NASA SP-195

SIGNIFICANT ACCOMPLISHMENTS IN SCIENCE

Goddard Space Flight Center, 1968

A symposium held at

GODDARD SPACE FLIGHT CENTER

January 10, 1969

NATIONAL AERONAUTICS AND SPACE ADMINISTRATION

NASA SP-195

SIGNIFICANT ACCOMPLISHMENTS IN SCIENCE

GODDARD SPACE FLIGHT CENTER, 1968

The proceedings of a symposium held at the NASA Goddard Space Flight Center, January 10, 1969

Prepared by Goddard Space Flight Center

Scientific and Technical Information Division
OFFICE OF TECHNOLOGY UTILIZATION 1969
NATIONAL AERONAUTICS AND SPACE ADMINISTRATION
Washington, D.C.

NATIONAL AERONAUTICS AND SPACE ADMINISTRATION

For sale by the Clearinghouse for Federal Scientific and Technical Information
Springfield, Virginia 22151 – Price $3.00

This is an almost-verbatim transcript of a Symposium held at Goddard Space Flight Center, Greenbelt, Maryland, on January 10, 1969. No attempt has been made to introduce editorial or stylistic uniformity; on the other hand, every attempt has been made to retain the informal flavor of the proceedings.

CONTENTS

OPENING REMARKS BY DR. JOHN F. CLARK
DIRECTOR OF GODDARD SPACE FLIGHT CENTER

Good morning, ladies and gentlemen. My name is John Clark. I'm the Director of the Goddard Space Flight Center. It's a real pleasure to welcome all of you to this first of what we hope will be an annual seminar on the scientific results of the Goddard space research program.

I should like to acknowledge our inspiration for the particular style and format being used here. It stems directly from an exceedingly attractive and successful seminar of this type carried out about a year ago at the Naval Research Laboratory in connection with the dedication of their new facilities at the E. O. Hulburt Center for Space Research.

I should also like to acknowledge the contributions of several men who are with us. James Webb, the second Administrator of NASA, is a man who is well known. He is, perhaps, less well known for one characteristic which has been extremely important to the science program of the Agency and to this Center. This is an extraordinary appreciation of the importance of a broadly based space program, in particular of the science which must underlie any such program. This Agency owes a great debt to Mr. Webb in this area as well as in some of those for which he may be better known.

Another man who has made contributions which clearly should be recognized in any meeting of this sort is with us today. This is Dr. Homer Newell, who was the first NASA Associate Administrator for Space Science and Applications and is the present Associate Administrator of the Agency. From the very early days preceding the establishment of NASA, in August 1958, with his initial discussions with the late Dr. Hugh Dryden, he has been Mr. Space Science of the Agency, until more than a year ago, when his responsibilities in the Agency were broadened still further. His presence with us today is eloquent testimony of his regard for this area of the Agency's activity.

The third man is Dr. John Naugle, who initiated his employment with the Agency here at the Goddard Space Flight Center. He is the third occupant of the office of Chairman of the Space Science Steering Committee, and is the second Associate Administrator for Space Science and Applications. We are very delighted to have him with us today.

For most of the people here it is not necessary to remind you that the results which will be discussed today are, among other things, the output of investigations in space. The other things include, for example, the very important theoretical background for such work, and the equally important laboratory investigations frequently associated with such work. But these results are the output, the culmination of the technological development and of the operations which tend to take so much of our total resources and occupy so much of our time. As such, these results ordinarily follow the actual space flights by an extended period of time. There are certain results that are available quickly, most notably photography. But, for the most part, we will talk about things which have occurred anywhere from three months ago to perhaps five years ago, relative to the actual space flight operations which are the basis of the results being discussed.

One word about the scope of today's meeting. This is not a total integrated output of the entire Goddard Space Flight Center. What we have today is the output of the Space Sciences directorate. I hope that the scope of these meetings can be extended to all of the directorates and all of the facets of the activities of the Center which use the scientific method in achieving their results.

Now it is very easy under these circumstances to feel that the work is more limited than is actually the case. There is a great deal of science in so-called applications areas. For example, meteorology is a science. Geodesy is a science. Earth resources, particularly at this stage of the game, rely very heavily on the scientific method to make sure that the operations to which many of us look forward will in fact be based on firm ground rather than sand.

In summary, one might say that there is a great deal of science in applications and a great many applications of science. These two areas are and must remain intertwined.

With that, I would like to introduce your Chairman, the Assistant Director for Space Sciences at Goddard, Dr. George Pieper.

REMARKS BY DR. GEORGE F. PIEPER, CHAIRMAN

Thank you, Dr. Clark.

Goddard Space Flight Center is the leading center for science within NASA. It is in fact one of the leading centers of scientific research in the United States and the world. Today members of the Space Sciences Directorate of Goddard are pleased to present to you a review of their accomplishments of 1968. I am proud to say that we have so many scientists and so much work going on that a very brief report from each person selected is all we have time for in a one-day program. Each speaker has been allotted only five minutes and three slides. Our experience with this method is that it really works no hardship. Rather, it forces the speaker to select very carefully what he wishes to say and to show. In order to keep the program on schedule, I shall limit sharply questions from the floor. The average number of questions allowed will be somewhat less than one. Our speakers will be pleased to talk with you during coffee, at lunch or at a reception which we have planned at the end of the day for our invited guests and speakers. So you will have ample opportunity to talk with people during the breaks.

RECOGNITION OF METEORITE IMPACTS FROM THE MICROSCOPIC STRUCTURE OF ROCKS

Bevan M. French

CHAIRMAN:

You will see from your program that the subjects of our work run all the way from earth resources to gamma-ray astronomy. I'd like to begin the program in the general area of earth resources, by calling first on Dr. Bevan French to talk about the recognition of meteorite impacts from the microscopic structure of rocks.

DR. FRENCH:

Probably the biggest geological problem that has come out of the space program is the considerable debate over the origin of lunar craters: Are they volcanic, or are they caused by meteorite impact? And, more to the point, given a large circular structure on the moon, how can you decide which is the case by examining a few pounds of rapidly-collected rock specimens?

The work with which I have been involved aims to answer this question. In the past few years it has become possible for geologists to establish unique criteria for the recognition of meteorite impact, using small samples, and to apply these criteria successfully to the recognition of large-meteorite impacts on the earth.

These criteria, which appear in the rocks themselves, are both large-scale and microscopic. They arise from the fact that, when a large meteorite hits the earth at its original cosmic velocity, the tremendous kinetic energy that it contains is released almost instantaneously as a shock wave into the surrounding rock. These shock waves may have peak pressures in excess of 10 megabars, and as they radiate from the impact point into the rock they do two things. First, they excavate and form a very large crater. Second, they produce in the target rocks unique and unusual deformational features which can survive permanently after the crater is formed. Such effects include the production of high-pressure minerals such as coesite, the initiation of high-temperature melting and decomposition, and the production of intense-strain features within the crystal lattices of individual minerals in the rock.

Such features, produced in terrestrial rocks by the shock metamorphism associated with a meteorite impact, occur in specimens of sandstone collected from Meteor Crater, Arizona (Figure 1). These photographs are of slabs of the rock that have been ground to a thickness of 30 microns and then examined microscopically in transmitted light, a standard geological procedure. The unshocked Coconino sandstone (left-hand photograph) is an aggregate of clear and undeformed grains of quartz or silica, the most common mineral on the earth. At moderate shock pressures, which we believe may be in the range of 50 to 150 kilobars, the quartz develops sets of planar fractures (center photograph) and the material between the quartz grains exhibits a glassy texture indicative of incipient melting. At even higher shock pressures, which may be in the range of 300 to 500 kilobars, the sandstone has been completely melted (right-hand photograph), probably at temperatures in excess of 1700° C. This melted sandstone has formed a frothy aggregate of silica glass which resembles volcanic pumice, but which can be distinguished from it by its chemical composition and by the remnants of very intensely deformed quartz grains (lower part of photograph).

These distinctive microscopic features have several advantages for identifying meteorite-impact structures:

First, they are apparently unique to meteorite impact. They have not been observed in rocks deformed by normal geological processes such as metamorphism or volcanic action.

Second, they can be easily and rapidly detected by standard geological techniques that have been in use for the better part of a hundred years.

Third, they require only small amounts of samples, less than a cubic centimeter, and therefore are very suitable for investigations of returned lunar samples.

Fourth, they can be preserved long after the meteorite fragments themselves have been destroyed and can give positive evidence on the origin of structures as old as two billion years.

Since 1960, geologists have applied these criteria very effectively to the study and recognition of terrestrial structures, with the result that the number of identified terrestrial meteorite-impact craters has climbed from 12 in 1960 to more than 60 now. This group now includes some structures more than 50 miles in diameter, comparable in size to major lunar features.

One example of this successful application is my own work on the Sudbury structure, Ontario, Canada. This is a structure of great age, about two billion years, and great diameter, originally more than 50 miles. It was originally believed to be volcanic and has associated with it ore deposits which have produced more than $9 billion worth of nickel, copper, and iron since they were discovered 60 years ago.

The recognition of the impact origin of Sudbury does not provide a prospecting tool because the ore deposits have already been effectively exploited for more than 50 years. However, the theory does provide important genetic information which is already being used by local geologists to guide future research and development in that region.

A quartz grain from one of the rocks at Sudbury (Figure 2) shows the very unusual shock-induced planar features similar to those in the shocked Cocomino sandstone (Figure 1, center). This specimen was hastily collected on a two-day trip to Sudbury, and yet it provided definitive evidence for the impact origin of structure--evidence which has been thoroughly verified and supplemented by subsequent studies.

In conclusion, these studies have made possible the definite identification of large meteorite-impact craters by examining small amounts of collected samples. Further goals in this field are: (1) experimental study of shock metamorphism in rock types such as basalts, which may occur on the lunar surface; (2) comprehensive geological studies of terrestrial impact structures in order to establish possible analogies with lunar craters.

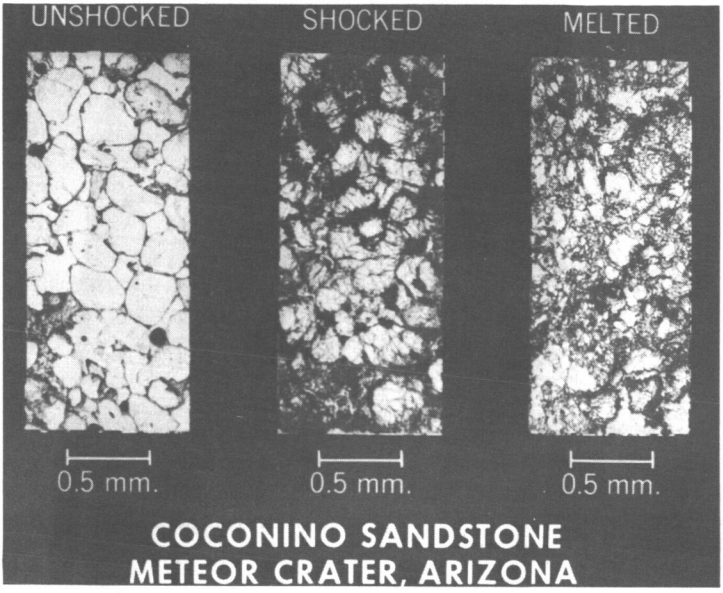

Figure 1

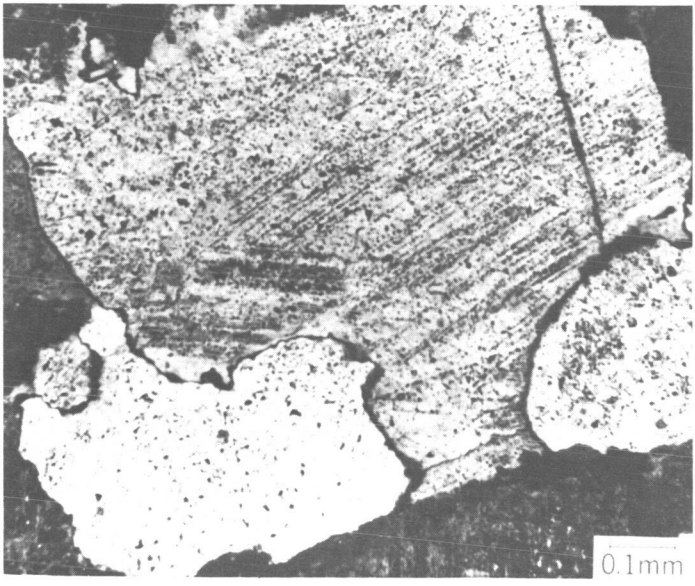

Figure 2

REMOTE SENSING OF THE SURFACE COMPOSITION OF THE EARTH

Warren A. Hovis, Jr.

CHAIRMAN:

I would like to call next on Dr. Warren Hovis to discuss the problem of remote sensing of the surface composition of the earth.

DR. HOVIS:

Most of the remote sensing of the lower atmosphere and the surface of the earth has been done as part of the meteorological satellite program. Instruments such as the Nimbus High Resolution Infrared Radiometer, though designed primarily for cloud mapping, have already produced useful earth-resources information such as ocean surface temperatures.

The recent interest in earth resources is principally concerned with the surface character of the earth in areas such as agriculture, oceanography, and geology, rather than with the atmosphere. Many of the techniques that have been developed for meteorology, such as high-resolution multichannel radiometry, are immediately applicable to earth resources.

One specific application of such techniques is remote sensing of the earth's mineral surface cover. One of the important methods of classification applied to this mineral surface cover uses silicon dioxide concentration. A concentration of 65 percent or more silicon dioxide is said to be acidic, 45 percent or less ultrabasic, with intermediate and basic between these two extremes.

Silicon dioxide produces a spectral feature known as reststrahlen, or residual rays, that appears as a minimum in thermal emission spectra of silicon-dioxide-bearing minerals in the 8-to-11-micron spectral region. The wavelength of this minimum varies with silicon dioxide concentration from 8.8 microns for the acidic, or high silicon dioxide concentration, minerals to 10.7 microns for the ultrabasic, or low silicon dioxide concentration, minerals. Remote sensing of the position of this minimum then allows us to determine silicon dioxide concentration.

Figure 1 illustrates the effect of reststrahlen on the thermal emission of two types of rock: granite, representing the acidic class, and dunite, representing the ultrabasic class. Granite is seen to have a minimum around 8.8 microns, and it can be seen that if one were to measure the radiance at 8.8 microns and at 10.7 microns and calculate the equivalent blackbody temperatures at both wavelengths it would appear that the granite was cooler in the 8.8-micron region than in the 10.7-micron region. Since the radiating surface can have only one temperature at one time, the difference must be due to an emissivity difference.

Dunite, representing the ultrabasic class, can be seen to have its minimum around 10.7 microns and hence would appear cooler in the 10.7-micron region than at 8.8 microns. Thus, if we use a two-channel radiometer with channels centered at 8.8 and 10.7 microns, we can discriminate between classes by observing which channel indicates a lower equivalent blackbody temperature. Absorption due to the ν_1 band of ozone is shown in Figure 1. Unfortunately, it covers the reststrahlen of intermediate and basic minerals, so that we cannot sense the reststrahlen of these classes. This limitation would not apply to the moon or Mars.

We have constructed a small two-channel radiometer with channels centered at 8.8 and 10.7 microns and flown it, in this locality, on a small aircraft. Figure 2 shows the equivalent blackbody temperature measured in the two channels versus distance as the aircraft flew over a serpentinite quarry in Rockville, Maryland. Over the trees and fields on either side of the quarry, both channels indicate the same equivalent blackbody temperature to within instrumental accuracy. Over the quarry, the 8.8-micron channel indicates a warmer temperature than the 10.7-micron channel, indicating a lower emissivity at 10.7 microns than at 8.8 microns and hence an ultrabasic mineral. Ground truth has confirmed that the serpentinite is indeed ultrabasic.

Another method of presentation is shown in Figure 3, a color representation of the instrument scanning as the plane flew over Assateague Island, Virginia. The indicated temperature difference is shown in color: green represents essentially no difference between the two channels, and the increasingly red scale indicates differences, with the 8.8-micron channel the cooler of the two. The ocean, on the left in Figure 3, appears to have the same temperature in both channels; while the sand of the island, on the right, produces apparent temperature differences as high as 8 degrees. Since the 8.8-micron channel indicates the cooler temperature, the surface of the island appears to be highly acidic, that is, rich in silicon dioxide. The ground truth confirms that this is indeed the case.

These two examples, in conjunction with many others not presented, show that we can unambiguously locate and identify acidic and ultrabasic minerals. Virtually all other natural materials such as water, ice, snow, trees, and fields are black in the spectral intervals of interest, so that no differences in apparent temperature will occur over such materials and both channels will indicate the true blackbody temperature.

A new and better instrument is now under development, as are better methods of data display and handling.

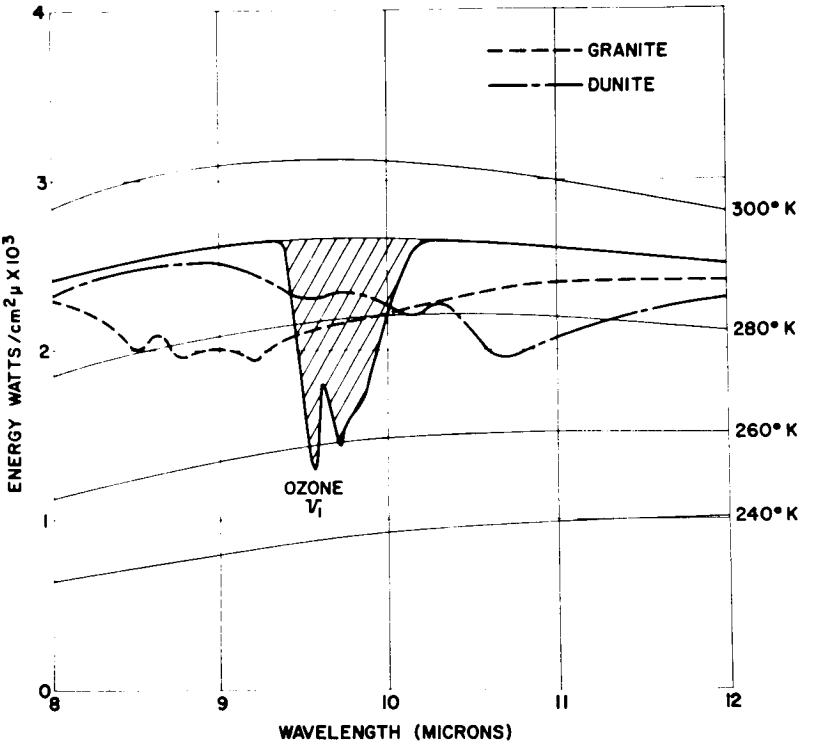

Figure 1

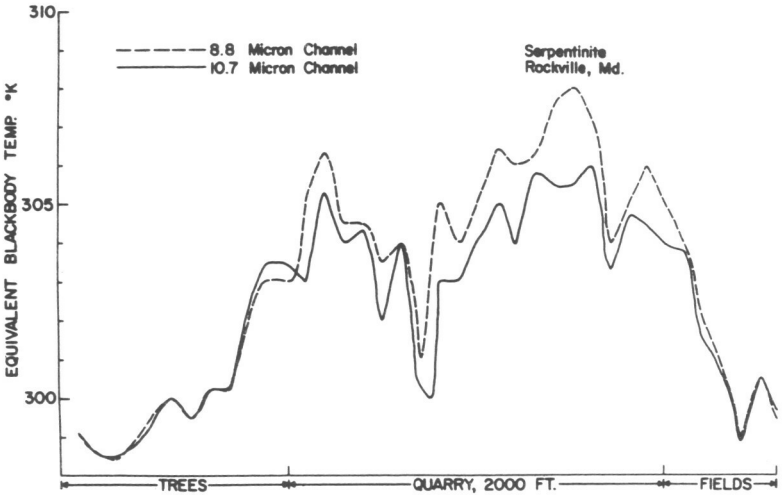

Figure 2

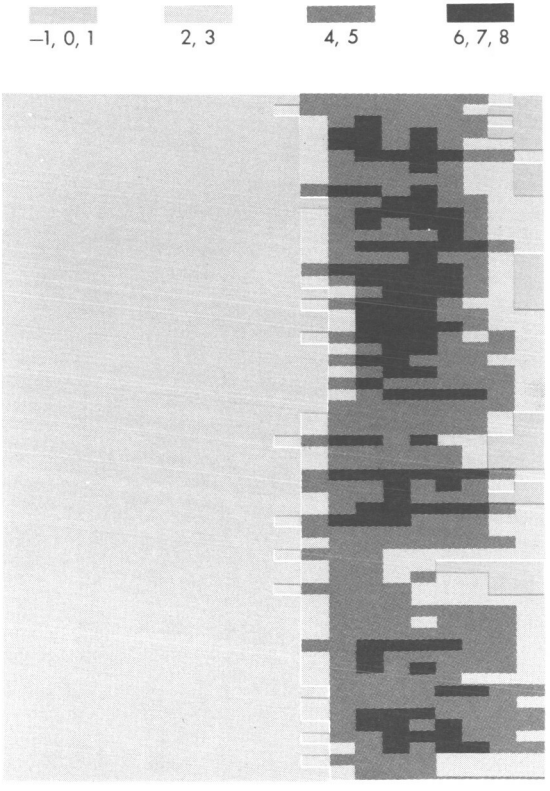

Figure 3

RESULTS OF THE HRIR EXPERIMENT WITH NIMBUS II

Lewis J. Allison

CHAIRMAN:

We will move into the results from the Nimbus experiment, and Mr. Lewis Allison will discuss the results from the HRIR, or high resolution infrared radiometer, experiment with Nimbus II.

MR. ALLISON:

The Nimbus II satellite, which was launched into a polar orbit in May of 1966, recorded six months of high quality infrared radiation data which were used for meteorological and oceanographic research. The high resolution infrared radiometer, or HRIR, which produced these data was a single-channel instrument sensitive to the radiative emission of the earth in the 3.5- to 4.2-micron atmospheric wind belt. It contained a lead selenide photoconductive cell radiatively cooled to approximately 198° K, and designed to measure radiant temperatures between 210° K and 330° K during nighttime conditions.

Based upon a 0.5° field of view at an average 1100-kilometer satellite altitude, a rectangular 9 × 10 kilometer scan spot was subtended at the sub-satellite point. Scanning was performed by a mirror which rotated perpendicularly to the orbital plane; and an in-flight calibration was achieved by viewing alternately outer space and the spacecraft housing, the temperature of which was monitored during each scan.

An example of nighttime HRIR coverage over the Gulf Stream is shown in Figure 1.

This Mercator map was made by an IBM 7094 computer from three minutes of digitized data with concurrent orbital and attitude information. The most significant feature shown in this figure is the strong 10° K gradient over a 10-kilometer distance between the warm (300°K) Gulf Stream water, which is in pink, and the cooler (290°K) water to the north.

This interface or north wall that you see outlined in black here was also delineated by U.S. Navy radiometer-equipped aircraft on the same night under clear sky conditions. An evaluation of several hundred scan spots over the north wall indicated that the HRIR measurements by Nimbus II were 2°K to 4°K cooler than the aircraft data.

This Gulf Stream boundary was seen in significant detail on about 50 out of 175 days. Similar results were obtained in analyses of the boundary between the Brazil and Falkland Currents.

Figure 2 shows a Mercator map of the southeast coast of South America, in which brightness values are color-printed to emphasize the temperature contrast at the boundary of the warm, southward-moving (pink colored) Brazil Current and the cold (green colored) Falkland Current, which is moving in a northerly direction. At the left is a scan of analog voltage data recorded just south of the La Plata River. It's also shown on an equivalent blackbody temperature scale. The cool Argentina coastline, Falkland Current, and coastal waters are indicated by 280°K to 283°K on the analog trace, while the warm Brazil Current is shown by 288°K isotherms.

Figure 3 shows the important ocean currents of the world. Nimbus II radiation studies over the warm currents, which are shown in pink, such as the Kuroshio, Agulhas, the Gulf Stream, the Brazil Current, and the cold (blue-toned) currents, such as the Falkland and Peru Currents, have been initiated and more studies are planned for the future.

For detailed oceanographic research, a higher spatial resolution and a shift to the 10- to 11-micron region are desirable to permit quantitative measurements in the daytime as well as in the nighttime. Simultaneous observations with a visible channel would be valuable for the identification and rejection of cloud-contaminated data within the field of view of the radiometer.

These initial oceanographic studies of sea surface temperature illustrate the potential earth-resources benefit to the worldwide fishing and shipping industries. Additionally, these measurements can be applied to the increasingly complex air-sea interaction model being developed for long-range forecasting in the world weather program of the next decade.

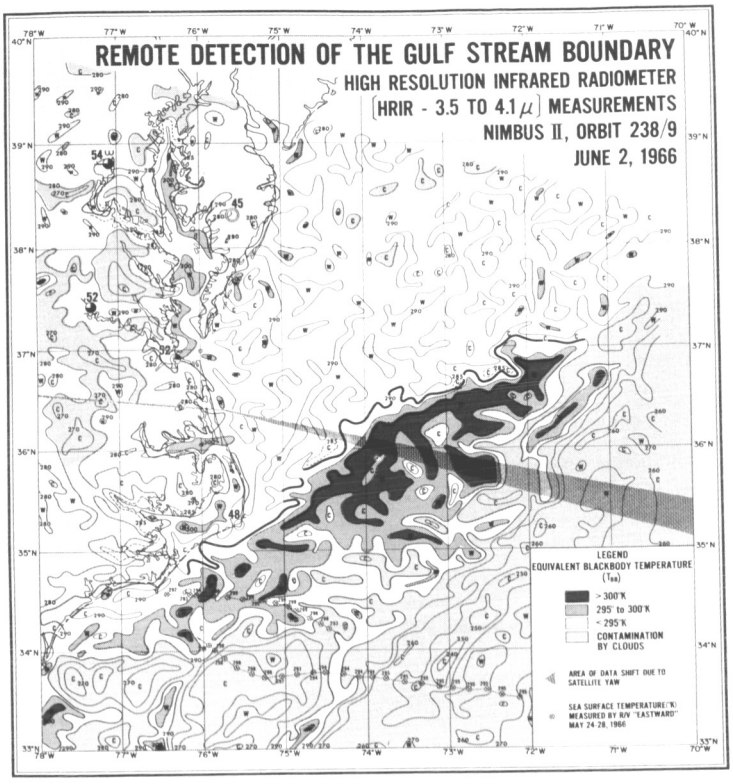

Figure 1

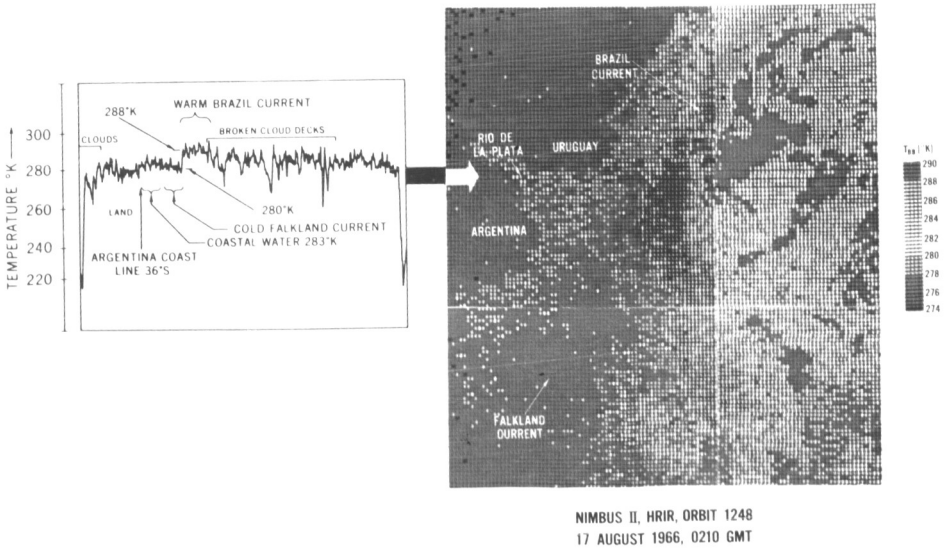

Figure 2

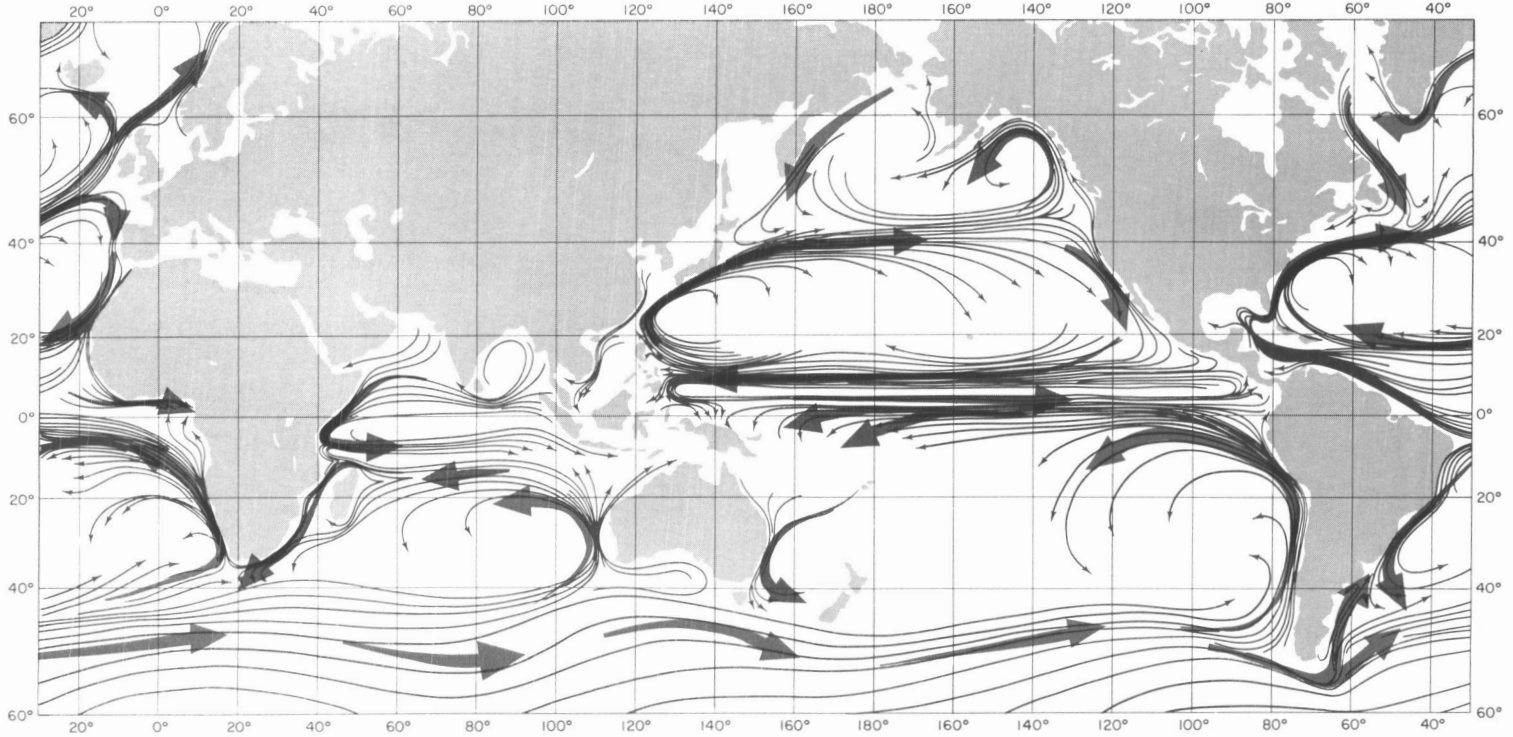

OCEAN CURRENTS OF THE WORLD

Figure 3

DEPENDENCE OF MICROWAVE EMISSION UPON SEA STATE

Jack Conaway

CHAIRMAN:

Occasionally one finds an unexpected result, perhaps, from a measurement. One of those that I believe was somewhat unexpected was the fact that the microwave emission from a body of water depends considerably upon the sea state.

Our next speaker, Jack Conaway, will describe his work in this area.

DR. CONAWAY:

Remote sensing with meteorological satellites has utilized the visible and IR portions of the electromagnetic spectrum; Nimbus D will use the UV. All of these sensors provide, of course, meteorologically useful information. However, in an effort to obtain unique geophysical information, we have developed an electronically scanning radiometer to map thermal radiation emitted from the earth's surface and atmosphere in the microwave region.

Aircraft flights with this instrument have demonstrated several surprising applications, as well as the ones we were looking for. Some of these applications are: sea ice mapping through clouds; soil surface moisture measurement; snow surveys; mapping of liquid water content of clouds; and the subject for today, sea state measurements.

During flights over the Imperial Valley of California this summer, it was noted that the southern half of the Salton Sea was quite choppy because of a local dust storm. The northern half of the sea was quite calm. This combination provided an excellent chance to record differences in microwave emission from these two sea conditions.

Figure 1 is a color presentation of the radiation intensity field in a pass at 12 kilometers above the Salton Sea. The delineation between the rough sea to the south and the smooth sea to the north is apparent, and corresponds exactly to the visible photography taken at the same time.

Figure 2 gives a more quantitative presentation of the data. We have graphed equivalent blackbody temperatures, averaged for several scans of the radiometer, versus nadir angle for both the smooth and rough portions of the sea. For comparison, temperatures computed by Stogryn for similar conditions are shown in the smooth and dashed curves.

The agreement between our data and Stogryn's computations is very good for the smooth sea: slight disagreements, but nothing that can't be accounted for by his assumptions. However, there is serious disagreement regarding the rough portion of the sea. Stogryn predicts about a 17°K difference at large nadir angles, and almost no difference at zero. We, on the other hand, find considerable difference at all angles—out to 50°, at least. And, most importantly, this difference appears to be constant with nadir angle. The latter factor is important from the viewpoint of possible earth resources applications, since no complicated corrections must be made for viewing angle.

Computed surface emissivities show an even greater increase with roughness than do the microwave-brightness temperatures, since the actual surface temperature measured with an IR radiometer was 3°*colder* for the rough sea than for the smooth sea. We are confident that this emission increase is due to the increase of foam and spray on the surface, a phenomenon which was not accounted for in Stogryn's analysis.

From this, the meteorological significance of our measurements is evident when it is noted that several oceanographers have related the amount of foam on the sea surface to the surface wind speed. Some of their results are shown in Figure 3, where percent of foam cover is plotted as a function of wind speed. The relatively low wind speeds for our two measurements are shown by the arrows. Foam cover seems to be an even more sensitive indicator of wind at the higher wind speeds in which we are most interested.

Incidentally, the apparent disparity between the two curves, I think, is largely due to Blanchard's extrapolation.

Thus our measurements of microwave emissivity, which we feel are strongly related to the amount of foam on the sea surface, are an indirect measure of the surface wind speed. In addition, of course, a knowledge of sea state per se is of practical value to the shipping industry. By making these measurements at a somewhat longer wavelength and from a satellite, we hope to map sea state globally, even in the presence of moderate cloud cover.

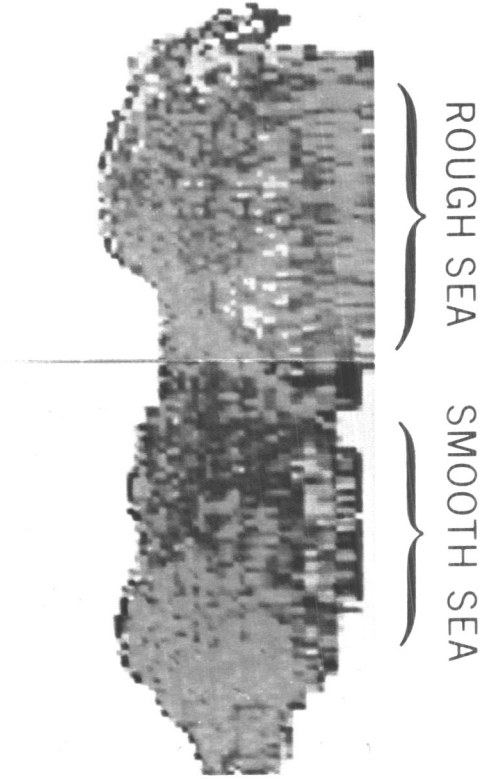

Figure 1

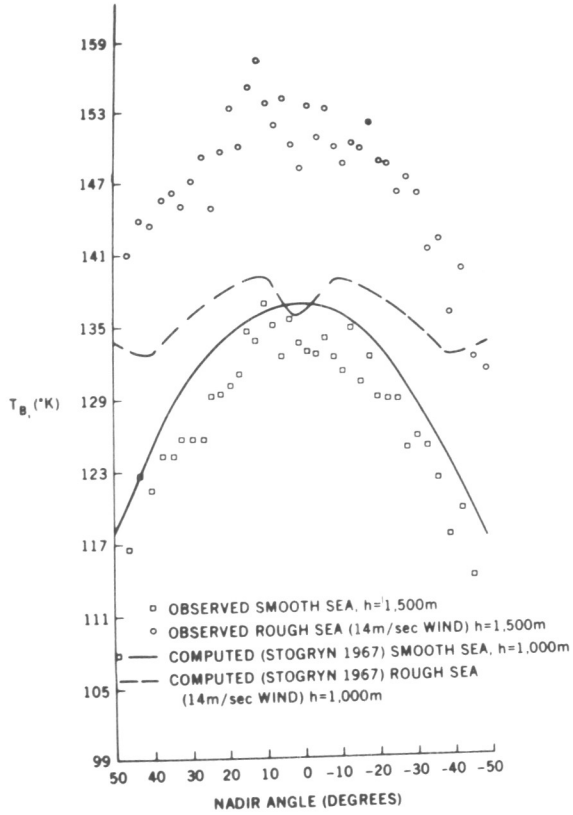

Figure 2

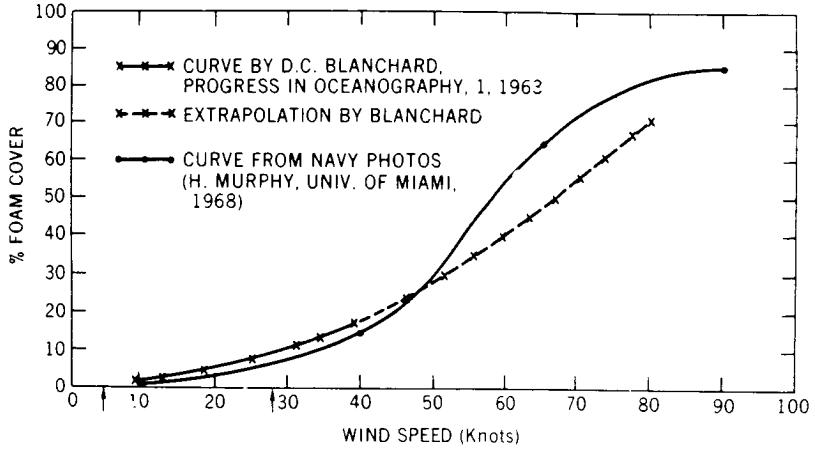
CURVE BY D.C. BLANCHARD, PROGRESS IN OCEANOGRAPHY, 1, 1963
EXTRAPOLATION BY BLANCHARD
CURVE FROM NAVY PHOTOS (H. MURPHY, UNIV. OF MIAMI, 1968)
% FOAM COVER
WIND SPEED (Knots)
0
10
20
30
40
50
60
70
80
90
100

Figure 3

INDIRECT SENSING OF ATMOSPHERIC WATER VAPOR

Barney J. Conrath

CHAIRMAN:

We will move now from the area of looking at the earth from space to the area of investigating the atmosphere from space from *in situ* measurements. The first talk in this general group will be by Dr. Barney Conrath, who will talk about the methods of indirect sensing of atmospheric water vapor.

DR. CONRATH:

In the past several years, considerable effort has been devoted to the development of theoretical techniques for inferring vertical temperature profiles from measurements of infrared radiation emitted by the earth's atmosphere. However, in addition to obtaining temperature information from measurements in absorption bands of uniformly-mixed carbon dioxide, it is also possible to get information on the vertical distribution of nonuniformly-mixed gases which are optically active in the infrared, such as ozone and water vapor. Recently we have been concerned with developing the theory of inferring vertical water vapor profiles from remote rediometric measurements.

The basic principles involved are illustrated in Figure 1. On the right-hand side we have plotted a typical temperature profile for the lower atmosphere, i.e., temperature versus the logarithm of pressure level in the atmosphere--which level is roughly proportional to the geometric height. The intensity of the infrared radiation reaching a satellite-borne sensor in a narrow spectral band can be regarded as the weighted mean of the Planck intensities associated with the temperature at each level in the atmosphere. On the left, looking first at the solid curve, we have plotted the relative contribution of each layer in the atmosphere to the outgoing intensity as seen from the top of the atmosphere for two narrow spectral bands, one located near the opaque center of the 6.3-micron water vapor absorption band, and the other in the more transparent wing of the same absorption band.

These so-called weighting functions are dependent on the total amount and vertical distribution of the absorbing gas. For example, if the relative humidity is decreased uniformly by 20 percent at all levels in the lower atmosphere, the weighting functions shift to the positions shown by the broken curves in Figure 1. In this case, slightly different segments of the temperature profile will be sampled, and there will be a corresponding decrease in the intensities measured at the top of the atmosphere. If, instead of changing by a uniform amount at all levels, the relative humidity is changed by differing amounts at different levels, then there will be a corresponding differential change in the intensities as measured in the different spectral intervals. We have attempted to use this basic concept to develop a computational technique for inferring vertical water vapor profiles from simultaneous measurements in several different spectral regions, ranging from the band center out into the band wing.

Figure 2 shows the results of an application of this technique to actual data obtained from an infrared interferometer spectrometer or so-called IRIS instrument. Here we have plotted water vapor mixing ratio as a function of pressure level in the atmosphere. The sloping line represents the water vapor profiles inferred from the infrared measurements. For comparison we have plotted 12 *in situ* measurements obtained from radiosonde ascents at a nearby radiosonde station, and we feel that the results are encouraging.

We are currently attempting to develop more sophisticated computational techniques, and the data to be obtained from the forthcoming Nimbus B2 satellite will provide an opportunity to test these techniques on a global basis. The techniques, at least in principle, can also be applied to thermal emission spectra from the atmospheres of other planets, and this aspect of the problem is being investigated as well.

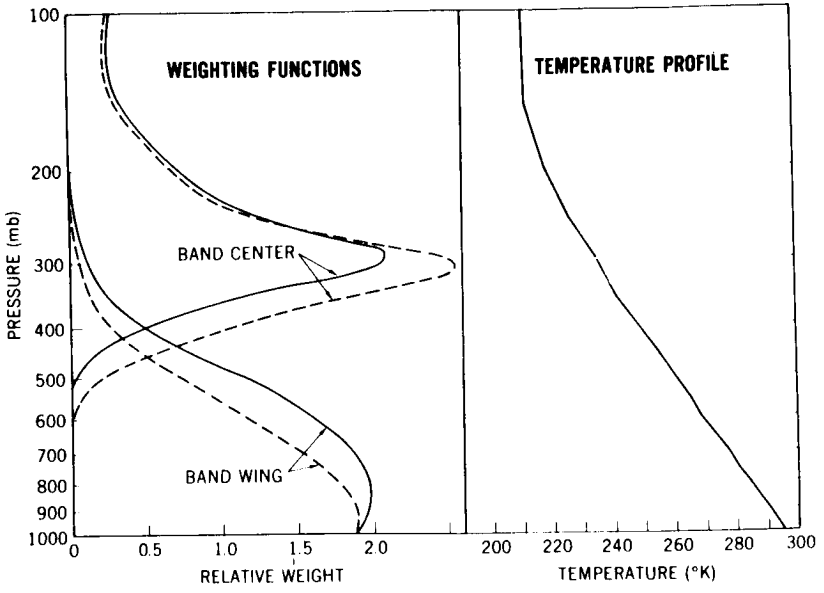

Figure 1

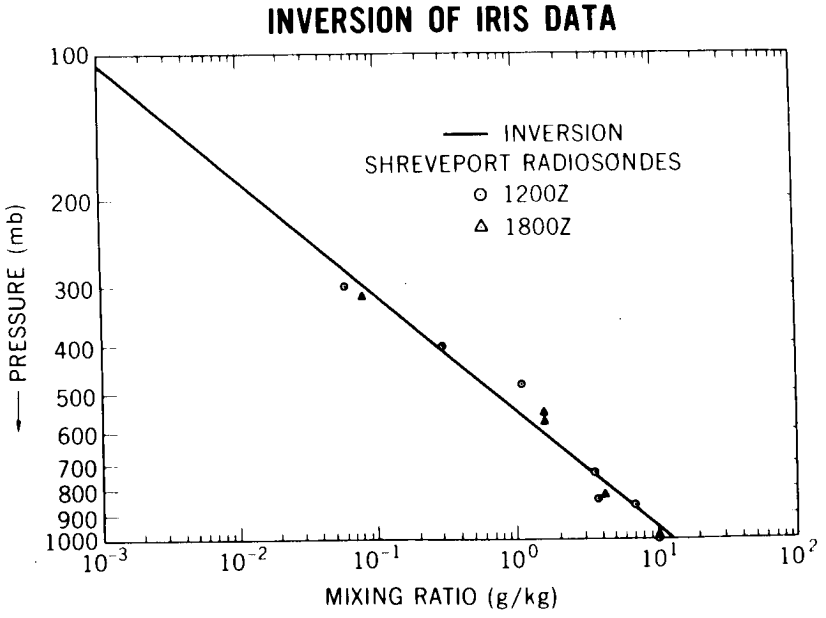

Figure 2

A CHEMILUMINESCENT MEASUREMENT OF OZONE IN THE ATMOSPHERE

Ernest Hilsenrath

CHAIRMAN:

The next subject concerns the measurement of ozone in the atmosphere by a chemiluminescent technique, and it will be presented by Ernest Hilsenrath.

MR. HILSENRATH:

High resolution ozone profile measurements obtained in the stratosphere and mesosphere will give some insight into a number of problems that have concerned the atmospheric physicist for some time. These are, first, the nature of vertical and horizontal transport of mass and energy in the stratosphere and the deposition of radiative energy at these altitudes. Second, the departures from photochemical equilibrium in the standard $O_2 - N_2$ atmosphere above the stratopause at 50 kilometers—departures such as those due to changes in solar illumination, to the absence of illumination in the polar winter night, and to the presence of other photochemically active minor constituents such as H_2O, hydroxyl radicals, NO, et cetera. And of special interest is the formation of a secondary ozone concentration peak near 60 kilometers during the nighttime. Of increasing importance, third, is the recognition of the possible occurrence of interactions between the neutral and charged atmospheres in the D region and the aurorae.

A few measurement techniques have been applied to this problem of ozone measurements, mostly based on deriving integrated ozone measurements, mostly based on deriving integrated ozone concentrations from the absorption of solar or airglow radiation. Our technique is based on a chemiluminescent reaction with ozone and performs the measurement *in situ*, day or night, from altitudes of 65 to 20 kilometers (the latter is below the ozone peak), by means of a parachute sonde released from a rocket. The experiments can be performed at stations where the measurements will have the greatest geophysical significance, such as during the polar night, or during solar eclipses. These flights may also be performed in support of future satellite experiments.

The operation of the ozone sensor can be described in the following manner, with the aid of Figure 1. The luminescence from the chemiluminescent material is proportional to ozone flux – that is, ozone flux is ozone concentration times the flow rate. Flow, or sampling of the ambient atmosphere, is accomplished by a self-pumping technique and can be described in the following manner: Consider an empty ballast chamber that is connected to the external environment by means of an inlet pipe and is in pressure equilibrium with the ambient atmosphere. The sonde is released at apogee, approximately 70 kilometers, and descends through the atmosphere via a specially designed high-altitude parachute. As the sonde descends, the increasing external pressure causes an increase in pressure inside the ballast chamber, resulting in a net flow of gas through the inlet pipe. Thus a flow rate measurement is determined by a pressure measurement inside this ballast chamber.

The ozone detector, consisting of the chemiluminescent material and the photometer, is oriented along the tube, thus providing a continuous measurement of the atmosphere for ozone content.

Figure 2 is a picture taken on our initial flight at Wallops Island. A parachute recovery was attempted. An ozone profile was obtained despite a partial parachute failure. The ozone sonde, as shown in Figure 2, was recovered out of the water, providing an opportunity to determine the cause of failure.

Figure 3 shows the results of the flight. Ozone density in molecules per cubic centimeter is plotted as a function of altitude. The data obtained from the chemiluminescent ozone sonde are shown by the solid line. A Naval Weapons Center rocket optical sonde and two balloon ozone sondes, one from ESSA and one from the Air Force Cambridge Research Laboratory, were flown simultaneously in support of this flight. The rocket optical sonde was capable of obtaining daylight measurements of lesser altitude resolution up to about 50 kilometers, shown by the solid circles, that practically coincided with the data obtained from the chemiluminescent sonde. The data from the two balloon sondes, shown by the X's , give essentially the same results and are in good agreement where the data overlap with the rocket data.

The data about 57 kilometers are shown, in Figure 3, only for demonstrative purposes because, as you can see, the measurement was performed back in 1960 using an airglow technique. The data, which have been reported in the literature, show a secondary ozone maximum at night, whereas our measurement was performed during the day.

We are highly encouraged by the performance of our initial flight because of the good agreement with the other ozone sensors and especially by the wide altitude range capability of the chemiluminescent ozone sonde.

MEMBER OF AUDIENCE:

The University of Minnesota has made some of these measurements at lower altitudes. How good is their data?

MR. HILSENRATH:

Are you talking about a Mr. Kronig?

MEMBER OF AUDIENCE:

Yes.

MR. HILSENRATH:

Yes; I don't know if he is still making these measurements. I know he has been using a chemiluminescent technique for balloon measurements, similar to the Regener technique, and I don't know of any recent measurements that he has made. But the comparison measurements that we have performed in support of our flight were made by standard ESSA and Air Force Cambridge Research Laboratory balloon ozone sondes flown along with the radio sondes. These are accepted techniques. And one thing I must add, in regard to our measurement, there was no adjustment or normalization of our ozone profile to a Dobson measurement or to the balloon measurement. We had an independent calibration.

OZONE SENSOR FOR SOUNDING ROCKETS

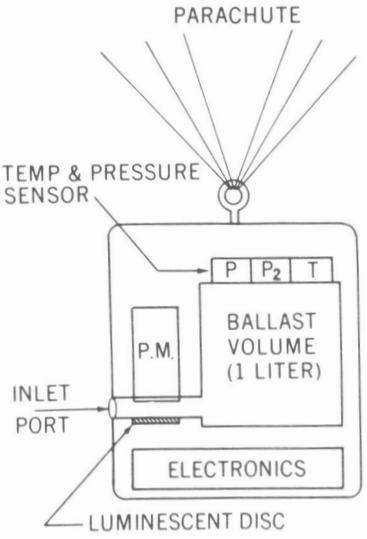

$$O_3 \text{ CONC.} \sim \frac{O_3 \text{ FLUX}}{\text{AIR FLOW RATE}}$$

O_3 FLUX ~ P.M. SIGNAL

AIR FLOW RATE ~ dp/dt

Figure 1

ROCKET OZONE SONDE

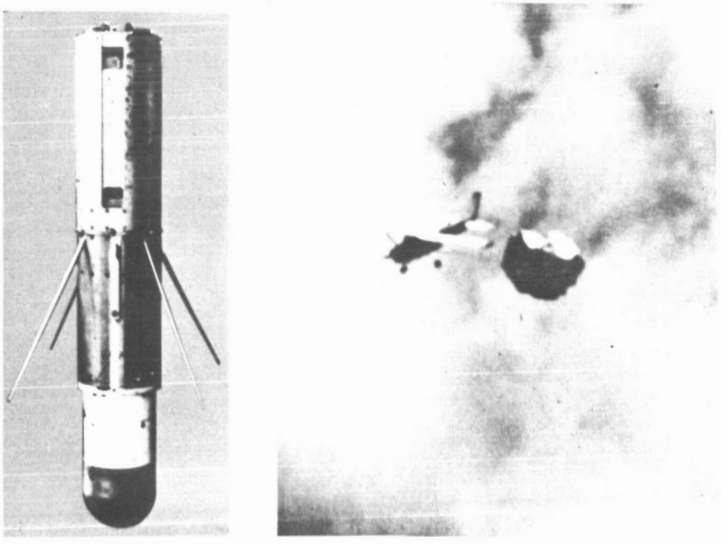

Figure 2

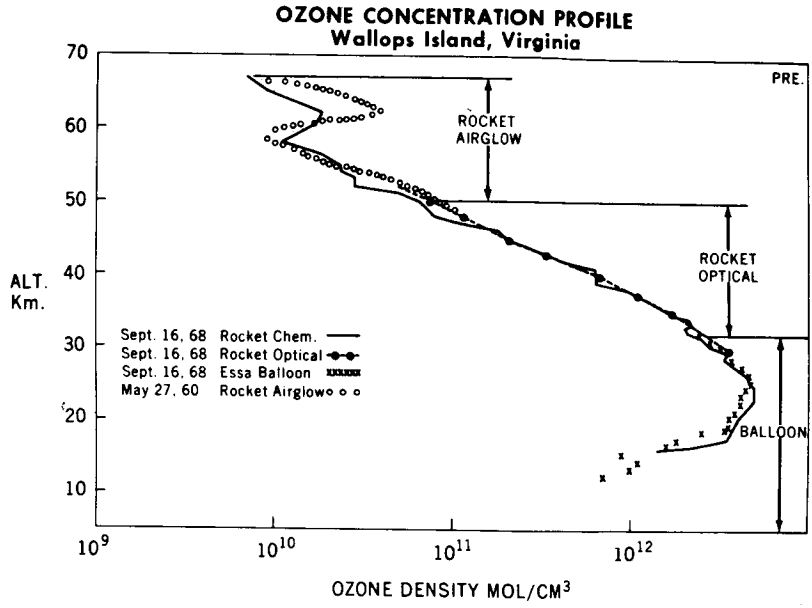
OZONE CONCENTRATION PROFILE
Wallops Island, Virginia
PRE.
ROCKET AIRGLOW
ROCKET OPTICAL
BALLOON
ALT. Km.
70
60
50
40
30
20
10
Sept. 16, 68 Rocket Chem.
Sept. 16, 68 Rocket Optical
Sept. 16, 68 Essa Balloon
May 27, 60 Rocket Airglow
10^9
10^{10}
10^{11}
10^{12}
OZONE DENSITY MOL/CM^3

Figure 3

SHORT-TERM TEMPERATURE VARIATIONS IN THE WINTER MESOSPHERE

John S. Theon

CHAIRMAN:

The subject of the temperature variations of the upper atmosphere is one that many members of Goddard have been involved in for some time. John Theon will tell you about the most recent results involving the short-term temperature variations in the winter mesosphere.

MR. THEON:

As recently as three years ago, the thermal structure of the mesosphere was believed to change relatively slowly with the seasons at middle and high latitudes and to remain rather uniform with time in the tropics. This concept had evolved largely from the nearly 200 mesospheric soundings conducted during the past eight years by the meteorological sounding rocket program here at Goddard. This program has systematically covered the four seasons at latitudes ranging from shipboard soundings at 60°S to those at Pt. Barrow, Alaska, at 71°N; and including Natal, Brazil, at 6°S; Ascension Island, at 8°S; Wallops Island, Virginia, at 38°N; and Churchill, Canada, at 59°N.

The logic of our concept of the mesosphere was sound enough, since the mesosphere is well above the region in the atmosphere where conductive and convective heat exchange with the earth's surface during short periods of time are important; also by reason of analogy with tropospheric meteorology, where the effects of radiative energy exchange are significant only when integrated for a period of several days or more. Thus we assumed that a sounding made at a given site was representative of that site for a period of several days and that it was representative of that site with respect to general characteristics for the entire season. To illustrate this point, I have selected data from Pt. Barrow, because the contrast between winter and summer there is most pronounced.

Consider Figure 1, which shows seven temperature profiles above Pt. Barrow observed with the acoustic grenade technique. These results, which show the temperature of the atmosphere plotted as a function of altitude, were obtained during the summers of 1965 and 1966. Note that

the temperature of the mesosphere, the region from approximately 50 kilometers to 85 kilometers—for the engineers in the audience, that's 160,000 ft. to 270,000 ft.—does not vary by more than 10°K at any given altitude. Note the very close correspondence of temperatures among all the soundings.

These data certainly confirm the concept of the mesosphere I have already described. However, when we began to conduct soundings in the winter at intervals of several hours, we found a completely different situation. Figure 2 shows six temperature profiles obtained with the same observational technique and from the same site during a 15-hour period in winter. These profiles are characterized by alternately warm and cold regions which produce a wave-like structure in the profiles. The vertical spacings between adjacent warm regions are on the order of 10 to 15 kilometers; and, most significantly, temperature changes of 30°K to 40°K per hour are common in the upper mesosphere. Note also that in the amplitude of these variations—that is, the peak-to-peak variation in temperature—increases with altitude. Such temperature changes in the mesosphere were previously unknown. Their existence demonstrates that currently-accepted theory which treats the mesosphere as a stratified, stable fluid is inadequate in these cases. While we are not yet able to account for these new data quantitatively with theory, certain implications have been drawn from their study.

First, the profiles shown include superadiabatic lapse rates which are inherently unstable and thus cause overturning of the air.

Second, large-amplitude vertical motions are necessary to explain the large changes in the temperature structure during such brief periods of time. Large vertical velocities, in turn, suggest the presence of internal atmospheric gravity waves or turbulence in which the vertical eddy size is an order of magnitude larger than heretofore believed to exist.

And, third, the large vertical velocities which are implied by the observed temperature changes could transport minor constituents such as atomic oxygen downward to levels where they would exothermically react to liberate heat.

The observed temperature variations are most likely the result of some combination of all of these processes. Auroral heating has been ruled out as a source of energy because the strong seasonal bias in the temperature structure does not correlate with the occurrence of aurorae.

Additional soundings were conducted from high latitude sites during February, October, November, and December of 1968 in a continuing effort to define and better understand this mesospheric behavior.

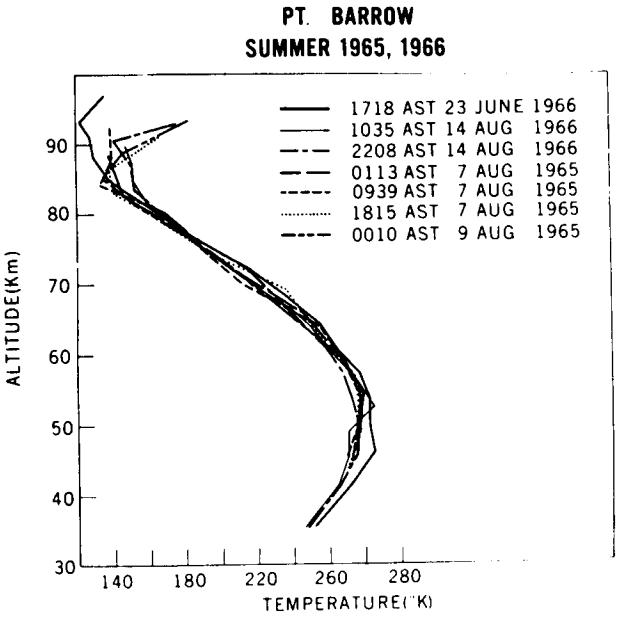

Figure 1

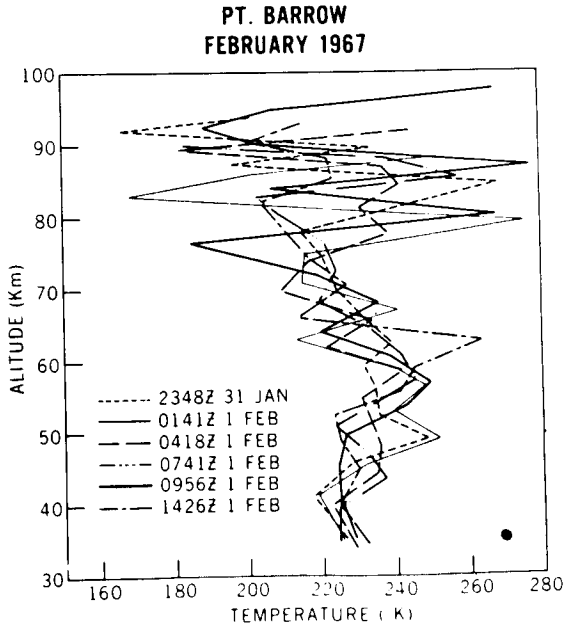

Figure 2

WAVES IN THE NEUTRAL THERMOSPHERE

George P. Newton

CHAIRMAN:

Our next speaker will continue a subject which is somewhat related to this idea of waves in the atmosphere. His subject is waves in the neutral thermosphere: Mr. George Newton.

MR. NEWTON:

One of the more interesting phenomena observed by the atmospheric density experiment on the Explorer XXXII satellite was the presence of wave structure in the neutral thermosphere density. This wave structure extended from the satellite perigee at 258 kilometers altitude to altitudes as large as 550 kilometers, and provides evidence for direct coupling between the lower and upper atmosphere.

This morning I am going to show a few examples of the observations. I am going to present a model under which we are interpreting the observations, and present a comparison between the model and the observations, and then draw a conclusion.

Figure 1 shows the measured atmospheric density versus altitude. The density is plotted in grams per cubic centimeter along the ordinate; the altitude in kilometers along the abscissa. The upper part of Figure 1 shows what we observe approximately 80 percent of the time. Each dot represents a direct measurement of the atmospheric density separated in real time by two seconds. This corresponds to a distance of 16 kilometers along the satellite orbit. The line represents a least squares fit to the data of an exponential dependence of density upon altitude. Quite often we observe very smooth profiles.

As illustrated in the lower part of Figure 1, we see obvious wave structure in the neutral thermosphere approximately 20 percent of the time. The line and the dots have the same meaning as they did in the upper part of Figure 1.

Two points should be made about this wave structure. First, if the half-amplitude of the wave structure is measured relative to the

exponential decrease of density with altitude, it is observed that the half-amplitude remains relatively constant over an altitude range corresponding to approximately two atmospheric density scale heights. This behavior indicates an upward-propagating wave. Second, there is an indication that the apparent vertical half-wave length is increasing with altitude.

Figure 2 shows the model which we use to interpret the data. We have plotted altitude versus horizontal distance. Imagine that we have a slow, predominantly horizontally-propagating wave pattern in this space, and we have plotted planes of extrema phase, pluses representing the compression phase of the wave, minuses the rarefaction phase of the wave. Now imagine that a satellite represented by the dashed parabolic curve passes through the wave pattern. What would we expect the satellite to see?

First, superimposed upon the altitude decrease of density would be rarefactions and compressions as the satellite passes through the planes of extrema phase of the wave.

Second, on both the descending altitude portion of the orbit and the ascending altitude portion of the orbit, the apparent vertical half-wave length increases with altitude. It should be pointed out that the scales in Figure 2 are not proportionate. The horizontal distance scale, when compared to the altitude scale, has been decreased by a factor of 16 for presentation.

Figure 3 shows many observations of the larger apparent vertical half-wave lengths versus altitude in kilometers. The X's represent measurements obtained when the satellite was descending in altitude; the circle symbols represent measurements obtained from the satellite when it was ascending in altitude. The lack of a strong Doppler shift between 280 and 300 Km has caused us to exclude acoustic waves as the cause of the wave structure in the atmosphere. The line in this figure has been calculated assuming the model shown in Figure 2 and a horizontal wave length, and is in good agreement with the data. The horizontal wave length assumed for this particular calculation was 520 kilometers. This wave length, together with other aspects of the data (not presented here), have led us to conclude that we are observing the propagation of gravity waves in the neutral thermosphere.

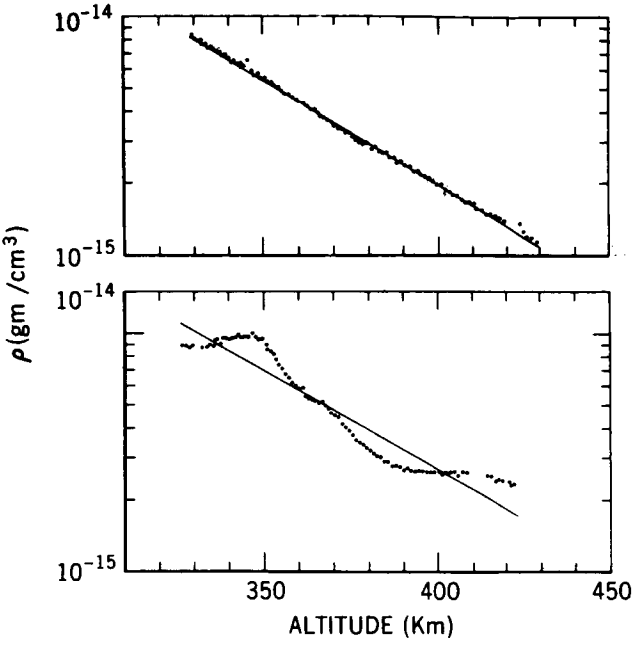

Figure 1

SATELLITE MOVING THROUGH WAVE-LIKE STRUCTURE OF NEUTRAL THERMOSPHERIC DENSITY.

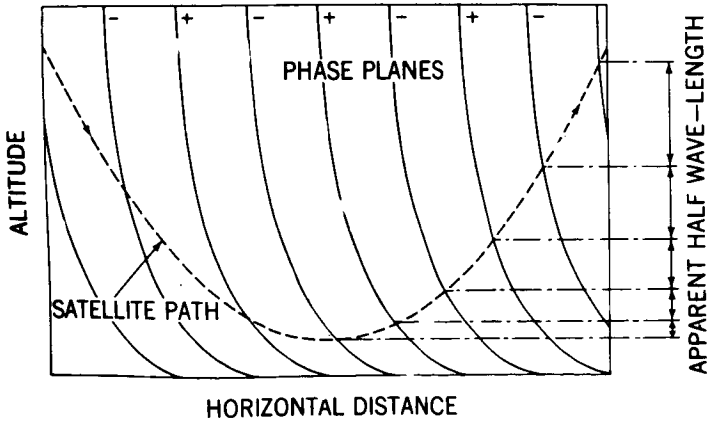

Figure 2

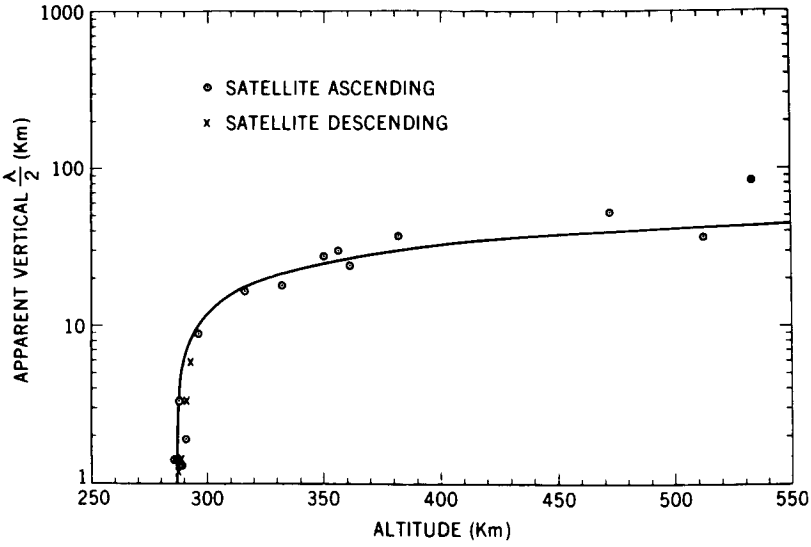
1000
100
10
1
250
300
350
400
450
500
550
SATELLITE ASCENDING
SATELLITE DESCENDING
APPARENT VERTICAL $\frac{A}{2}$ (Km)
ALTITUDE (Km)

Figure 3

THE EQUATORIAL ANOMALY AND ATMOSPHERIC WINDS

Hans G. Mayr

CHAIRMAN:

The next subject will be the equatorial anomaly and atmospheric winds, by Dr. Hans Mayr.

DR. MAYR:

Bottomside sounder and satellite measurements have indicated that the latitudinal variations in electron density of the F_2 region are very significant.

In Figure 1 (left half) we show as X marks the measured electron density at the F_2 maximum plotted versus geomagnetic latitude. We see from this plot that the electron density decreases very rapidly as we go to higher latitudes, by a factor of almost 8. This is for minimum solar activity and during daytime. Second, we find that a density minimum forms at the equator a phenomenon that is known as the equatorial anomaly.

The processes that are basically responsible for the formation of the F_2 region are photoionization, recombination, and diffusion along the constraining magnetic field lines of the earth. We have considered these processes, and we computed the electron density at the F_2 peak and we show this density as a dashed line in the figure. From this we see that we are able to reproduce the observations qualitatively. The electron density decreases toward higher latitudes, and there is even a very small maximum formed near the equator; both phenomena result from the changing dip angle of the magnetic field.

However, we see that quantitatively we are in striking disagreement with the observations. The observed variability with latitude is much stronger than our theoretical predictions indicate.

To account for this discrepancy we know of two possible reasons. Electric fields that cause drift of ionization perpendicular to the magnetic field are one possible explanation; and this process was postulated and

discussed in detail by Hanson, to interpret the equatorial anomaly. And, second, we believe also that atmospheric winds, horizontal atmospheric winds, possibly could be partly, or even entirely responsible for the observed global distribution of the electron density.

Atmospheric winds that blow from low latitudes toward the equator have an upward component parallel to the magnetic field. And so they lift the ionization along these field lines up to high altitudes, where the decrease of the ion loss rate causes an increase in electron density.

To study these wind effects, we think, not only could improve our understanding of the global electron density distribution; but, in turn, once these wind effects are established, we hope that the ionosphere could serve us as a monitor of the atmospheric wind system, which is not very well understood.

So what we have done is construct, by means of spherical functions of low degree, a wind field satisfying certain symmetry conditions, one of which (for example) requires that the wind velocity must be zero at the equator during equinox. We then came up with a wind field, also shown in Figure 1 (right half), where the wind velocity parallel to the magnetic field is plotted versus geomagnetic latitude. The wind component is upward at middle latitudes, and downward at high latitudes. The wind velocities are between 50 and 100 meters per second, and allow us to fit the observations quite nicely.

There are two reasons which indicate that such a wind field could actually exist even during daytime. One is that the pressure bulge of the neutral atmosphere is observed to be elongated toward high latitudes. And we think that this pressure bulge could conceal a very shallow minimum at the equator; in fact, we need a decrease in the pressure by only 10 to 20 percent to produce these winds. A second evidence for this wind system seems to come from direct measurements on Explorer XXXII by Newton, who showed that the increase of the time-average density component toward high latitudes is much stronger than the satellite drag data indicate. Such an increase in this density component causes a wind flowing toward the equator. Superimposed on this, of course, there is the diurnal-varying density component derived from satellite drag data—it was discussed by Kohl and King. If we add these two components together, our analysis shows that we can indeed, at least during minimum solar activity, produce winds blowing from middle latitudes toward the equator even during daytime. So these observations seem to support the conclusions we derived from our ionosphere study.

CHAIRMAN:

We have a question from Dr. Schmerling.

DR. SCHMERLING:

These winds of course are associated with electric fields which are deduced from some vapor releases in rocket experiments and from the ground-based geomagnetic observations. Is there any agreement between these observations and the wind field you proposed?

DR. MAYR:

We have not yet checked this. We think that the winds we postulate here could result from the circulation pattern in which vertical winds are included. And, second, they might be associated with an energy input into the auroral zone that drives them in toward the equator. Our wind components are parallel to the magnetic field. I think when you were talking about electric fields the winds would need to be perpendicular to the magnetic field.

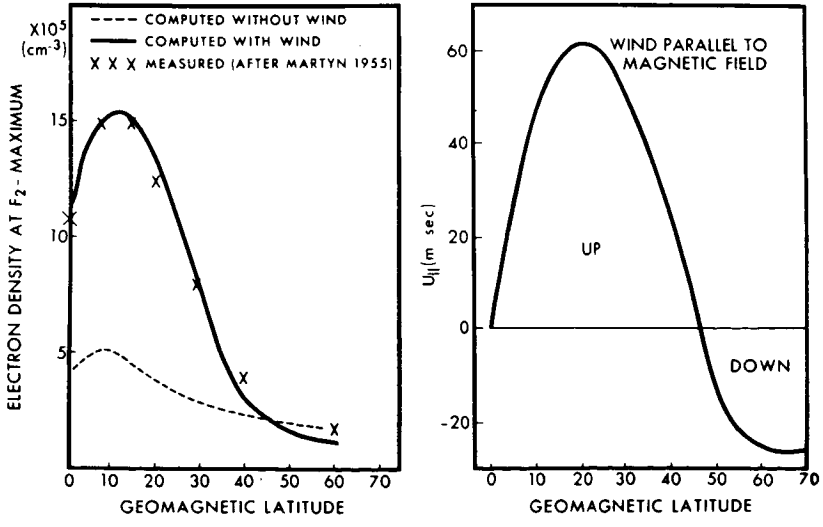

Figure 1

THE POLAR PEAK IN ELECTRON DENSITY

Larry H. Brace

CHAIRMAN:

Related to this is our next talk, in which Mr. Larry Brace will discuss the polar peak in electron density.

MR. BRACE:

The polar peak is a phenomenon that occurs, as the name implies, in the polar ionosphere. It's a topside phenomenon, an enhancement of electron density. This enhancement was first identified in Alouette I topside sounder data, using a rather limited amount of data from the fall of 1963. Nashida found that it occurred in the day side of the polar cap at a latitude where one might expect the neutral point to occur: that is, the point where the pressure from the solar wind forces the field lines back into the tail of the magnetosphere. This was an interesting possibility because it represented an opportunity to see what happens when solar wind particles interact with the earth's atmosphere directly without having to cross field lines.

We don't believe that is the explanation of the polar peak, however, and I am going to attempt to say what we do think causes it today.

Figure 1 demonstrates the kind of data we have been working with from Explorer XXII, a satellite in a polar, near-circular orbit. The altitude is 1,000 kilometers plus or minus 100 kilometers. And these are measurements of electron density shown on a global scale. The South Pole is at the left, and the North Pole is in the middle. The satellite goes to 80° geographic latitude and then on down to the equator, then around the South Pole again. So this is a kind of a gross view using real data points, showing the global pattern in northern summer. This is the summer of 1966, one week of data. The data points here are connected by straight lines when they are obtained from a single pass. What you see here is the day side of the earth and the night side of the earth, and clearly in summertime the polar cap is entirely illuminated.

You may be familiar with this feature. This is the daytime maxima, it's near the magnetic equator. And on the night side there's a double

maxima of electron density with a tendency toward a minimum at the equator. The polar peak is this large enhancement. The density is comparable to what one finds at the equator.

Figure 2 portrays this schematically, possibly a little better. The sun is at an elevation of about 23° to the equator, and the line represents the electron density plotted radially out from the surface of the earth. Here's the daytime equatorial maxima of density, and here are the two maxima on the night side at middle latitudes. The polar peak is here, in between.

I think the thing that is significant about the polar peak and that says something about its formation is that the north end of it, let's say the night side boundary of it, always occurs near the solar terminator where sunlight falls on the polar region.

This changes the picture somewhat. This certainly isn't the location of the neutral point in summer or at any time. What I haven't shown here is that the polar peak does follow the terminator at other seasons as well. When the sun moves farther south, the night side boundary of the peak tends to move southward also, occuring near a zenith angle of about 100°.

This suggests then that the explanation of the polar peak really lies in what forms the trough here at middle latitudes. If such is the fact the polar peak isn't really a polar phenomenon, but has to do with the behavior of the mid-latitude ionosphere. The explanation of the polar peak then lies in the behavior of the trough and in the processes behind the existence of the trough.

Figure 3 is the same as Figure 2 but has superimposed on it magnetic field lines. From the previous talk we saw that there is an interaction between the neutral atmosphere, particularly the winds in the neutral atmosphere, and the ion and electron distributions. And here is just another manifestation of that.

Our argument here is that the trough at middle latitudes is caused by these northward neutral winds at middle to high latitudes. If you recall Dr. Mayr's Figure 1, he had poleward winds in the day side from mid-latitudes northward. We employ these northward neutral winds to argue that their downward component, the ion-neutral drag force, drives the ions down deeper into the F region, causes recombination, and reduces the density at these middle latitudes—and that this itself is the reason for the formation of the polar peak. Otherwise, without these winds, one would expect a much more uniform density as a function of latitude, as Dr. Mayr pointed out.

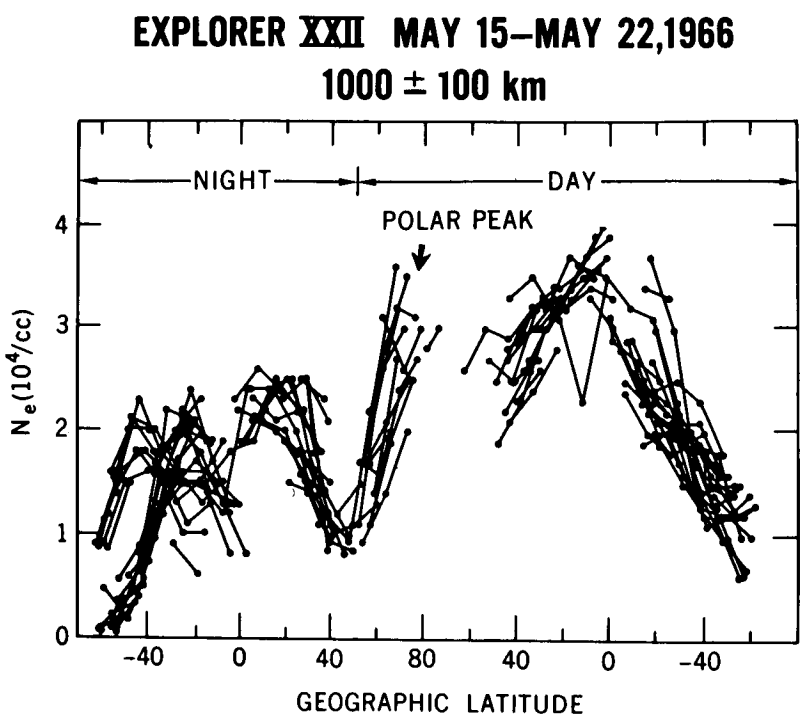

Figure 1

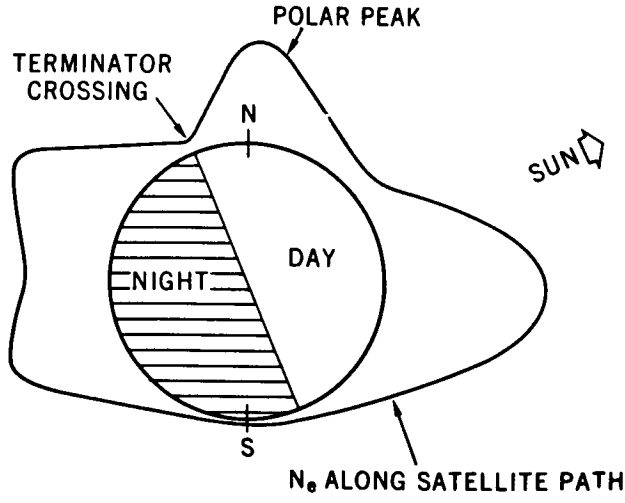

Figure 2

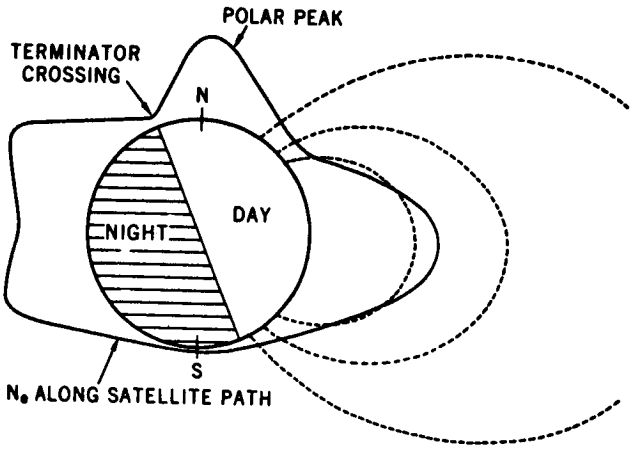
POLAR PEAK
TERMINATOR CROSSING
N
DAY
NIGHT
S
N_e ALONG SATELLITE PATH

Figure 3

PHOTOELECTRONS IN THE TOPSIDE IONOSPHERE

Siegfried J. Bauer

CHAIRMAN:

We will continue in the area now of the ionosphere. Dr. Siegfried Bauer will discuss photoelectrons in the topside ionosphere.

DR. BAUER:

It is well known that the formation of the ionosphere is due to the absorption of extreme ultraviolet in the upper atmosphere. The photoelectrons formed in the ionization process carry excess energy beyond the ionization energy. This excess energy is typically of the order of a few electron volts to a few tens of electron volts. Below about 300 kilometers, this excess energy is quickly dissipated by collisions and contributes to the heating of the upper atmosphere. Above about 300 kilometers, however, the mean free path for these photoelectrons becomes large enough so that they can escape and spiral along field lines and actually contribute to the low-energy particle distribution in the magnetosphere and also cause effects in the conjugate hemisphere.

The existence of escaping photoelectron fluxes was first invoked to explain the rather high electron temperatures which were observed in the topside ionosphere by satellites. There was also indirect evidence for the existence of such escaping photoelectrons from the observation of the pre-dawn enhancement of the 6300 Å airglow, and also the pre-dawn enhancement of electron temperature observed from the ground by Thomson scatter radar. However, there was really no direct measurement or evidence for the existence of these escaping photoelectrons.

The first measurement, or rather let us say, the identification, of photoelectrons in the measured suprathermal electron component was made by means of retarding potential analyzers on the Explorer XXXI. For this particular measurement a specific geometry was utilized. The measurements were performed when the satellite was in darkness but the foot of the field line at about 300 kilometers was beginning to be illuminated by the sun as indicated in Figure 1, where χ is the solar zenith angle.

In Figure 2 we show the increase of the flux of suprathermal electrons having energies greater than five electron volts with sunrise at the foot of the field line, i.e., increasing flux with decreasing solar zenith angle or increasing solar illumination. This makes it quite clear that the suprathermal electrons here are definitely associated with the sun and therefore can be identified as escaping photoelectrons.

Now in addition to the measurement of the fluxes, we also have been able to determine the energy spectrum (shown in Figure 3) of these escaping photoelectrons. This energy spectrum shows a maximum in the range between 5 and 10 electron volts, which is in good agreement with theoretical expectations for such photoelectrons escaping along field lines.

If we take into account the fluxes and energies of these particles, we arrive at a number density for these photoelectrons of a few electrons per cubic centimeter. Therefore, the photoelectrons represent a rather substantial fraction of the low-energy suprathermal electron component in the magnetosphere.

In addition to the heating effects which these electrons can cause, especially the heating of the ambient electron gas by collisions, there is another important aspect of those particles: their energy and fluxes are just right to cause plasma oscillations by the Cerenkov process. In fact, the discovery of the plasma line by the Thomson radar backscatter is dependent on the existence of such fluxes.

The fact that the photoelectrons can cause plasma oscillations which can be converted into radio waves appears to be a rather plausible explanation of some of the radio noise at medium frequencies which we have observed on satellites within the ionosphere and magnetosphere.

GEOMETRY FOR PHOTOELECTRON FLUX MEASUREMENTS

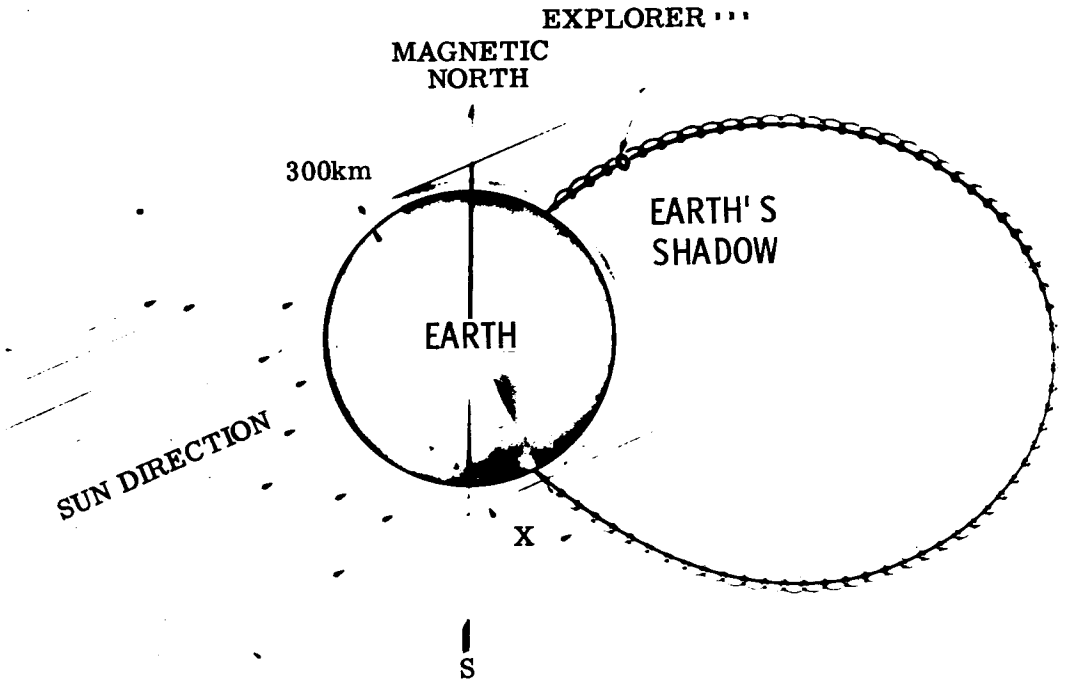

Figure 1

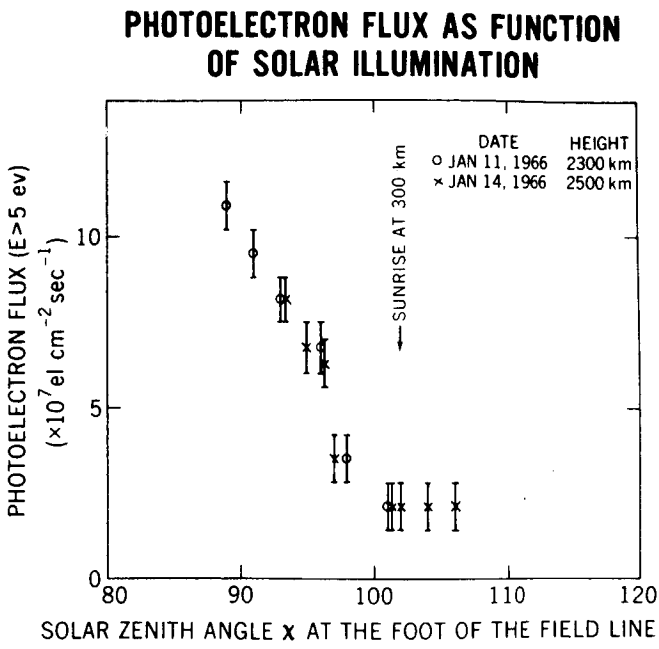

Figure 2

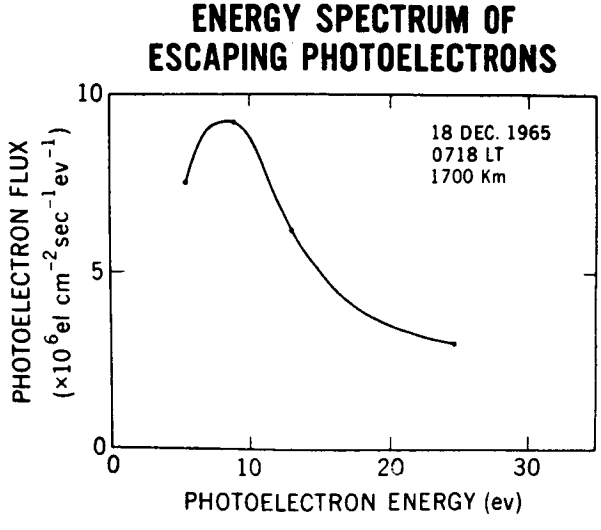

Figure 3

ACCOMPLISHMENTS OF THE WORLD MAGNETIC SURVEY BY POGO SATELLITES

Joseph C. Cain

CHAIRMAN:

As you will have observed, we have gradually moved into the area of electric and magnetic fields and charged particles in space. The next talk in this group will be by Dr. Joseph Cain on the results of the POGO world magnetic survey.

DR. CAIN:

Figure 1 summarizes the main accomplishments to date of the magnetic surveys made by the Polar Orbiting Geophysical Observatories. As you can see, we have moved down in the magnetosphere all the way to the earth's core. From the launch of the first POGO in late 1965 to the present, the two satellites OGO 2 and 4 have acquired enough data - if you reckon that they can completely survey the earth's field in about 10 days - for the equivalent of over 60 magnetic surveys. OGO 2 obtained over 150 days of data in the altitude range 400 to 1,500 kilometers, and OGO 4 over 500 days in a slightly lower polar orbit.

We have shown that we can make vector maps of the earth's field using only measurements of the total field. We no longer need surface magnetic survey data to assist us in this analysis, although we have used such data in the past.

We have used the results of these studies to help us understand the changes in the core field, and also to look at the field variations during both magnetic disturbance and quiet–the Sq variation. We have shown that the auroral ionospheric currents follow the classical two-celled pattern, in contradiction to some recent interpretations that hold the polar currents to be represented by a single cell system. The only other magnetic variation that we have definitely attributed to ionospheric currents is the equatorial electrojet.

Figure 2 illustrates one of the results from our studies of the core field. It shows estimates of the flux emanating from the core as you progressively add various spherical harmonic components of the field from

the field models as determined from surface and satellite data. That is, you extrapolate these models down 2,900 km to the core, where we believe the field originates. The field that we observe is the poloidal leakage from a tightly wrapped toroidal field in the highly conducting core. As you add the higher and higher harmonics, you soon arrive at results which are completely erroneous, since the errors magnify immensely for these higher-order terms. As you can see in the figure, we have used two field models, both of which used POGO data in their derivation. The GSFC(12/66) model, which was the prime basis for the International Geomagnetic Reference Field, used OGO 2 data for 1965.7, plus earlier non-satellite data. The POGO(10/68) model used only POGO data covering the two-year interval 1965.7 to 1967.9.

The result shown here is that, even though the earth's main dipole - as represented by the first two harmonics - continues its slow collapse, the flux from the core remains relatively constant as you add the higher-order terms. The POGO field model shows that if anything, the rate of dipole collapse is now faster than previous estimates. One possible implication of this frozen field idea is that, as the dipole continues to weaken and presumably goes into a reversal, it would become more and more non-dipolar. This might help explain some of the paleomagnetic results which show an apparent wandering of the magnetic pole.

Jumping now from the earth's core into the magnetosphere, Figure 3 gives information on the source of the asymmetric ring current - the DS and Dst variations. We have plotted here for a two-day magnetically stormy period in 1966 the changes in field seen at the OGO 2 satellite every time it passed over the equator versus the variation seen at the nearest surface magnetic observatory. Since the plane of the orbit moves very slowly in local time, all of the passes during this interval occur near one local time at ascending node and near another on the southward traversal. The ring current is asymmetric with the larger field depressions occurring in the afternoon (compared with those in early morning). Since the surface and satellite values correlate exactly within the $\pm 10\gamma$ accuracy of the points, we conclude that neither DS nor Dst could arise from ionospheric currents and hence the source must be in the trapped-particle regions outside the ionosphere. We understand that this result will be a problem to the theories which have attributed the atmospheric heating following magnetic disturbance to ionospheric currents.

WORLD MAGNETIC SURVEY
ORBITING GEOPHYSICAL OBSERVATORIES

OGO-2 OGO-4

1965.8 - 1969.0

ONLY COMPLETE SURVEY OF THE GEOMAGNETIC FIELD
(Have surveyed more than 60 times)

SHOWN THAT:

1) WORLD MAGNETIC MAPS OF VECTOR GEOMAGNETIC FIELD AND ITS SECULAR CHANGE CAN BE OBTAINED USING ONLY SATELLITE TOTAL FIELD DATA

2) FLUX OF FIELD FROM EARTH'S CORE REMAINS CONSTANT AS MAIN DIPOLE CONTINUES TO COLLAPSE

3) SOURCE OF BOTH ASYMMETRIC AND SYMMETRIC RING CURRENT IN LOW LATITUDES LIES OUTSIDE THE IONOSPHERE

4) TWO-CELL MODEL OF POLAR IONOSPHERIC CURRENTS DURING MAGNETIC STORMS IS VALID

Figure 1

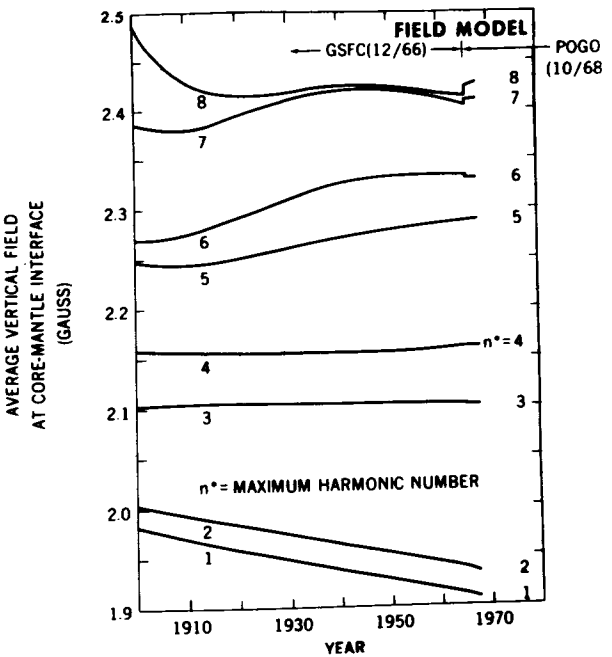

Figure 2

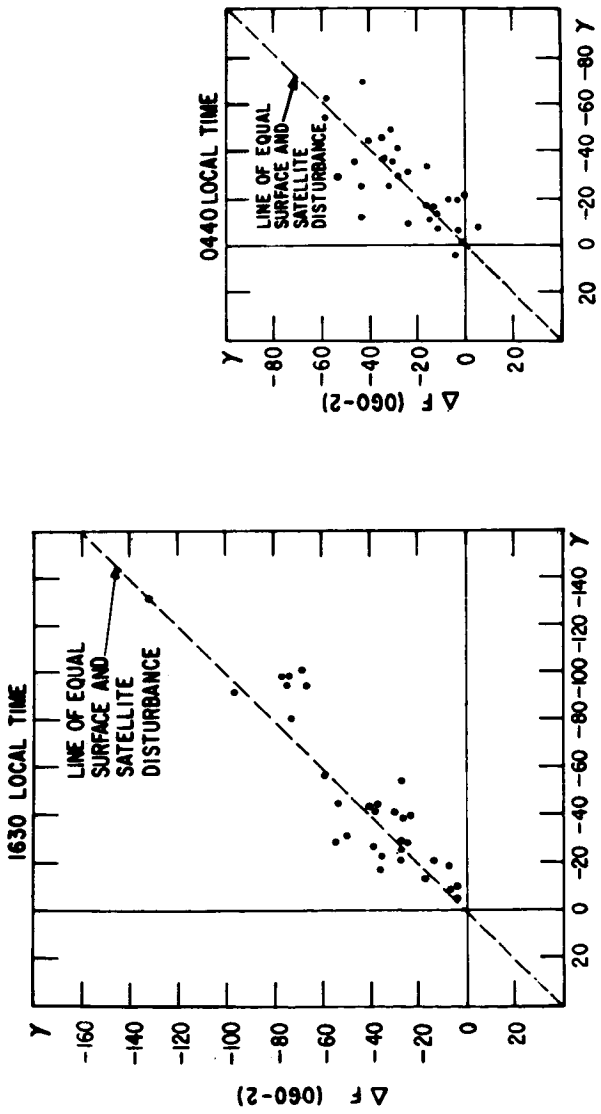

DISTURBANCE AT 060-2 VS. DISTURBANCE AT SURFACE MAGNETIC OBSERVATORIES, MARCH 13–15, 1966

Figure 3

ELECTRIC FIELD STUDIES WITH BARIUM IONS

Eugene M. Wescott

CHAIRMAN:

I'd like to go on then to the next talk, which concerns electric field studies carried out with barium ions. This will be presented by Dr. Eugene Wescott.

DR. WESCOTT:

In order to find solutions for several outstanding problems in magnetospheric and ionospheric physics, we require electric field measurements. A very powerful method for making these measurements has been developed over the last several years. This is to observe the drift motion of barium ion clouds.

Now, if we release barium vapor from a sounding rocket above, say, about 200 kilometers during twilight conditions, part of the barium becomes ionized and forms a visible ion cloud which can be tracked for as long as it is illuminated by sunlight. The barium ions will drift in the electric and magnetic fields, with the velocity given by $[\vec{E}\times\vec{B}/B^2,]$ in a direction perpendicular to both $\vec{E}$ and $\vec{B}$.

A very important fact is that the magnetic field lines are very highly conductive, and thus they are essentially equipotentials. That means that we can measure an electric field in the upper ionosphere and transfer the potentials of this field out to the magnetosphere and thus infer magnetospheric convection.

Now, we can observe magnetic variations on the ground and deduce the ionospheric current system, but we cannot know what electric field is driving this current system. That is because the ionospheric conductivity is not a scalar quantity. That is, the electric field is not necessarily in the same direction as the current.

This problem is illustrated in Figure 1. In the region above 200 kilometers the equation $\vec{E} + \vec{V}\times\vec{B} = O$ holds, and this is the basis of our method. The magnetic field is downward, and the electric field is perpendicular to it. The ions and the electrons move in the same direction

with the same velocity, so there is no current. In the lower ionosphere, at around 110 kilometers, there are many more collisions with ions than with electrons; and thus current can flow. We have two possible conductivities perpendicular to the magnetic field line. In the Hall conductivity, the current is perpendicular to both $\vec{E}$ and $\vec{B}$. The electrons still move in the same direction but the ion velocity is essentially zero, so a Hall current flows in the opposite direction to vi. In the Pedersen conductivity, the current flows in the same direction as $\vec{E}$. Now, we don't really know the relative importance of these two conductivities to the ionospheric currents. So that's why we need to measure the E field.

A problem that my colleagues and I have solved involves the intense electric currents which flow in the auroral zone, called the auroral electrojets.

Figure 2 illustrates schematically the main features of these currents on a map looking down on the North Pole. This is the two-cell model which Dr. Cain referred to. On the evening side we have a strong eastward current. On the morning side we have a stronger westward current. And in the 22^h region they overlap.

By a series of barium release shots from northern Norway under varying conditions, we have shown that the barium velocity is eastward on the evening side; meaning an electric field perpendicular to the current, and of a magnitude of about 50 millivolts per meter. On the morning side we find again $\vec{E}$ perpendicular to $\vec{V}$, in the opposite direction, and of a magnitude of up to 130 millivolts per meter. In the overlap region we find a very sharp transition of direction.

This means that now we know the electrojets are Hall current essentially. Furthermore, we can transfer these electric field measurements out to the magnetosphere and infer the convection pattern. Further measurements are required in the polar cap to verify that Hall current is the predominate current there also.

I'd like to illustrate another feature of barium work. Across the bottom of Figure 3 is an auroral arc, showing a highly-rayed structure aligned along the magnetic field. The spherical shape is a neutral barium cloud. At the top is an ionized barium cloud which at this time was in the same magnetic field shell, or on the same field lines, as the aurora. You see it's also showing the very highly field-aligned rayed structure which we are seeing in the aurora. This is a common feature that is seen in barium clouds, and from this we have made the conclusion that many of the features which we see in auroras are due to a basic structuring which has occurred in the ionosphere. That is, auroral rays are not being caused by

events way out in the magnetosphere, but are a result of inhomogeneities in the ionosphere.

MEMBER OF AUDIENCE:

How does this work compare with Aggson's direct probe measurements?

DR. WESCOTT:

We have made a couple of direct comparisons – well, I say "direct," they were done at the same time (10 minutes to a half-hour separated in time). The barium clouds on those occasions saw very high fields so they had moved out of the area by the time Aggson's direct probe technique came on. However, we did see the same order of magnitude fields in the same region where aurora had existed. And we are quite confident the two methods are comparable.

CHAIRMAN:

Yes, Dr. Newell?

DR. NEWELL:

What makes barium the substance chosen for this rather than something else?

DR. WESCOTT:

Barium is essentially the only element that has been found which will ionize in the ultraviolet and give you resonant scattering in the visible spectrum.

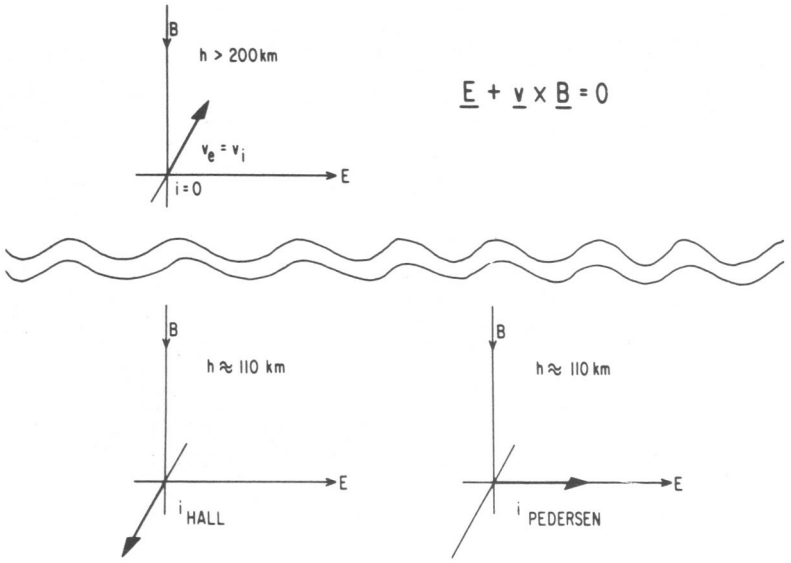

Figure 1

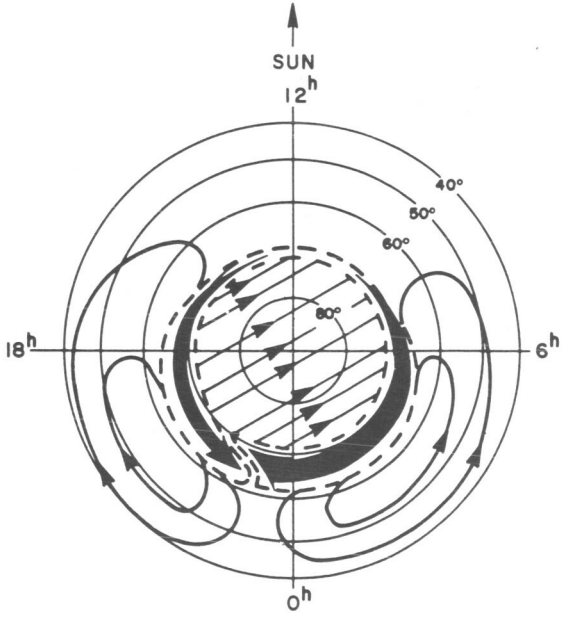

Figure 2

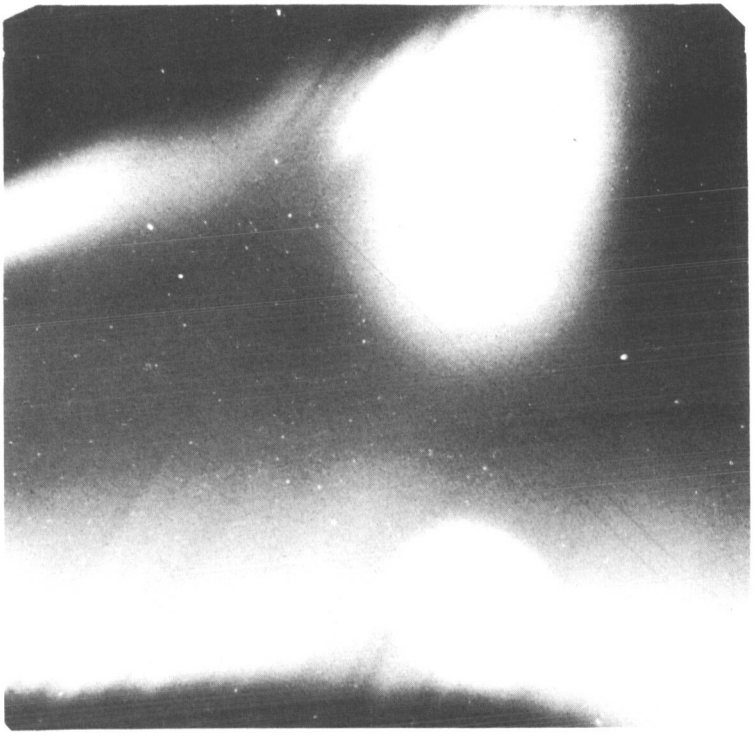

Figure 3

AURORAL ELECTRONS

David S. Evans

CHAIRMAN:

The next talk will be on the subject of auroral electrons, by Dr. David Evans.

DR. EVANS:

Energetic electrons have long been known to precipitate into the atmosphere to produce visual aurora. The explanation for this seems to be linked with the answers to the questions: How and where were these particles energized? Why do they precipitate into the atmosphere?

My approach to the answers to these questions has been to study the electron beam itself in the hope of finding characteristics in the electron particles—time variations, intensity variations, energy spectra—that could be linked to specific mechanisms of energization or precipitation.

Figure 1 summarizes some of the observables in a particle beam that would be useful in this respect.

For example, one might find structure or peaks in the energy spectra which you could infer were the result of acceleration by electrostatic means, allowing the charged particle to fall through a potential difference.

A smooth spectrum, on the other hand, would be more indicative of statistical processes, wave particle interactions, Fermi acceleration, and the like.

Time variations are another observable in the particle beam. A periodic time variation would suggest, to me at least, that a wave particle interaction played an important role in the particle's behavior.

Also in the time realm, if one has a transient change in the particle flux, you have the opportunity to do a velocity dispersion analysis on your data in an effort to find out where in the magnetosphere this change in the particle flux was initiated. This, of course, is of great interest.

Figure 2 shows an electron energy spectrum that was obtained above an active aurora a year ago. It is very striking, I think. You have an extremely prominent peak at about 3 kilovolts energy.

I think it is also important that the flux falls off very rapidly indeed at higher energies. The e-folding energy over that portion of the spectrum above 3 kev is much less than a kilovolt.

This sort of energy spectrum has been observed numerous times in the past few years as people have begun to study electrons of less than 10 kilovolts energy; and in fact, I think, it is spectra of this type which can be termed typical auroral electron spectra.

It seems most satisfying to ascribe particles having this sort of spectra to some sort of electrostatic acceleration mechanism, these electrons having simply fallen through 3-kilovolt potential difference. Certainly potentials far greater than 3 kilovolts are available in the magnetosphere.

The problem seems to be to find a method or a mechanism which can efficiently utilize these potential differences for the acceleration of charged particles.

Figure 3 shows an auroral electron beam of an entirely different character. Here we see large numbers of energetic electrons; electrons greater than 60 kilovolts, and they act in a very dynamic fashion. This is a high-time-resolution plot, only a little over a second's worth of data; and you see these large, quasi-periodic fluctuations, particularly in the 60-kilovolt electron flux.

The frequency of these pulsations is about 10 cycles per second.

There were other characteristics in this particular auroral electron beam that were of interest but are not displayed in Figure 3. First, the electron energy spectra exhibited a peak, similar to that shown in Figure 2, at about 6 kilovolts. Second, although the 6-kilovolt beam of electrons in this peak was extremely intense indeed, they did not show fluctuations of nearly the magnitude that we saw at 60 kilovolts.

Using these data from four different energy detectors (as shown in Figure 3), we did a cross-correlation analysis and we found there were no time differences between fluctuations observed at energies ranging from 8 to 120 kilovolts. This led us to conclude that the modulation mechanism, whatever it was, could lie no further than a few thousand kilometers from the surface of the earth.

Well, after considering a number of conceivable modulation mechanisms, the one I finally proposed was in fact not a modulation mechanism but an acceleration mechanism. The picture was that some very dynamic process was at work rapidly energizing electrons to in excess of 50 kilovolts. The time scale for the acceleration was something like 10 or 20 milliseconds.

The low-frequency fluctuation, the 10-cps periodicity, was accordingly thought to be a growth and decay of this dynamic acceleration mechanism.

The fact that the low-energy electrons exhibited a peak in the energy spectra at 6 kilovolts, and also the fact that the process presumably was at work in the upper ionosphere, further led us to specify this dynamic mechanism as being a beam plasma instability and the 50-kilovolt electrons as being runaway electrons.

This sketch of an ionospheric acceleration mechanism was taken up by Perkins at Princeton in a quantitative fashion, and this process of beam plasma instabilities in the upper ionosphere seems to be a very reasonable one indeed.

This particular observation, I feel, is important in two respects. First, it is one of the very few electron acceleration mechanisms for which there seems to be a good basis in theory and experiment. Second, the location of the mechanism in the upper ionosphere serves to refocus our attention on this local region of space for further explanations as to auroral behavior.

Some measurable parameters of auroral particles which may aid in understanding their acceleration:

A. Energy Spectra

1. **Structured - may indicate that d.c. electric fields governed the acceleration.**

2. **Smooth - characterized by a kT - indicates a statistical energization process.**

B. Time Variations

1. **Periodic - may indicate instabilities or wave-particle interactions play a role.**

2. **Velocity dispersion - can in principle lead to knowledge of the position of the acceleration mechanism.**

Figure 1

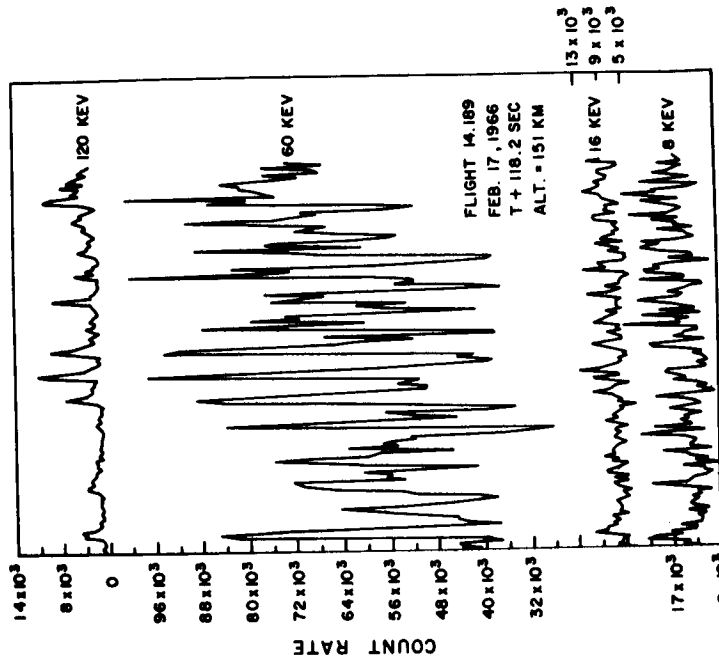

Figure 3

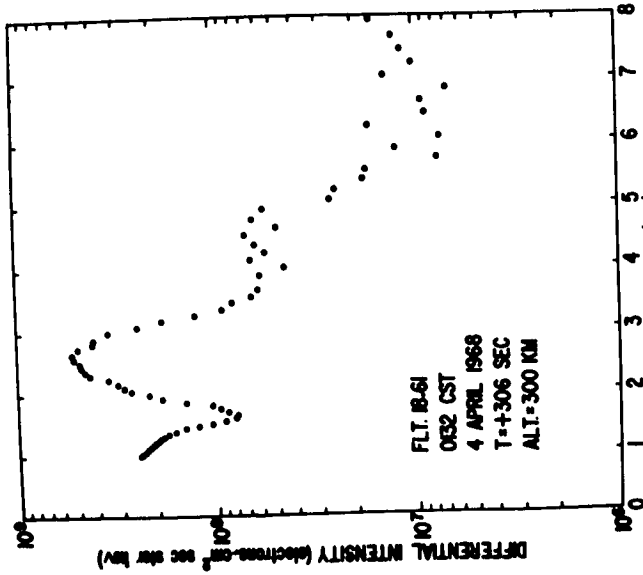

Figure 2

PARTICLE ACCELERATION MECHANISMS IN THE MAGNETOSPHERE AND ON THE SUN

Donald J. Williams

CHAIRMAN:

Since the discovery of the radiation belts encircling the earth, we have been interested in the question of particle acceleration mechanisms. Our next speaker is Dr. Donald Williams, who will tell you about his work in this area of particle acceleration mechanisms in the magnetosphere and on the sun.

DR. WILLIAMS:

It is now known, and it has been experimentally observed, that convection processes play a very important role in supplying low-energy particles and plasma to the outer radiation zone.

However, it also appears that more energetic particles, for example, electrons of greater than ~100 kilovolts, are not convected into these stable trapping regions during magnetic storms – nor can their appearance be explained by any of the normal modes of diffusion through the earth's magnetic field.

Figure 1 illustrates the appearance of these relativistic electrons deep within the earth's magnetosphere. In this figure we have plotted the relative intensity of energetic electrons and the time of their arrival at the point of observation (the time of arrival being measured from the start of the magnetic storm) as a function of L value. For these distances the L value represents very nearly the distance at which the earth's line of force crosses the geomagnetic equator.

We show points for each line of force – those obtained from the near equatorial regions (open circles), and those obtained from the foot of the field line at an altitude of 1,100 kilometers (solid circles). Therefore Figure 1 presents a very thorough sampling of all the lines of force through the outer zone.

In addition, these data are shown for the two energy ranges, greater than approximately 300 kilovolts and greater than approximately 1 Mev.

The important feature to note in Figure 1 is that both at low altitudes and in the equatorial regions a minimum occurs in the arrival-time plots for both energies. This leads to the conclusion that the bulk of energetic electrons associated with main phase magnetic storms appear first deep within the trapping regions and subsequently follow diffusion processes leading them to lower and higher altitudes.

Note also that, in the region where these energetic electrons appear initially, they appear in the greatest numbers. These are characteristics of the energetic electron population observed in many geomagnetic storms.

Another feature of interest in Figure 1 is that approximately one and a half to two days after the initial start of the storm there can be seen, in the region of L = 4 to 5, either secondary maxima or secondary minima, or very clear discontinuities in the trend of the curves. This effect is associated with a secondary substorm occurring approximately one and a half days after the start of the storm and injecting a fresh supply of energetic electrons in these higher altitude regions.

Further studies of several storms indicate that this effect is indeed general, that is, that these energetic electrons not only are associated with the large-scale main phase magnetic storms but are also associated with the smaller substorm activity.

A point of interest which I would like to mention here is the relation between the large-scale main phase storm and the smaller substorm phenomenon. It is now thought that the main phase storm may be due to a pumping action whereby the smaller substorms occur occasionally at a very high frequency and thus integrate into the large-scale magnetic storm effect. We will refer back to this point later.

I would like at this time to mention briefly two additional characteristics which we have observed concerning the appearance of these energetic electrons within the stable trapping regions.

First, the larger the storm the closer in toward the earth is the region of initial electron appearance. That is, the acceleration region moves even further into the stable trapping region as the size of the geomagnetic disturbance increases.

Second, using simultaneous plasmapause data, we have found that the acceleration region responsible for these energetic electrons is located outside the plasmasphere. That is, it is located in the low-density region of the earth's magnetosphere.

These acceleration mechanisms are as yet unknown; and, rather than speculate on possible candidates at this time, let us accept as a fact that, during magnetic storm and magnetic substorm activity, mechanisms do exist which are capable of producing relativistic electrons in copious numbers.

Given this fact, I would like to turn now to examine the possibility that similar processes may be occurring at the sun and are responsible for some of the characteristic solar proton behavior observed in interplanetary regions.

To illustrate this, Figure 2 shows a plot of low-energy (1 to 10 Mev) protons as observed at 31 earth radii by Explorer 34 with instrumentation in the Solar Proton Monitoring Experiment.

The top curve displays these proton intensities. The bottom three curves show the interplanetary magnetic field simultaneously observed on Explorer 34. It shows the magnitude of the field, the solar ecliptic longitude, and the solar ecliptic latitude. These data have been generously made available by Drs. Ness and Fairfield of GSFC.

The point of interest in Figure 2 is that this small event which is observed by our detectors is seen consist of a series of pulsations which integrate into the larger overall event seen here. The period of these pulsations is approximately one hour.

An additional interesting fact is that at the same time and place there are no local magnetic effects occurring which can produce this pulsation. Therefore, if we are able to eliminate magnetic control from the observed proton intensity fluctuations, we may possibly be looking down through the flux tube at the solar surface and observing the source of these low-energy protons. We may thus be observing a series of substorms on the solar surface occurring at a sufficiently high frequency to integrate into the larger overall event seen in Figure 2. This is analogous to the way in which geomagnetic substorms are thought to integrate into a larger magnetic main phase disturbance in the magnetosphere.

This type of analogy becomes more attractive when we recall from Figure 1 that very energetic particles are indeed produced during such magnetic activity. Thus magnetic and plasma activity at or near the solar surface may be producing many smaller substorm type events on a frequent basis which only occasionally build up to frequencies that integrate into an easily observable proton event in interplanetary space. These effects may be quite analogous to similar types of activity occurring within the magnetosphere.

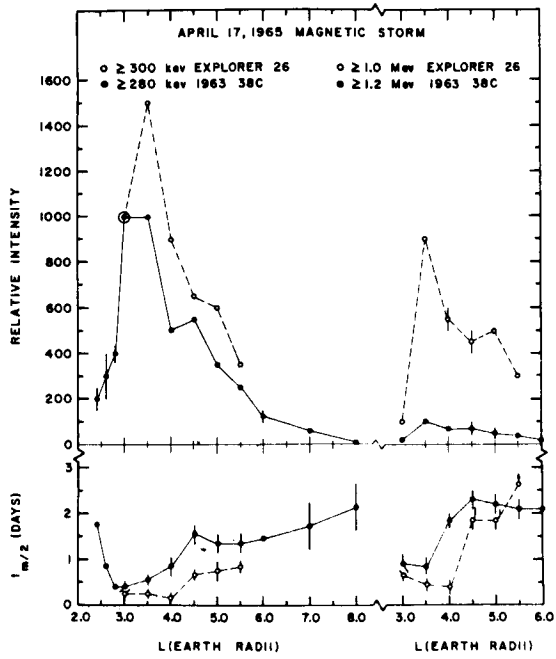

Figure 1

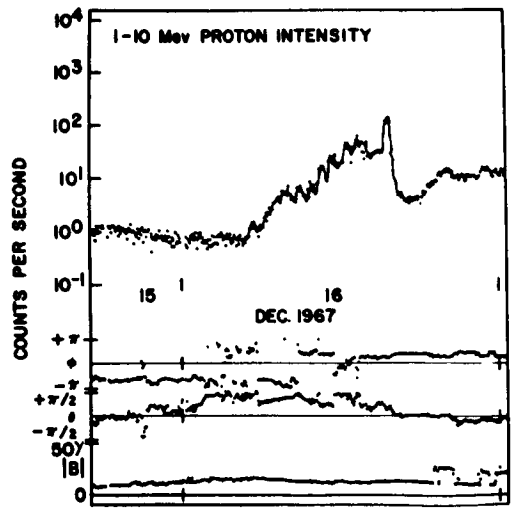

Figure 2

DIFFUSION OF CHARGED PARTICLES

Thomas J. Birmingham

CHAIRMAN:

The next paper is a theoretical one but related to the same subject. Dr. Thomas Birmingham will discuss the diffusion of charged particles.

DR. BIRMINGHAM:

My work deals with the motion of energetic charged particles in the earth's magnetosphere. I am particularly interested in how such particles interact with time-fluctuating electric fields which may be present.

It is our present understanding of the magnetosphere that quasi-steady fluxes of trapped particles exist in spite of the simultaneous presence of strong loss mechanisms. Clearly, a strong compensating replenishment mechanism must also exist.

I shall show that fluctuating electric fields drive a radial transport of charged particles toward the earth and hence can act as the replenishment mechanism by bringing in particles deposited at the magnetospheric boundary.

My calculation is carried out with the magnetospheric model which is shown in equatorial cross-section in Figure 1. For orientation purposes, the earth is a point at the origin of coordinates, $L = 0$. The magnetic field is a dipole magnetic field, is static, and in this figure is everywhere directed perpendicularly outward. The magnetic field, being a dipole field, falls off in magnitude with radius as I/L^3.

Across the magnetosphere from dawn to dusk is a spatially uniform but time-fluctuating, and I emphasize time-fluctuating, electric field. This electric field is intended to represent the so-called convection electric field which exists in the earth's magnetosphere. As such, it has a typical magnitude of 1mv/m, and typically varies with time on a scale of one hour.

Let's now inject a kilovolt particle into this model magnetosphere and follow its motion as we progressively add elements to the model. Just for the sake of simplicity we will restrict our attention to a particle whose motion is totally confined to this equatorial plane.

With no electric field present, the motion of a particle in the static dipole magnetic field is the sum of two components. There is first of all a millisecond gyration about the local magnetic field line with a space scale of kilometers. Kilometer distances are virtually infinitesimal on the scale of this figure, so the gyro motion hasn't been shown here. Shown as the solid circle is the second component of particle motion in the dipole field: a slow, one-hour azimuthal drift about the earth. This azimuthal drift is the result of the radial drop-off in the dipole magnetic field strength.

When we next add to the static dipole magnetic field a static electric field, a particle is alternately energized and de-energized depending on the sign of its charge and whether it has a component of motion parallel or anti-parallel to the electric field. Its dipole drift path is distorted into the dashed curve. However, after each excursion of 2π in longitude, the particle returns to exactly the same radial position. Hence we conclude that a small static electric field is not very effective in producing large radial displacements of particles.

However, if the electric field varies with time over a particle's azimuthal excursion, the particle can be energized for a relatively large portion of its drift path. In this case, it returns to its initial longitude but displaced towards the earth a small amount. This small amount, ΔL, has been exaggerated for schematic purposes in this figure. Even in the small convection electric field, however, a particle can undergo over a number of drift periods a large radial excursion via the integrated effect of many such small displacements ΔL.

I have done a theoretical calculation using this model magnetosphere with a time-dependent electric field. I have derived and solved a diffusion equation for a distribution of particles in this magnetosphere. One result of this calculation is shown in Figure 2.

Here $\langle Q \rangle$, which is particle flux (differential in energy and solid angle) divided by particle energy, is plotted against L, distance from the earth in units of earth radii. $\langle Q \rangle$ evolves from an initial δ -function at $L = 8$. The various curves are the form of $\langle Q \rangle$ at subsequent later times. For conditions which are appropriate to the magnetosphere, one unit of the parametric time T is roughly one day.

Features that are to be noted in this figure are the inwardly moving maximum and the asymmetric radial shape. These are features which have also been observed on experimental data in the few instances where it has been possible to follow with time an inwardly diffusing distribution of particles.

The theoretical significance of the result is that the diffusion proceeds at a rate which is 1 to 2 orders of magnitude faster than that in other mechanisms which have been proposed to diffuse particles.

My conclusion is that the mechanism I have discussed is one capable of compensating for the large estimated losses of particles in the magnetosphere.

SCHEMATIC DIAGRAM OF EQUATORIAL SLICE THROUGH MODEL MAGNETOSPHERE

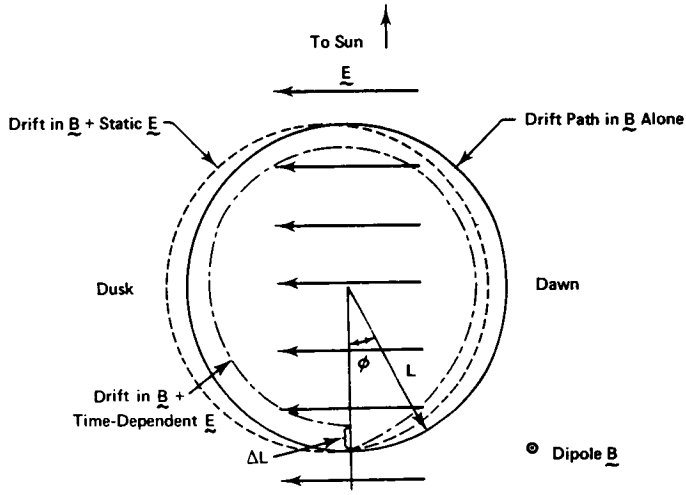

Figure 1

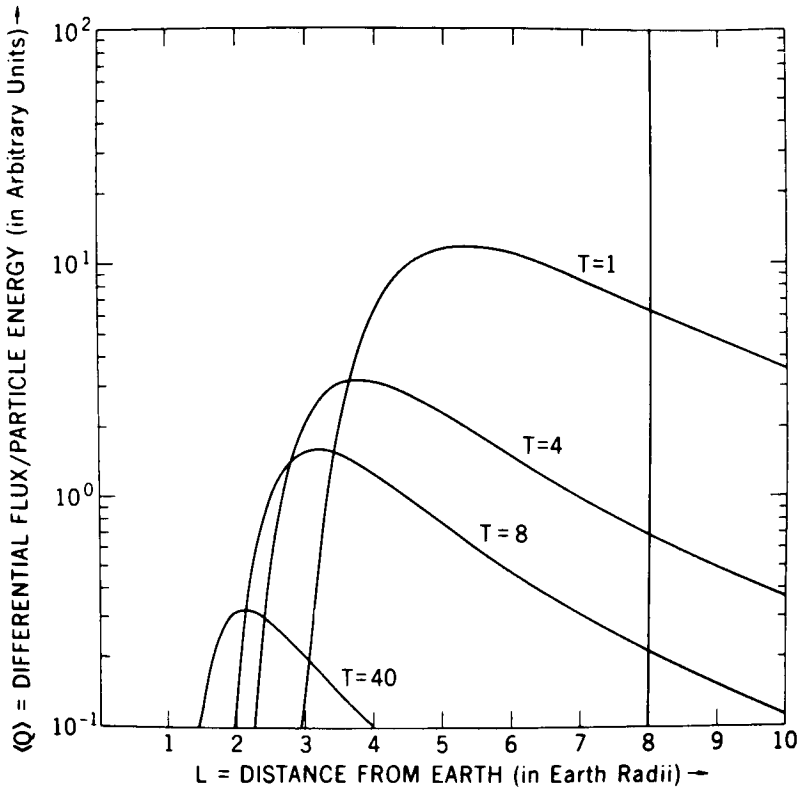
⟨Q⟩ = DIFFERENTIAL FLUX/PARTICLE ENERGY (in Arbitrary Units)
10^2
10^1
10^0
10^{-1}
T=1
T=4
T=8
T=40
1
2
3
4
5
6
7
8
9
10
L = DISTANCE FROM EARTH (in Earth Radii)

Figure 2

POSITRON ANNIHILATION IN HELIUM – THEORY AND EXPERIMENT

Richard J. Drachman

CHAIRMAN:

Our anchorman for this first session this morning is Dr. Richard Drachman. He will tell us about his work in positron annihilation in helium – theory and experiment.

DR. DRACHMAN:

Quantum mechanical calculations of low-energy electron scattering from atoms and molecules are interesting in themselves. They are a lot of fun to calculate. This task would also be useful, however, in studies of atmospheres, ionospheres, and the interstellar medium. Direct computations, however, i.e., solution of differential equations, are limited by present machine capacities.

I have examined a simple theoretical model of the positron-helium system at low energies. The positron provides a much more exacting test of model wave functions than does the electron, since its annihilation properties must be predicted along with the scattering cross-section.

In addition, the positron is an interesting constituent of interstellar space, being produced in cosmic ray collisions and perhaps also in the hypothetical anti-matter regions of the universe.

To understand the theoretical model, it is useful to imagine what will happen as the positron approaches the helium atom. And to save money for the laboratory I have eliminated the first figure I was going to have.

The nucleus of the atom is heavy and positively charged. Around it we have atomic electrons which are light, negatively charged, and rather easily perturbed by external electric fields.

Now, imagine that this is a positron. As the positron approaches the atom more closely, the atomic cloud–the cloud of electrons–distorts, moving toward the positron by an amount which depends on the elasticity

or polarizability of the atom, which is something that can be computed. This disturbance in the charge produces an electric field that reacts back on the positron, accelerating it in an inward direction. The inward acceleration is finally stopped only by the strong repulsion between the helium nucleus and the positron. This combination of long-range attraction and short-range repulsion determines the qualitative features of the scattering wave function.

The model I have used builds in these features from the start, leaving two functions initially undetermined. It is these functions which are then calculated numerically with the help of a certain variational principle.

The basic experiment needed to check the validity of the model would be a scattering measurement at several well-defined energies. Such experiments are quite difficult, but preliminary results are expected soon.

However, another test of the theory is already available. It makes use of a precise and elegant angular correlation experiment performed by A. T. Stewart, working at the University of North Carolina.

You must realize that whenever, in the course of the scattering process, the positron is close enough to one of the atomic electrons, there is a certain chance of pair annihilation. Such annihilation results in the creation of two gamma rays which emerge from the atom and can be detected.

In Figure 1 you see a diagram of Stewart's apparatus. It is essentially a device for measuring the angular correlation between the two outgoing photons produced by positrons from Cu^{64} that slow down before annihilating in the liquid helium.

In the first approximation these photons emerge in opposite directions. Any deviations from exact opposition are due to the fact that the electron and positron, at the instant of annihilation, may not be at rest. It is their momentum distribution which gives rise to a spread around 180 degrees in the angular correlation. And this spread in turn can be obtained from the positron-helium wave function.

In Figure 2 you see the results. The points are experimental, normalized to 1 at zero angle. The curve is the result of my calculation. The agreement of the points with the curve is very good, and is a fairly significant test of the correctness of the calculated wave function.

It is interesting that the distribution is narrower than you might expect if you examined the momentum distribution of the undisturbed

atomic electrons alone. A partial explanation of this comes from the fact that the highest electron speeds occur in the inner parts of the atom. The repulsion of the nucleus prevents the positron from really penetrating to this region.

Until detailed experimental scattering results are reported, the good agreement shown here is the best evidence for the correctness and usefulness of the simple approximation that I have described.

MEMBER OF AUDIENCE:

I would like to point out that very similar experiments have been performed to measure the Fermi surfaces in solids.

DR. DRACHMAN:

Right. The same technique is used, and Stewart's is one of the first experiments using it on atomic momentum distribution.

SCHEMATIC DRAWING OF THE EXPERIMENTAL ARRANGEMENT

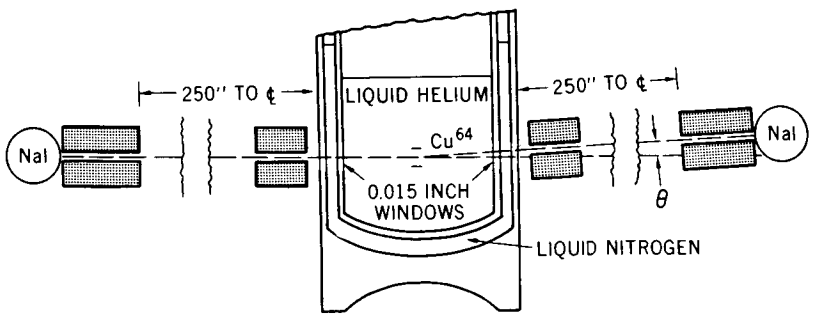

Figure 1

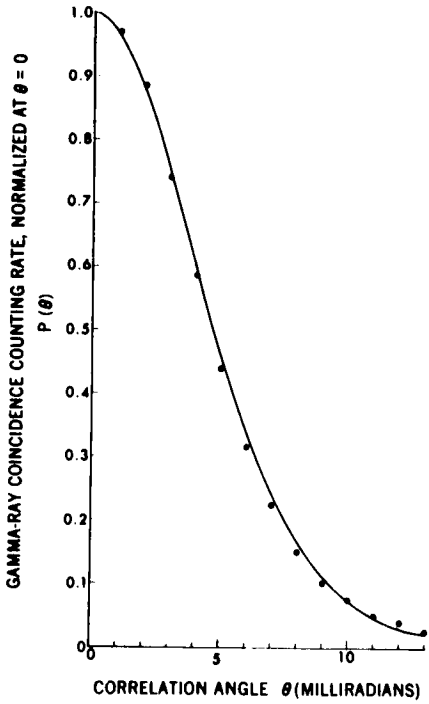
GAMMA-RAY COINCIDENCE COUNTING RATE, NORMALIZED AT θ = 0
P (θ)
1.0
0.9
0.8
0.7
0.6
0.5
0.4
0.3
0.2
0.1
0
0
5
10
CORRELATION ANGLE θ (MILLIRADIANS)

Figure 2

EVOLUTION OF THE ATMOSPHERES OF THE EARTH AND VENUS

Ichtiaque S. Rasool

CHAIRMAN:

The continuation of our program concerns the planets. The first speaker in this session will be Dr. Ichtiaque Rasool, who will speak on the evolution of the atmospheres of the earth and Venus.

DR. RASOOL:

The most important achievement in planetary sciences during the last year has been the exploration of Venus by Mariner V and Venera IV and also the determination of the radius of the solid surface of Venus by earth-based radar.

Having worked as a co-experimenter on the Mariner V occultation experiment, I would like to report on the progress we have made in determining and deriving a coherent picture of the atmosphere of Venus which will be consistent with the three sets of data obtained by the three means mentioned above.

Figure 1 shows the measurements made by Mariner V and Venera IV. This is the pressure versus height. It now seems certain that the last measurement reported by Venera IV was made not at the surface but at about 25 kilometers above the surface. So, in order to get the conditions of the surface of Venus, one has to extrapolate down 25 kilometers.

One such extrapolation assuming adiabatic equilibrium is shown in Figure 1. It gives a pressure of about 75 to 100 times the pressure at the surface of the earth.

A similar temperature curve would give a surface temperature of 730°K to 750°K.

So this is what we know of the atmosphere of Venus. The pressure is about 100 times higher than the pressure at the surface of the earth. The atmosphere is mainly carbon dioxide and the surface temperature is about 700 degrees.

Now I wish to present an explanation of a puzzle which seems to exist regarding the composition of the Venus atmosphere in comparison with that of the earth. Venus and the earth are of the same size and mass, and presumably were formed out of the same material in the solar system. However, when we compare the two atmospheres they seem to be quite different.

Figure 2 shows the amount of volatiles on the two planets: earth at 300°K, Venus at 700°K. You first see that the proportionate amount of carbon dioxide on Venus is about 70,000 times higher than that in the atmosphere of earth. But at the same time we have about the same high amount of carbon dioxide in the crust of the earth. That is not very surprising, because Harold Urey several years ago pointed out that in the absence of water most of the carbon dioxide on Venus would remain in the atmosphere. And recently Mueller and other people have shown that high temperature also allows the carbon dioxide to stay in the atmosphere.

The amount of nitrogen is also about the same on the two planets. But the puzzle is that at the temperature of Venus we should have all the oceans which are on the earth in the atmosphere of Venus but we see that the amount of water in the atmosphere of Venus is less by a factor of about 10^4 to 10^5 !

I have made calculations to see whether we could explain this deficiency by photodissociation of water and subsequent escape of hydrogen.

Now, in order to have 300,000 grams of water escape from Venus we need escape flux, and therefore a dissociation rate of 10^{11} /cm^2 /sec. On the earth the dissociation rate is 10^6. We have to account for an extra factor of 10^5.

Now, the two special circumstances of Venus would give us this factor of 10^5. First, the tropopause temperature on Venus is about 50 degrees higher than on the earth. This allows 1,000 times more water to go from the troposphere to the stratosphere. Second, the absence of free oxygen allows the ultraviolet flux to come down in the stratosphere and this is also a factor of 1,000. So we could get a dissociation rate of as much as 10^{12} . We calculate the 10^{11}/c diffusion velocities and the escape flux for the Venus conditions and we find that a hydrogen escape flux of 10^{11} /cm^2/sec is very plausible.

So this then seems to be the mechanism by which Venus has lost its water. The water is probably being continuously exhaled from the interior and dissociated at the top of the atmosphere at the same rate. The small amount of water that is observed in the atmosphere is that which is in transit from the ground to the top of the atmosphere.

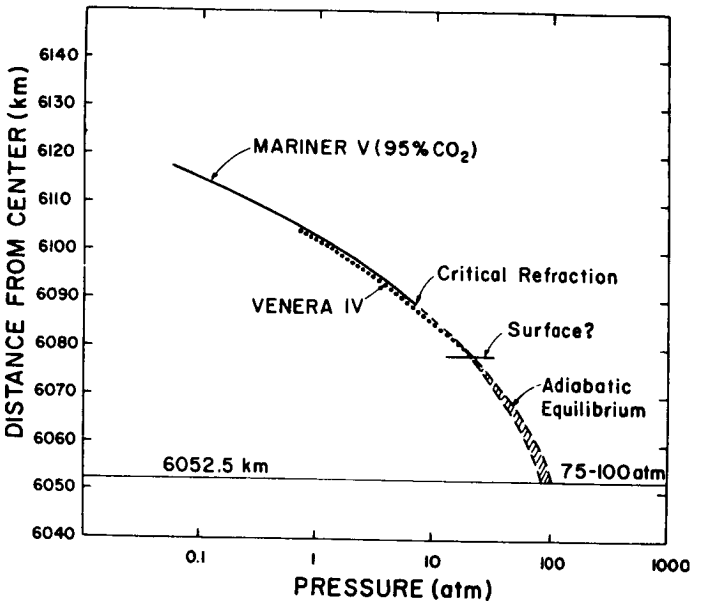

Figure 1

		EARTH 300 °K (g/cm^2)	VENUS 700 °K (g/cm^2)
CO_2	atm.	~1	70,000
	crust	60,000	–
N_2	atm.	800	< 5000
	crust	~2000	–
H_2O	atm.	~1	~10
	oceans	300,000	–

Figure 2

COMPOSITION OF THE VENUS SURFACE AS DEDUCED FROM THE ATMOSPHERIC COMPOSITION

Robert F. Mueller

CHAIRMAN:

Our next speaker is also concerned with the planet Venus. His concern is the composition of the Venus surface as deduced from its atmospheric composition. This is Dr. Robert Mueller.

DR. MUELLER:

My thesis is that the atmosphere of Venus, including the major component, carbon dioxide, and many other constituents, results essentially from a strong chemical interaction with the lithosphere, or rocksphere, of the planet. If this is true, there must be a rather close relationship between the molecular composition of the atmosphere and the mineralogic composition of this rocksphere. If, then, we can look at the atmosphere and measure the concentration of various molecules, we can thereby learn something about mineralogic constitution of the surface rocks.

Now, the character of these types of interactions may be illustrated with chemical reactions of the following type. Calcium carbonate, a common constituent of the earth's crust, for example, can react with another common constituent, quartz, to yield calcium silicate and carbon dioxide gas, which is the major constituent of the atmosphere. Also, a minor constituent may result, for example, fluorine produced when the mineral fluorite reacts with quartz and water and yields calcium silicate and hydrogen fluoride.

One could in this manner discuss innumerable other major and minor constituents and relate them to the composition of the lithosphere.

Now, these reactions are shifted to the right by high temperatures; that is, the gas pressures will rise directly as a function of the temperature, so that if one could calculate this function in some way and compare it with the observational data one would have indirect evidence for not only the type of interaction but the various thermal characteristics of the interaction.

If we look at Figure 1, we see an envelope of curves calculated from thermochemical data and corresponding to reactions of the first type plotted in terms of atmospheres of carbon dioxide. We see that the space probe data fall into the range between 10 and 100 atmospheres, and within the uncertainties involved there really isn't anything to choose between the Venera IV and the Mariner V data; but we see at any rate that there is a close correspondence to what we would expect from this type of interaction.

We can go on to the next type of reaction, shown in Figure 2, which involves the minor constituents hydrofluoric acid and hydrochloric acid as determined by Connes, Connes, Benedict, and Kaplan. One of the curves refers to the fluorite reaction mentioned previously, while the other is a corresponding one for hydrochloric acid. We see again there is a fair correspondence to the model.

There is still a minimum amount of this type of quantitative data, but there is quite a bit of a qualitative nature so that upper limits of abundances for such species as hydrocarbon molecules may also be seen to be in agreement with this interaction model. In fact, we would expect this situation to prevail anywhere where there is no control by exhaling such as is discussed by Dr. Rasool.

Figure 3 is essentially my picture of the Venus atmosphere, and the essence of this is the basal interaction zone, in which the lower atmospheric gases react chemically with the upper lithosphere and in which the molecular abundances are established. The overlying zone is one in which these gases are frozen in their equilibrium abundances; it is this zone which is largely observed in the spectra. Finally, above this is the zone of photochemical reactions.

If this model holds, we can expect the Venus atmosphere to have a very contemporary characteristic; that is, the constituents are being formed and destroyed before our eyes. This is quite different from the situation we find on the cooler terrestrial planets, where the atmospheric constituents are thought to date back to remote geological times.

CHAIRMAN:

Is there any question or comment at this point? It is a novel picture of the origin of the Venus atmosphere.

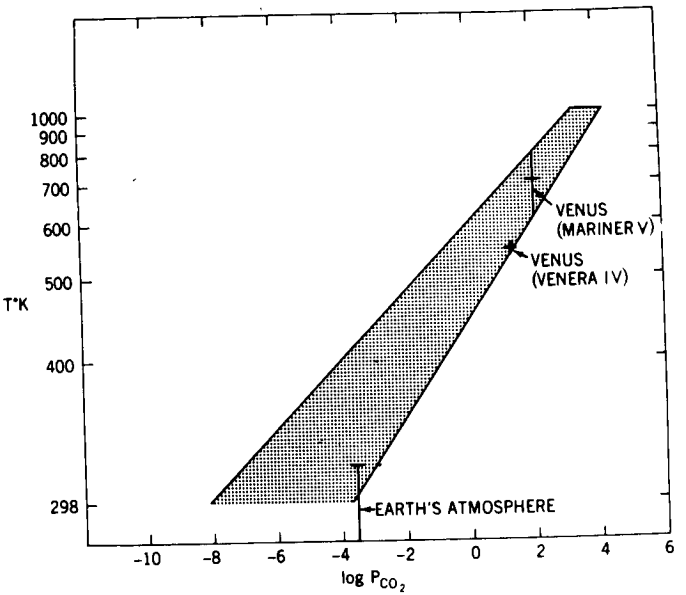

Figure 1

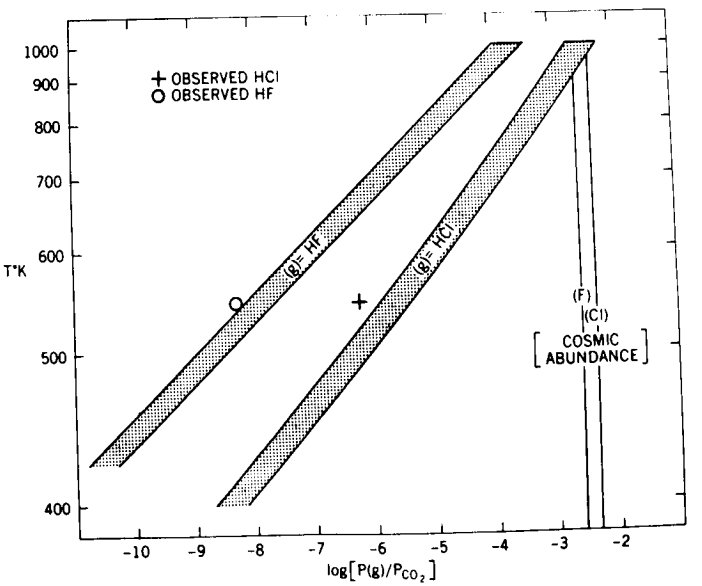

Figure 2

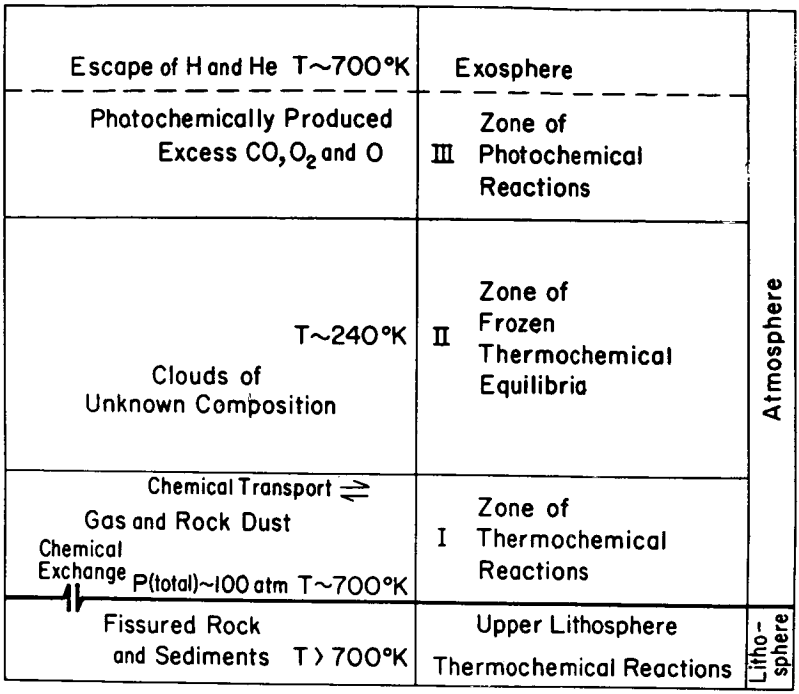
Escape of H and He T~700°K
Exosphere
Photochemically Produced
Excess CO, O_2 and O
III Zone of
Photochemical
Reactions
T~240°K
Clouds of
Unknown Composition
II Zone of
Frozen
Thermochemical
Equilibria
Atmosphere
Chemical Transport
Gas and Rock Dust
Chemical
Exchange
P(total)~100 atm T~700°K
I Zone of
Thermochemical
Reactions
Fissured Rock
and Sediments T > 700°K
Upper Lithosphere
Thermochemical Reactions
Litho-
sphere

Figure 3

EFFECTS OF SCATTERING ON THE THERMAL EMISSION FROM VENUS

Robert E. Samuelson

CHAIRMAN:

Our next speaker is also concerned with the planet Venus. His interest is in the effects of scattering on the thermal emission from Venus. This is Dr. Robert Samuelson.

DR. SAMUELSON:

One of the major things that the two recent probes to Venus (the Venera IV and the Mariner V probes) did not give was any information on the cloud structure of Venus. By patching together certain types of information, clues can be obtained as to what this cloud structure might be. Today I would like to indicate some of the work that I have done which indicates that the cloud tops may be a very diffuse aerosol-like structure. This is opposed to what we find on the earth in the way of water clouds, which are much more compact.

Looking at Figure 1, we can get introduced into the subject by fixing our attention on the schematic at the right. The large solid dot schematically is the solid core of Venus. The two concentric circles outside represent two parts of the atmosphere. There is a differentiation. The inner circle indicates the upper limit of the lower atmosphere, which is in convective equilibrium; i.e., that part of the atmosphere in which the temperature decreases outward. Then we go higher, into the lower stratosphere, where the atmosphere is essentially isothermal. So the inner circle breaks, or shows the break between, this isothermal region and the region in which the temperature increases inward. The outer circle is the outer limit of the optically active atmosphere.

Now, imagine an observer on the earth looking in a direction opposite the arrows—back toward Venus. He would see down to an effective level in the atmosphere which is indicated by the curved line connecting the arrow bases. And this effective radiating level in the atmosphere would be the region which would have a temperature corresponding to the effective brightness temperature of the planet as seen by the observer.

So, as the observer looked toward the center of the disc, he would see as deeply into the atmosphere as he could. As he scanned out toward the edge he would see higher and higher into the atmosphere at cooler and cooler temperatures until he came to the region of the tropopause; after which, as he looked out further, he would see only an isothermal region, and the intensity of radiation would be essentially constant.

Now, in the graph we have the actual quantitative data obtained by James Westphal of Caltech with the 200-inch telescope at Mount Palomar. Plotted here is the intensity of thermal radiation versus the direction cosine μ of the viewing angle, which is a monotonic function of position on the disc from the center out to the limb.

Now, again, we have first of all a very rapid drop of intensity from $\mu = 1$ to $\mu = .5$, which corresponds in the schematic to scanning outward along the effective radiation level curve up to the point of the tropopause. Then a break occurs and the slope of the graph is less steep for $\mu < .5$, indicating we are in the more isothermal region of the lower stratosphere.

Now, you can take these data, invert them through an equation of radiative transfer that considers both scattering and thermal emission, and come up with a temperature profile. The results are shown in Figure 2.

I want to attach your attention first to the dashed curve. This is the temperature profile inferred by inverting the equation of transfer, using the data shown in Figure 1.

In addition to this we have the Mariner V data from the S-band radio occultation experiment, which also give a temperature profile in the atmosphere. This is shown by the solid curve.

The distinction is that the 8- to 14-micron limb darkening gives the temperature shown along the abscissa as a function of optical depth whereas the Mariner V data give the temperature as a function of radius, or distance from the center of the planet.

So what we have by matching up the two profiles—by normalizing them to each other—is the optical depth as a function of the distance, or of the geometrical height.

What is done is, the two curves are matched at the tropopause and then the slopes of these curves are made equal by expanding or contracting the scale.

Now, when this is done and the optical depth is obtained as a function of radius, we get extinction coefficients for Venus of on the order of 10^{-6} cm^{-1}. And to contrast this with other types of atmospheres, a pure CO_2 atmosphere, if that were the case for Venus in this general region, would have an opacity which is about five times less.

On the other hand, if we were seeing down into a water cloud such as we would have on the earth, the opacity would be 100 times greater. As a result, the opacity of Venus in this general region appears to be somewhat between that for a pure CO_2 atmosphere and that for a typical water-type cloud. In other words, we appear to have something which corresponds to a very tenuous aerosol or haze in the region around the tropopause, which implies a non-volatile material as opposed to a volatile material. In other words, water presumably would not be this type of cloudy substance. So I suppose in summing up we could say that what we have is a tenuous aerosol which optically is very comparable to what you would have over Los Angeles on a clear day.

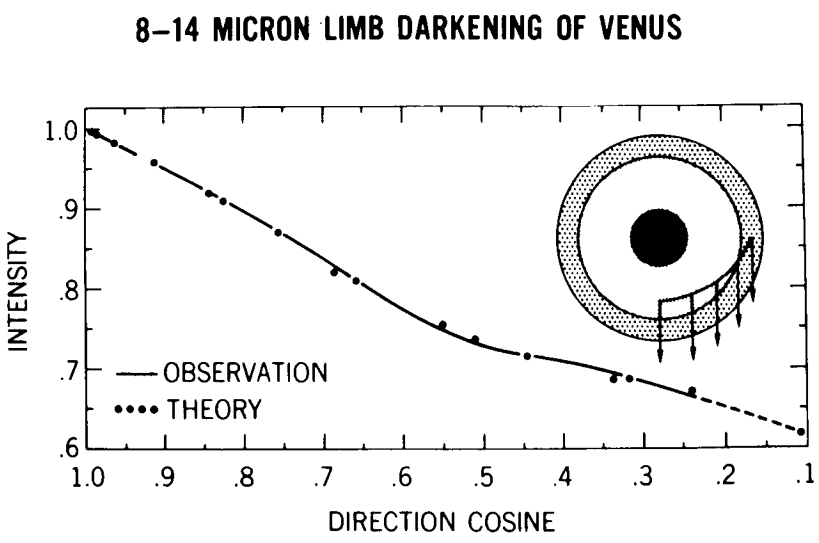

Figure 1

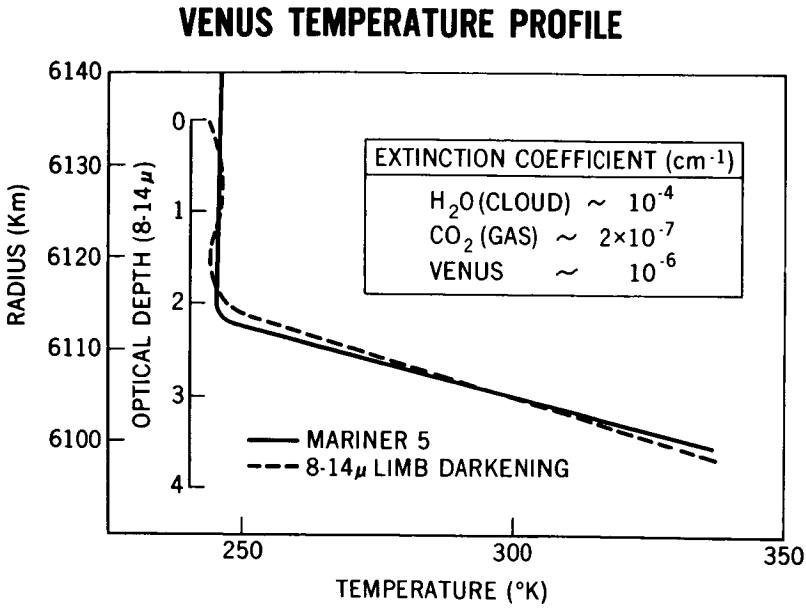
VENUS TEMPERATURE PROFILE
RADIUS (Km)
6140
6130
6120
6110
6100
OPTICAL DEPTH (8-14μ)
0
1
2
3
4
EXTINCTION COEFFICIENT (cm-1)
H2O (CLOUD) ~ 10-4
CO2 (GAS) ~ 2×10-7
VENUS ~ 10-6
MARINER 5
8-14μ LIMB DARKENING
250
300
350
TEMPERATURE (°K)

Figure 2

CHEMICAL PROCESSES IN COMETS

William M. Jackson

CHAIRMAN:

Our next speaker is Dr. William Jackson, who will discuss chemical processes in comets.

DR. JACKSON:

An understanding of how comets interact with the interplanetary radiation field will enable astronomers and astrophysicists to use ground-based observations of comets to map this field in regions that are not accessible to space probes.

Visible emission from comets is caused by the resonance fluorescence of radicals and ions present in the head and tails of comets. Since it is known that these radicals and ions cannot be stabilized in the icy nucleus of the comet, they must be formed either photochemically or as result of the effects of the solar wind protons and electrons on this neutral gas.

The observations of the radical and ion emissions in comets indicate that these species are present very close to the nucleus. The velocity of the neutral gas evaporating from the icy nucleus is about a half kilometer per second. Therefore, the observations of these radicals near the nucleus correspond to exposure times of this neutral gas of only 10^3 to 10^4 seconds. The average lifetime, however, for a neutral molecule before photodissociation, photoionization, or interaction with the solar wind is 100 times larger than this; that is, 10^5 to 10^7 seconds. This has led some astronomers to conclude that these mechanisms cannot be invoked to form ions and radicals near the nucleus.

This conclusion is not valid, since the number of radicals and ions in the nucleus is a function not only of the lifetime of the prime molecules, but also of the density of these prime molecules. This density for the Whipple model of the comet can be shown to vary inversely as the square of the distance from the icy nucleus, and therefore could compensate for the long life time of the parent molecules.

With these ideas in mind, we constructed a theoretical model for the production of radicals and ions by a photodissociation and photoionization mechanism. In this model we have taken into account the effect of the optical depth of the neutral molecules and the calculated densities of radicals and ions.

In Figure 1 we have plotted in polar coordinates the number density of the ions and the radicals as a function of the distance from the center of the comet. Here we see that the maximum density of ions for a small comet at 1 A.U. occurs near the nucleus. The same is true for the radicals. Furthermore, we also see that one only has to invoke a mole fraction of the C_2 parent molecule of 10^{-4}. That is, the number of C_2 parent molecules evaporating from the nucleus represents one part in 10^4 of the total number of molecules evaporating from the nucleus.

Figure 2 shows what happens when we increase the optical depth by increasing the size of the comet or bringing it closer to the sun, or by increasing the evaporation rate. Here we see that the maximum density has shifted from the nucleus out to 1,000 kilometers in front of the nucleus. The same is true for the CO+ ions.

Now, this means that if we assume, as is normally done, that the nucleus is at the center of the most intense emission, errors as large as 10^4 kilometers can be made in measuring the position of the nucleus. Models of cometary phenomena, therefore, should not be forced to account for ionization and dissociation any closer than 10^4 kilometers, since errors in the measurement of the nucleus position can be off by this much.

In conclusion, I would like to say that a detailed theoretical study has been useful in showing that ions and radicals can be produced near the nucleus even though the lifetime of an average molecule is long. Further, the position of the apparent nucleus has been found to be dependent on the optical depth of the neutral molecules and therefore also upon the nuclear size and heliocentric distance.

RADICAL AND ION DENSITIES FOR A 0.5 km COMET AT 1 A.U.

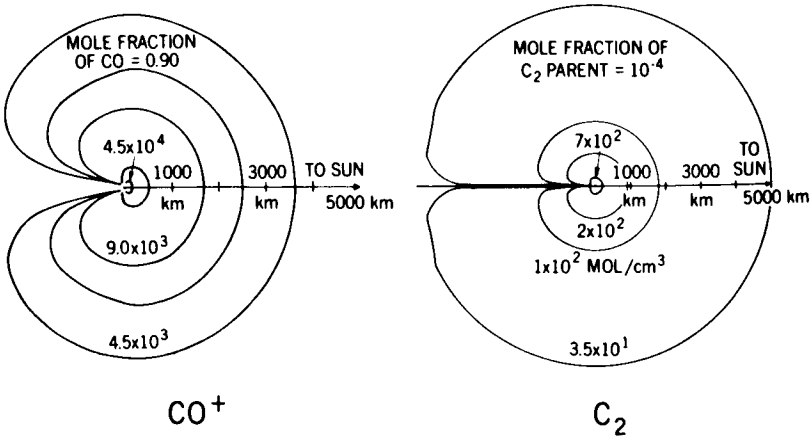

Figure 1

RADICAL AND ION DENSITIES FOR A 5 km COMET AT 1 A.U.

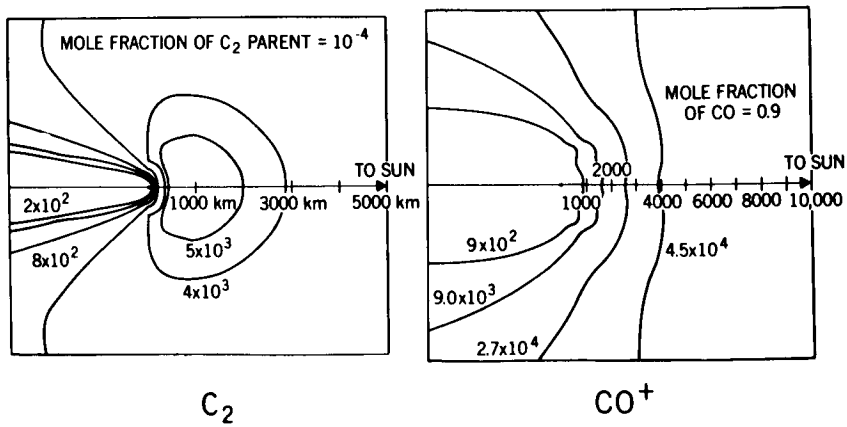

Figure 2

GEODESY WITH RESONANT SATELLITES

Carl A. Wagner

CHAIRMAN:

We turn now to the subjects of geodesy and celestial mechanics, and our first speaker in this area is Dr. Carl Wagner, who will speak about geodesy with resonant satellites.

DR. WAGNER:

As we all know, one of the great achievements of the space age has been to prove that the earth's mass distribution is much more complicated than was once thought possible.

Perhaps the greatest consequence of this discovery bears directly on the accurate navigation of orbiting satellites. Here the potentially promising use of the most sophisticated tracking devices such as lasers for long-term orbit prediction is severely limited by the complicated earth, which disturbs the satellite in still unpredictable ways.

In satellite geodesy we invert this problem, and from the deviations of a satellite's orbit we try to calculate a better earth model.

The starting point in these calculations is a general disturbing function which for the earth can account for any arbitrary mass distribution that can affect the dynamics of a satellite.

This arbitrary function or potential is conveniently expressed mathematically as a spherical harmonic series in so-called associated Legendre polynomials (Figure 1).

The arbitrary constants C and S of this series may represent the external gravity potential of any mass distribution in the same way that the constants of one-dimensional Fourier series can represent an arbitrary one-dimensional function.

These spherical harmonics are functions of three variables: radius r from the center of coordinates, latitude ϕ, and longitude λ. They can be

divided into two kinds according to whether or not they depend on the longitude. Earth forces which are derived from them cause essentially different deviations of satellite orbits.

The harmonics that do not depend on the longitude, the zonals, where the ℓ subscript is zero, give rise to long-term changes in the orbit plane and orientation and in the shape of the orbit in its plane.

These long-term changes are easily observed compared to the small effects which occur periodically in each satellite revolution and also in one revolution of the earth.

These small short-term effects are generally all that are observed from the far more numerous longitude-dependent harmonics, those with subscripts m not equal to zero.

However, there is one kind of orbit which allows long-term effects from the longitude harmonics to develop for essentially the same reason as for the zonals. The common orbit feature implying long-term effects for both kinds of harmonics is a satellite track that is geographically stationary with respect to the given harmonic.

With respect to the zonals, all orbits are stationary in this sense. But, with respect to the longitude harmonics, the only stationary orbits are those whose orbital frequency is commensurate with the earth's rotation. These are the so-called resonant orbits. They offer the possibility of observing the greatly amplified long-term effects of these generally hard-to-observe components of the earth's potential function.

The greatest deviations on these orbits from the longitude harmonics occur along the track of the satellite and involve long-term changes in the energy or the semimajor axis of the satellite.

A recent examination of the elements of almost 1,000 satellites presently being tracked reveals the existence of about 100 which should be showing considerable along-track deviations due to resonance with longitude harmonics of order m equal to multiples of the orbital frequency S.

The distribution by inclination and frequency of these orbits is shown in Figure 2.

When more of these objects are tracked for the purposes of satellite geodesy, I would expect we should begin to have the first really definitive

information on many of the longitude harmonics of low order and also order 12 through 15.

Over the past two years I have been developing theories and computer programs to deal efficiently with data from these resonant orbits for the purpose of recovering potential model coefficients. One of these orbits that I have been investigating is that of the Russian communications satellite, Cosmos 41, whose energy or semimajor axis variation with a period of about 120 days is shown in Figure 3. This orbit, whose frequency is two times a day, shows the resonance effects of harmonics of order 2, 4, and even 6 as revealed by gravity solutions I have made from these data. The solutions are in good agreement with recent results from non-resonant orbits.

From all the tracking data I have now on resonant satellites of one and two revolutions a day, there are excellent possibilities of obtaining significant information on more than half of all the longitude harmonics through 88. About a quarter of them should be definitively determined from a combined solution using 24 arcs of the 10 satellites shown in Figure 4.

Already the ellipticity of the earth's equator has been measured most accurately from only about half of this data. But the broadest achievements of resonant-satellite geodesy are still in the future.

THE EARTH'S GRAVITATIONAL POTENTIAL IN SPHERICAL HARMONICS

$$V_e = \sum_{\ell=0}^{\infty} \sum_{m=0}^{\ell} \frac{\mu r_e^{\ell}}{r^{\ell+1}} P_{\ell m}(\sin \varphi) \left[C_{\ell m} \cos m\lambda + S_{\ell m} \sin m\lambda \right]$$

EXAMPLES OF TERMS

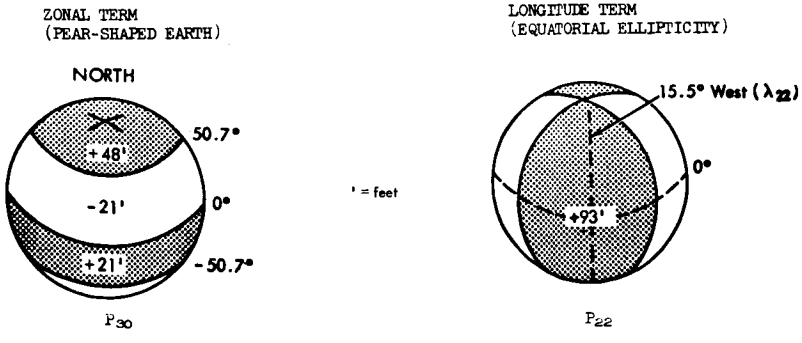

Figure 1

CHARACTERISTICS OF 97 EXISTING RESONANT ORBITS WITH BEAT PERIODS GREATER THAN 10 DAYS

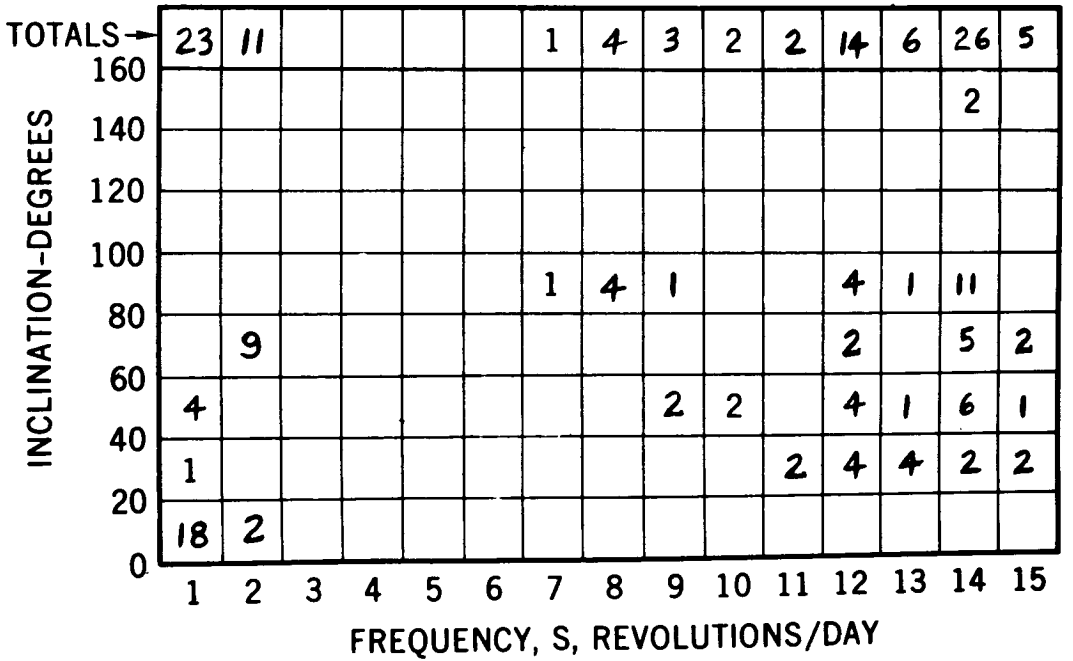

Figure 2

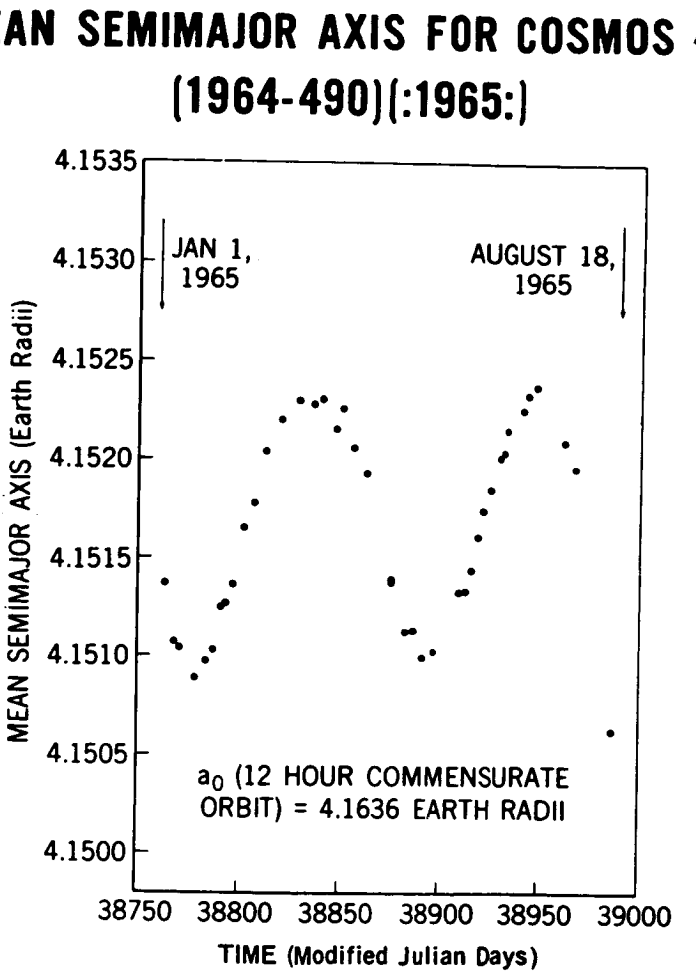
MEAN SEMIMAJOR AXIS FOR COSMOS 41
(1964-490)(:1965:)
4.1535
4.1530
4.1525
4.1520
4.1515
4.1510
4.1505
4.1500
MEAN SEMIMAJOR AXIS (Earth Radii)
JAN 1, 1965
AUGUST 18, 1965
a0 (12 HOUR COMMENSURATE ORBIT) = 4.1636 EARTH RADII
38750
38800
38850
38900
38950
39000
TIME (Modified Julian Days)

Figure 3

RESONANT SATELLITES AND HARMONICS IN CURRENT LOW ORDER GRAVITY SOLUTIONS

Satellite	Orbit Frequency (revs/day)	Inclination (degrees)	Number of arcs being used
Syncom 2	1	29 - 33	6
Syncom 3	1	0 - 3	4
Early Bird	1	0 - 3	2
Intelsat II-F4	1	1	1
Intelsat II-F1	2	17	1
Cosmos 41	2	65 - 66	2
Cosmos 41 rocket	2	67 - 69	2
Molniya 1	2	64 - 65	4
Molniya 4	2	65	1
Molniya 7	2	65	1

Quality of Determination of $H_{\ell m}$ With Combined Solution (S-Strong, W-Weak)

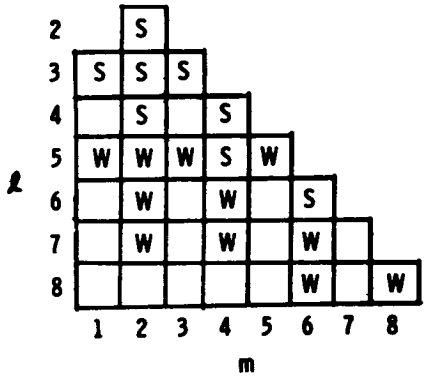

Figure 4

DYNAMICALLY SELF-CONSISTENT PLANETARY EPHEMERIDES

Lloyd H. Carpenter

CHAIRMAN:

Our next speaker is concerned about variations in the positions of planets. His subject is dynamically self-consistent planetary ephemerides. Mr. Lloyd Carpenter.

MR. CARPENTER:

For the space program it is necessary to have very accurate coordinates of the sun, moon, and planets. Obtaining these coordinates involves several problems, and the solutions to these problems are not independent. The basic mathematical model was established by Newton, and the astronomical constants are determined by fitting the observed motions in the solar system to this model.

The most immediate problem is the accurate determination of the masses of the planets, and their orbits. In Figure 1 we have the orbits of the five outer planets starting with Jupiter, and working outwards. Saturn, Uranus, Neptune, and Pluto. (The sun is at the center.) To the right is the direction of the vernal equinox. For each orbit the position π of the perihelion, or closest approach to the sun, is given as well as the position Ω of the ascending node, or the point where the orbit intersects the plane of the ecliptic. These orbits are all projected onto the plane of the ecliptic. The distances are given in astronomical units (one unit, of course, being equal to the mean distance between the earth and the sun).

Just this year a redetermination of the mass of Pluto was made at the Naval Observatory, yielding a value which is just one-fifth of the previously adopted mass. Thus it becomes necessary to compute a new set of coordinates for the planets based on the new value for the mass of Pluto. Of more direct concern for the space problems is the matter of fitting the motions of the inner planets to the recent highly accurate radar observations.

The point of this discussion is to indicate that for the purposes of the space program it is not reasonable to expect to compute an accurate ephemeris which will be used over a period of many years. Rather, what

we should hope for is to set up a highly accurate and efficient method for computing planetary theories such that this method can be readily applied when new values are determined for the astronomical constants.

For this purpose there are methods which offer important advantages over the numerical integration techniques which are presently being used. Dr. Musen has given a method - general perturbations in rectangular coordinates—which lends itself to the process of iteration or successive approximations. I have developed a program which applies this process with the perturbations represented in Chebyshev series. This process is extremely fast and accurate. The differential corrections which are so necessary for updating are very easy to apply. The corrections due to general relativity are added as small corrections to the coefficients in the series. The form of the solution is concise and convenient for the computations.

As an example, I have applied this method to the motions of the five outer planets between the years 1800 and 2000. The positions of these planets during this time interval are given to the full accuracy of the observations in only six pages of numerical coefficients. In other words, the results are given in less than 4 percent of the space required to tabulate the coordinates at 40-day intervals as the results of numerical integration. This process is presently being further studied and applied at the Jet Propulsion Laboratory.

In Figure 2 I have given, just to indicate the form of the solution, the coefficients in the perturbations of Jupiter and Saturn for a 10-year interval, from 1970 to 1980. The perturbations are divided into components α, β, and γ in the directions of the radius vector, the velocity vector, and the normal to the orbit plane. The numbers which are given here are coefficients of Chebyshev polynomials of various degree indicated by the index K.

The point of this is just to indicate how concisely the solution is represented when given in this form. These numbers are sufficient to give the positions with a formal accuracy of 10 significant figures.

In Figure 3 you see the corresponding solutions for the other three outer planets, Uranus, Neptune, and Pluto. Here again the series are very rapidly converging.

We are presently applying the method of successive approximations with the perturbations represented in trigonometric series. Some early

difficulties have now been overcome, and this method promises to be the most useful of all that are available for studies of the motions of the inner planets.

These techniques have also been applied to the studies of periodic orbits both in the restricted three-body problem and in the earth-moon-sun four-body problem. In fact, the first periodic orbits in this last problem were found by our group using the method of Chebyshev series.

In conclusion, the studies now being made in planetary theory are very necessary and useful for the space program.

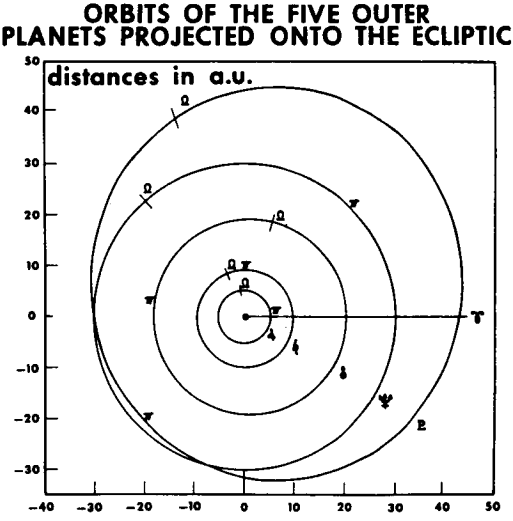

Figure 1

COEFFICIENTS IN THE PERTURBATIONS OF JUPITER AND SATURN FROM 1970 TO 1980

JUPITER				SATURN			
K	$\alpha \cdot 10^{10}$	$\beta \cdot 10^{10}$	$\gamma \cdot 10^{10}$	K	$\alpha \cdot 10^{10}$	$\beta \cdot 10^{10}$	$\gamma \cdot 10^{10}$
0	-3256757	5360123	5198	0	6939517	-15647683	-355940
1	2500078	1425165	79032	1	9197540	2489044	129124
2	-2366685	-6571803	-13979	2	2924647	838461	-23869
3	-2341314	3160242	-44592	3	-611122	-1061923	-35322
4	848352	2024059	7230	4	-366689	-394481	19369
5	467504	-466370	7727	5	-57395	28609	3021
6	-53695	-230522	-21	6	-6053	40923	-2981
7	-41346	19341	-531	7	-7295	7898	-691
8	5145	13606	46	8	-858	-291	162
9	4465	-2464	68	9	1208	292	49
10	-850	-1579	-8	10	420	421	-19
11	-768	174	-12	11	25	72	-3
12	7	187	-1	12	28	-44	5
13	73	5	1	13	28	-21	2
14	-7	-9	0	14	5	-3	-0
15	-11	5	0	15	-3	-2	-0
16	1	3	0	16	-1	-2	-0
17	1	0	-0				
19	-1	0	0				

Figure 2

COEFFICIENTS IN THE PERTURBATIONS OF URANUS, NEPTUNE, AND PLUTO FROM 1970 TO 1980

URANUS

K	$\alpha \cdot 10^{10}$	$\beta \cdot 10^{10}$	$\gamma \cdot 10^{10}$
0	7299007	-2434514	-27449
1	-179712	-2851662	16595
2	2012702	-599713	31416
3	339713	838943	5897
4	-310063	131556	-5477
5	-36915	-84814	-1110
6	26960	-14216	552
7	4404	8119	123
8	-2953	1658	-54
9	-613	-905	-15
10	364	-223	6
11	81	109	2
12	-44	31	-1
13	-12	-14	-0
14	6	-4	-0
15	2	2	0
16	-1	1	-0

NEPTUNE

K	$\alpha \cdot 10^{10}$	$\beta \cdot 10^{10}$	$\gamma \cdot 10^{10}$
0	2669824	-1262528	17413
1	-937276	-1483766	39623
2	702239	-1187449	-6794
3	622771	361012	-14389
4	-120838	237886	983
5	-74935	-36909	1812
6	10421	-23840	-72
7	7443	3102	-177
8	-933	2618	4
9	-885	-312	20
10	93	-323	-0
11	114	33	-3
12	-10	41	-0
13	-15	-3	0
14	1	-6	0
15	2	0	-0
16	-0	1	-0

PLUTO

K	$\alpha \cdot 10^{10}$	$\beta \cdot 10^{10}$	$\gamma \cdot 10^{10}$
0	3747768	-1071643	-40202
1	574900	-861509	-109320
2	1286712	83623	-311596
3	74821	438008	-30319
4	-254537	-556	67037
5	-14669	-50819	5540
6	24397	-674	-6835
7	1917	4933	-678
8	-2555	188	696
9	-274	-568	91
10	306	-35	-81
11	40	70	-13
12	-38	6	10
13	-6	-9	2
14	5	-1	-1
15	1	1	-0
16	-1	0	0

Figure 3

THE REDISCOVERY OF JUPITER X

Peter Musen

CHAIRMAN:

There are few astronomers who have the opportunity to discover a planet or a planetary satellite. One of our scientists who is an expert in celestial mechanics has rediscovered a planetary satellite. Dr. Peter Musen will tell you about the rediscovery of Jupiter X.

DR. MUSEN:

We are interested in the application of electronic machines to the expansion of the general perturbations of the natural satellites of outer planets. Such methods, as it was indicated also by the previous speaker, can successfully compete with the methods of numerical integrations.

However, in my opinion, the general perturbations give better information about the physics of the problem: they show the relative importance of different waves in the expansion of perturbations, as well as being able to supply us with information about the behavior of an orbit and its stability over a long interval of time.

As a test body we choose the X^{th} satellite of Jupiter because it is faint; because its orbit has a large eccentricity, about .2; because there is a large inclination of its orbital plane toward the orbital plane of Jupiter, about 28 degrees; and because the solar effects are quite considerable in this case. The last published observation we found in the literature was one made in 1958. From 1958 to '67 either this satellite was not observed or observations were not published.

In the case of such a large inclination, if one would attempt to develop a purely analytical theory of motion, he would be obliged to push the existing development by Delaunay several orders of magnitude higher, because of the large eccentricity and large inclination. Nobody has solved this problem yet, and probably several years will pass before we do have a complete solution.

It means we have to apply some other theory.

We choose a theory by Hansen, with necessary modifications to adapt the theory to existing electronic machines. The Hansen theory represents a peculiar space-time transformation when the disturbed motion of a real satellite is being transformed into undisturbed motion of a fictitious satellite moving in an ellipse of constant shape.

The position of the real satellite is determined by its deviation from the position of the auxiliary, fictitious satellite in time and space.

The basic information is the mean elements of the satellite and of Jupiter. The machine expands the disturbing potential, forms the differential equations for Hansen perturbed coordinates, and integrates them by means of the process of iteration. We need about 10 iterations to develop the theory of a satellite of Jupiter, about 14 to develop the theory of the moon. We used the moon as a test body—not in order to develop a new theory of the moon, but if the theory works for the moon, surely it will work for certain outer satellites of Jupiter, too.

Final results are the expansion of each Hansen coordinate into a trigonometric series with four basic arguments. The machine, in addition, computes the speed of rotation of the node and of the perigee. After we completed the program and the theoretical investigations, we dared to predict what the position of Jupiter X would be in '67.

Figure 1 gives us a basic idea about the position of the satellite relative to Jupiter. Jupiter is in the center; on the horizontal axis are given the differences in the right ascension of the satellite and of Jupiter, and on the vertical axis are given the differences in declination for every few days.

The accuracy of computation of such an ephmeris is within one minute of arc. The satellite was observed again after an interval of nine years by Dr. Roemer in 1967. After we obtained Dr. Roemer's additional observations of the satellite, we computed better expansions of perturbations, and produced a better orbit using Lemekhova's orbit as a start; her orbit represented observations up to 1942 with an accuracy of approximately 37 seconds of arc.

In Table 1 we show the final result. The final accuracy of the representation with the expansion of Hansen's perturbations is just a few seconds of arc.

The satellite was re-observed also in 1968. We have two additional observations in 1968 which we didn't use. As we see, the machine can be used successfully to develop semi-analytical theories of motion of natural satellites of Jupiter and perhaps satellites of some other planets.

THE REPRESENTATION OF OBSERVATIONS USED

	UT		OBSERVED α(1950.0)	OBSERVED δ(1950.0)	O − C Δα COS δ	O − C Δδ	
1	1938 July	6.3743	22h17m15s.21	−11°13′35″.3	−1.3	+2.5	Mt. Wilson
2		6.4667	22 17 13.89	−11 13 41.6	−0.9	+1.5	Mt. Wilson
3		9.4229	22 16 22.89	−11 16 23.4	−1.5	+1.4	Mt. Wilson
4		9.4521	22 16 22.36	−11 16 26.0	−0.9	+1.8	Mt. Wilson
5		27.3361	22 09 13.67	−12 00 14.9	−0.2	+0.0	Mt. Wilson
7		28.3174	22 08 45.05	−12 03 06.3	−0.3	+0.3	Mt. Wilson
8		29.4667	22 08 10.91	−12 06 30.2	+0.1	+1.1	Mt. Wilson
10	Aug.	24.4167	21 54 07.40	−13 33 16.2	+2.4	+0.2	Mt. Wilson
11		25.2129	21 53 41.86	−13 36 00.3	+3.2	−0.8	Mt. Wilson
12	Oct.	18.1285	21 39 13.15	−15 25 53.6	+0.7	+0.1	Mt. Wilson
13		20.1257	21 39 25.45	−15 25 54.0	+0.7	−0.5	Mt. Wilson
14		23.1319	21 39 50.17	−15 25 15.1	+0.2	−0.6	Mt. Wilson
15	Nov.	21.1188	21 49 30.06	−14 41 12.0	+1.0	+0.2	Mt. Wilson
16	1939 July	15.4205	0 31 26.11	+ 1 36 35.3	+3.0	−0.6	Mt. Wilson
17		15.4528	0 31 26.49	+ 1 36 36.4	+2.2	−0.7	Mt. Wilson
18	Aug.	16.4365	0 33 47.03	+ 1 33 14.1	+1.3	+2.6	Mt. Wilson
19		16.4806	0 33 46.72	+ 1 33 11.8	+1.0	+2.4	Mt. Wilson
20	Oct.	8.3998	0 15 53.39	+ 0 00 48.7	−0.3	+3.3	Mt. Wilson
21	Dec.	15.0885	0 01 26.93	− 0 46 17.8	−2.6	−0.6	Mt. Wilson
24	1940 Sept.	6.3736	2 57 26.16	+16 02 05.9	−0.2	−0.1	Mt. Wilson
25		8.4438	2 57 25.74	+16 02 03.0	+0.1	−0.6	Mt. Wilson
26	Oct.	25.3488	2 38 37.74	+14 14 20.0	+0.9	−0.7	Mt. Wilson
27		25.3731	2 38 36.88	+14 14 15.2	+1.6	−0.3	Mt. Wilson
28	Nov.	1.2160	2 34 23.96	+13 48 17.5	+0.0	−1.0	Mt. Wilson
29		1.4161	2 34 16.35	+13 48 33.3	+0.1	−0.6	Mt. Wilson
30	1941 Dec.	23.2569	4 56 06.78	+22 24 12.2	−1.0	+0.2	Mt. Wilson
31	1942 Feb.	17.2342	4 44 28.41	+22 23 09.5	+0.7	−1.1	Mt. Wilson
32		18.2618	4 44 36.92	+22 23 19.4	+2.0	−1.5	Mt. Wilson
33	Nov.	8.4951	7 53 12.49	+21 30 26.6	−0.1	−0.4	Mt. Wilson
34		9.5090	7 53 17.86	+21 30 13.4	+0.2	−0.6	Mt. Wilson
35	1943 Jan.	6.3400	7 32 51.54	+21 57 36.7	+6.1	+1.1	Mt. Wilson
36		6.3230	7 32 48.03	+21 57 40.5	+5.6	+0.5	Mt. Wilson
37	1951 Sept.	30.29101	0 39 41.51	+ 2 17 48.3	−1.1	−3.6	Mt. Wilson
38		30.30663	0 39 41.08	+ 2 17 47.1	−1.6	−3.3	Mt. Wilson
50	1958 Apr.	25.30100	13 34 27.90	− 7 41 04.4	−2.2	−2.0	Flagstaff
51		25.36887	13 34 26.09	− 7 40 53.6	−1.3	−2.3	Flagstaff
52	1967 Jan.	7.31247	8 17 49.38	+20 23 30.2	−0.1	+4.2	Tucson
53		7.38122	8 17 47.19	+20 23 34.4	+1.4	+3.3	Tucson
54	Feb.	11.17166	7 57 31.87	+21 06 02.6	−6.3	+2.7	Tucson
55		11.35846	7 57 28.83	+21 06 06.1	−7.3	+2.9	Tucson

Table 1

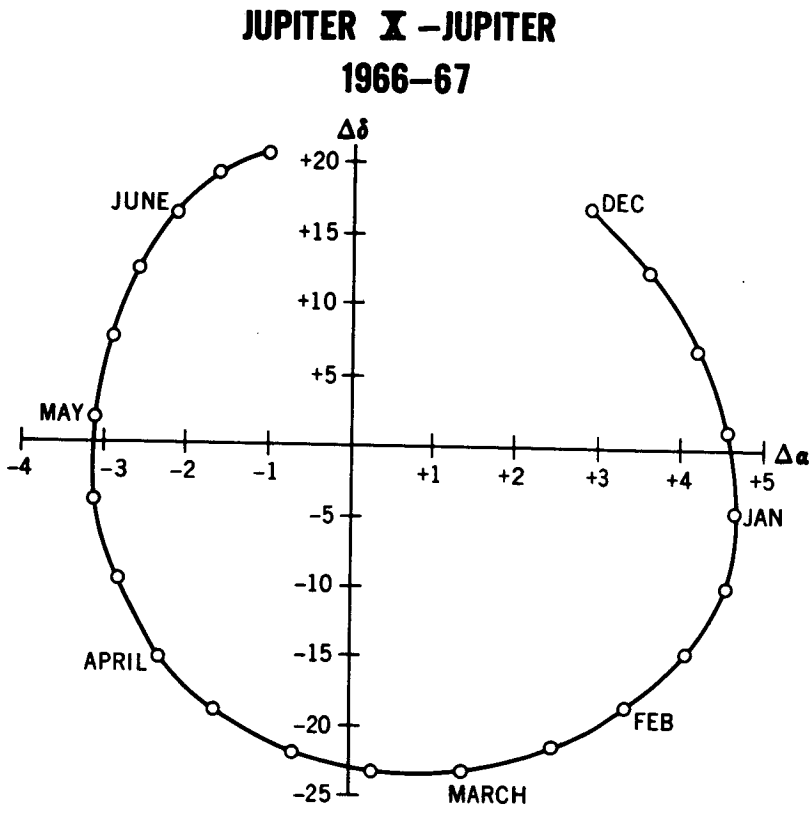
JUPITER X – JUPITER
1966–67
Δδ
+20
+15
+10
+5
-5
-10
-15
-20
-25
JUNE
DEC
MAY
JAN
APRIL
FEB
MARCH
-4
-3
-2
-1
+1
+2
+3
+4
+5
Δα

Figure 1

SOLAR X-RAY IMAGING

James H. Underwood

CHAIRMAN:

We will turn now to the sun and begin a series of papers concerned with the sun. Dr. James Underwood will speak about solar X-ray imaging.

DR. UNDERWOOD:

The solar corona is quite difficult to observe from the ground. The best observations in visible light can be obtained during eclipses, but they of course are very infrequent. Some observations outside of eclipses can be made with specialized instruments such as the coronagraph invented by Lyot, or with the K-coronameter, which is in use at the High Altitude observatory. Unfortunately, these observations are very difficult to make, because of the masking effect of skylight, which is light scattered from the very bright photosphere. The photosphere is about a million times brighter than the corona. This intense photospheric light makes it almost impossible to observe the corona in front of the solar disc in visible light—such an observation has not yet been made.

Radio observations do enable one to get some idea of the form of the corona in front of the disc, but the resolution obtainable with the radio heliographs in existence at the present time is not very great—of the order of a couple of minutes of arc. A resolution of the order of a few seconds is needed in order to study the morphology of regions of interest in the solar corona.

If, however, you observe the sun at very much shorter wavelengths, ultraviolet and X-rays, then the corona stands out in strong contrast because these radiations are produced in the lower corona and upper chromosphere and one is able to make a study of the morphology of coronal regions in this way.

We have been engaged in such a program, observing the sun in its X-ray emissions with an instrument we fly in rockets, the glancing incidence X-ray telescope. Figure 1 shows some of the results we have obtained in the period between the last solar minimum, which occurred at the end of 1964, and the present time.

One can see from this series of pictures that the variation of solar activity during the solar cycle is reflected in the X-ray region, in the number and intensity of the regions observed. We have been able to observe some rather unusual features in the solar corona. For instance, please note the peculiar S-shaped feature at about 30°N on the central meridian which we observed on October 3, 1967. This represents the X-ray emission from a point where a filament had recently disappeared. This phenomenon is called "disparition brusque," and we see that such an event may give rise to an enhancement of X-rays in the region where it occurs.

We also see jets and arches which emit X-rays extending far up into the corona, 150,000 kilometers or so.

Please note also the brightening of the X-rays which occurs at the limb of the sun. This is evident on all these photographs. And this is due to the fact that the corona is optically thin and one is looking through a greater thickness of material at the limb of the sun than when one looks straight down on the disc. As the X-ray emission in the corona is collisionally excited, the intensity of this emission at the limb is proportional to the square of the electron density integrated along the line of sight.

So, by examining the variation of this X-ray emission with radius and with position angle, we are able to test some models of the electron density variation in the solar corona and perhaps derive new models.

Figure 2 shows the X-ray brightness that would be predicted from one well-known model of the latitude variation of the electron density of the solar corona at solar minimum. This is the model of Waldmeier, which predicts that the electron density should vary smoothly as the cube of the consine of the latitude. We find that in fact the variation is considerably different: there is a sharp cutoff at a latitude of about 65°. This corresponds more to a model in which the electron density, instead of varying smoothly with latitude, undergoes a sudden change at around 65° latitude. Below 65° the electron density is aboout 10^9/cc, but above this latitude it is at least 10 times smaller. The actual latitude and sharpness of the transition changed with the solar cycle, as may be seen from Figure 1. During the period from minimum to maximum, the excess electron density at the equator seems to creep down toward the poles until finally, at solar maximum,there is a complete ring of limb brightening surrounding the sun.

This is just one of the ways in which I think X-ray and extreme ultraviolet observations can supplement the observations made in visible light.

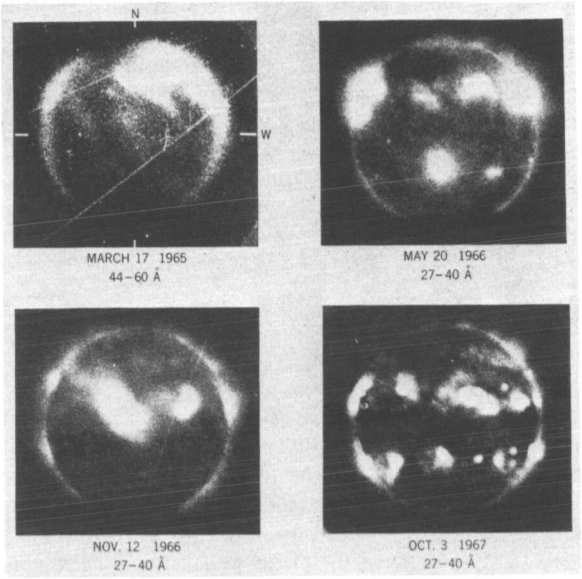

Figure 1

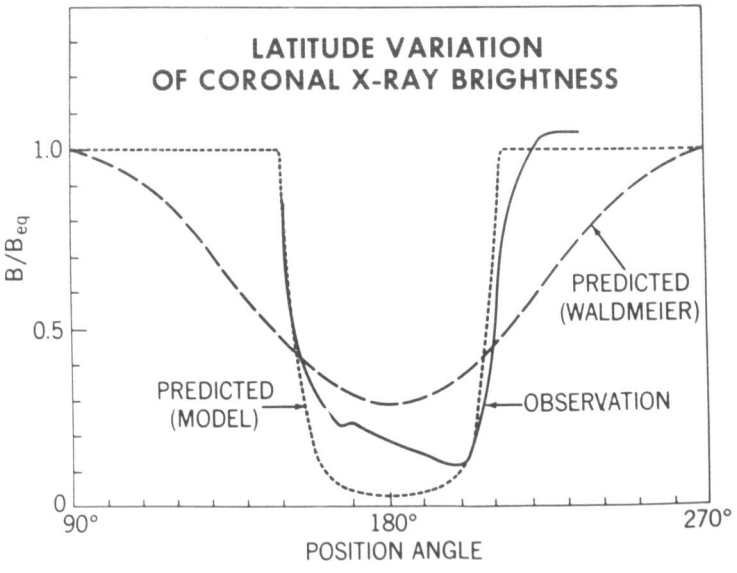

Figure 2

SOLAR X-RAY SPECTRA

Werner M. Neupert

CHAIRMAN:

A companion work to Dr. Underwood's is Dr. Werner Neupert's work in solar X-ray spectra. That's our next subject. Dr. Neupert.

DR. NEUPERT:

One of the goals of solar physics is an understanding of the solar flare phenomena in which a large amount of energy is released or deposited—we don't know which at the present time—in the solar chromosphere and in the lower solar corona. The release of this energy accelerates particles to high energy and also results in the creation of a hot X-ray-emitting plasma. I want to give you some of the results we have obtained recently on the nature of this plasma from our studies of the soft X-ray spectrum.

Using crystal and grating spectrometers pointed at the sun by the OSO III satellite, we have found that the X-ray flare is characterized by a strong emission line spectrum at short wavelengths, that is, in the soft X-ray band of wavelengths.

In Figure 1, where count rate is plotted against wavelength, we observe prior to the flare the characteristic emission line spectrum, with its strong emission lines of Fe XVII, which is associated with the active regions Dr. Underwood showed you in his photographs. During the flare, however, we recorded new emission lines. These new lines are still attributed to iron, but they originate from ions of iron more highly stripped than those that existed prior to the flare. In addition to Fe XVII we now observe Fe XX through Fe XXV. Such highly stripped iron can exist only if one has temperatures of the order of 20 to 40 million degrees. New emission lines from flares also appear at longer wavelengths (between 100 Å and 400 Å) which we observed simultaneously with a grazing incidence grating spectrometer.

As an example of such lines we show in Figure 2 a small region of the spectrum centered at about 256 Å. Here again we plot counting rate against wavelength for a small portion of the spectrum. Each profile is the

average of three scans made, at or near the time shown, through this part of the spectrum. The profiles have been staggered for the sake of clarity in reproduction – as necessitated by their close similarity. Notice the strong line at 255 Å. We have observed this line, which we attribute to Fe XXIV only, during a few strong flares.

In this case, we have the opportunity to measure the wavelength of such a line against its neighbor, a well-known chromospheric emission of He II. One of the most intriguing results to come from the observations to date is the observation that this emission line of Fe XXIV appears on occasion to have been shifted towards shorter wavelengths relative to the He II line. Notice, for instance, the shift of about 0.3 Å during the flare on October 29, 1967. Here we have plotted a flare for which the shift is exceptionally large. If one interprets this shift as a Doppler shift, then we are observing here for the first time line-of-sight motions toward the observer of up to 300 kilometers per second.

It is informative to observe the development of the X-ray-emitting flare plasma as a function of time. Figure 3 is an example of the kind of observation we have made, in which (upper portion of figure) we observed simultaneously three different emission lines. As seen by our instrument, the flare apparently begins earliest in the chromospheric line of He II. Notice that the increase in intensity in this line is not large – only of the order of about 8 percent of the total of He II emission from the sun.

Coincident with the abrupt increase of intensity of He II, we have a radio burst, and at the same time the hot plasma emitting Fe XXV, helium-like iron, begins to appear. By studying the two profiles of this ratio burst (Figure 3), we have found it possible to infer the rate at which the hot plasma is created.

As the phenomenon progresses, we observe the line emission of lower stages of ionization of iron. In this case we are observing Fe XVIII. Presumably this emission comes about as a result of recombination from higher stages of iron through the lower stages of iron.

Evidently from an observation like this we learn immediately that the flare is not a steady-state phenomenon to which we can apply usual coronal theories; and it is evident that we will have to modify our current theories, in the light of such observations, to reflect the dynamic and changing characteristics of such an event.

Note in Figure 3 the increase in radio emission about one hour after the flare. This radio emission was reported as a metric Type IV emission which is usually attributed to synchrotron emission from relativistic electrons spiraling in magnetic fields several solar radii from the sun's surface. The combined data for this event suggest that particles may be subject to acceleration twice during the event. The first acceleration would occur at the time of the chromospheric flare, and of the initial radio burst. Apparently, as some of these particles travel away from the solar surface, a second acceleration occurs as they travel through regions of optimum magnetic field in the corona. The second acceleration then gives rise to the synchrotron emission.

Our instrumentation was not capable of determining from what locations on the sun the radiation came. However, Dr. James Underwood and I are currently working on instrumentation that will give us not only the spectra of these flare phenomena but, in addition, their detailed structural appearance in the solar chromosphere and corona.

MEMBER OF AUDIENCE:

I wonder to what extent the Orbiting Solar Observatory as it's now constituted technologically is starting to become obsolescent in terms of future studies, as opposed to what extent it is still useful in terms of permitting it to get the spatial and spectral resolutions necessary to extend these studies.

DR. NEUPERT:

Well, one of the—I think—outstanding attributes of the OSO is that—as it's now constituted, as you might say—is that it has been flown enough times that it has a high degree of reliability. The observations I have given here—and, of course, we have many more—are taken from 6,000 or 7,000 hours of observations, about one year of observations. And some of the emission lines we have seen only, let's say, six times in one year, because they are intense enough only during very strong flares. So one of the requirements for observing these phenomena is that you have to be up there for a long period of time. OSO serves that purpose very well. In addition, as we understand more about the OSO, we can upgrade, let's say, its pointing capability without, I think, changing the philosophy of it. Actually, our OSO III instrument is the first that has recorded some of the emission lines I discussed. I certainly wouldn't want to cut off such experimentation. We have no explanation for much of what we see here, and evidently there is much to be learned about basic phenomena on the sun.

MEMBER OF AUDIENCE:

My question was directed more to relative priority of the required upgrading rather than cutting off the sequence.

DR. NEUPERT:

I think that varies from experiment to experiment. We will be able to upgrade the kind of observations we are making without appreciable change of the OSO. But to go to somewhat more spatial and spectral resolution, we perhaps need to carry a larger pointed weight. That, perhaps, with more experiment power, might be the first thing to consider.

MEMBER OF AUDIENCE:

In the solar physics branch they have a slogan, and the slogan is: Love that OSO.

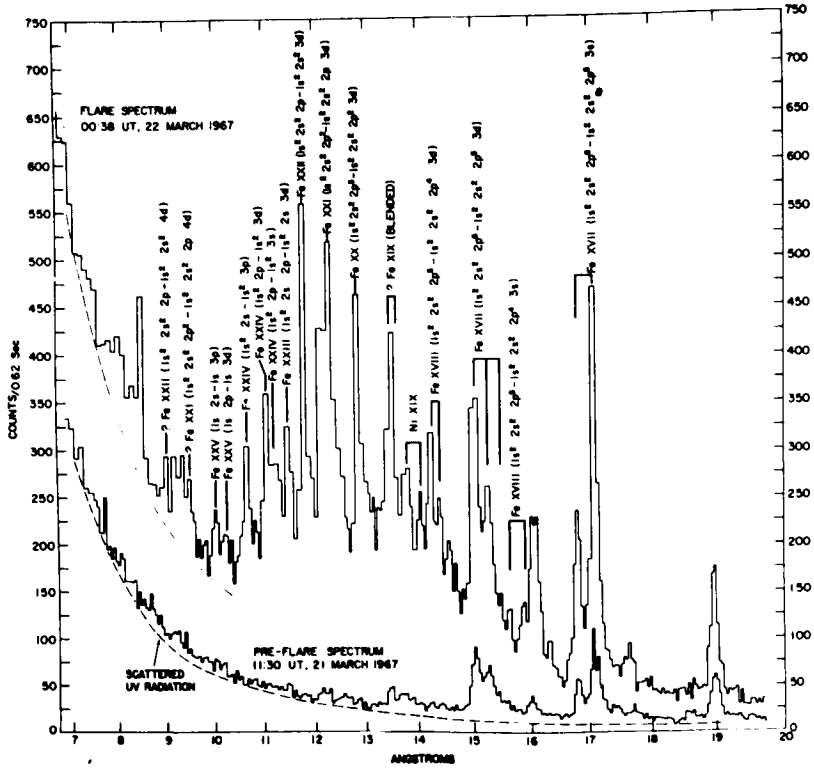

Figure 1

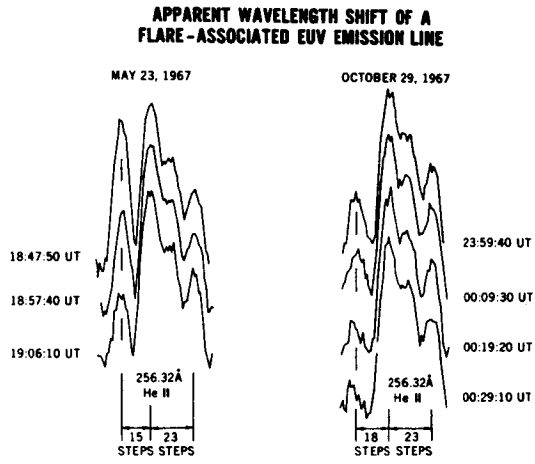

Figure 2

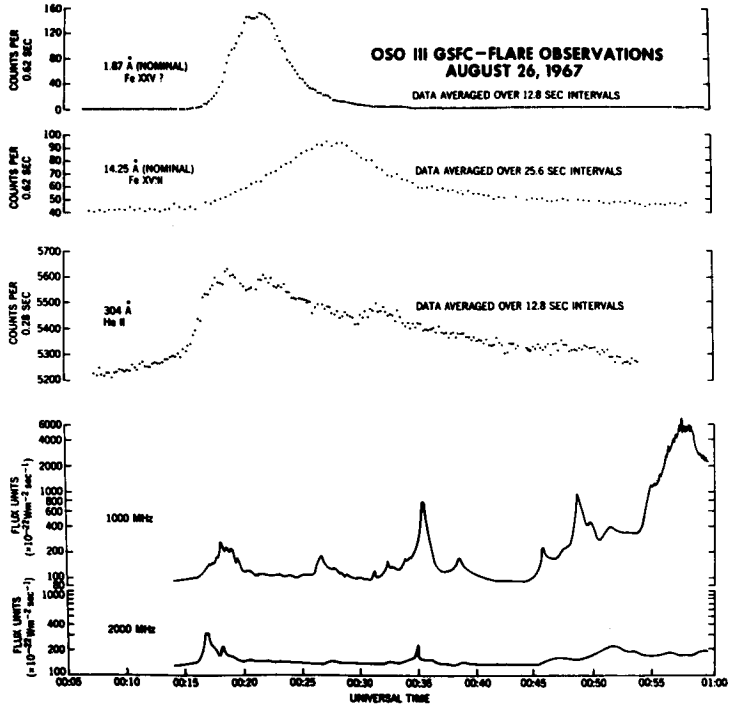

Figure 3

SOLAR RADIO BURSTS

Joseph K. Alexander, Jr.

CHAIRMAN:

Our next speaker is also concerned with emanations from the sun, but emanations in a different wavelength region. This is Mr. Joseph Alexander, and he'll talk about solar radio bursts.

MR. ALEXANDER:

Observations of solar radio bursts and of radio propagation phenomena are about the only means that we presently have for studying that region of the outer solar corona between about 10 and 100 solar radii. That is the region that is bounded on one side by what one normally thinks of as the corona as observed, say, with a coronagraph, and bounded on the other by the orbital distance of the earth, where we can make space probe observations.

Today I am going to describe how we have combined radio measurements obtained at high frequencies from the ground and from very low frequencies on satellite experiments to study one type of radio burst: a procedure which enables us to investigate the structure of active-region coronal streamers in the outer corona.

In Figure 1, I have a sample of the data obtained from a radiospectrograph at the Clark Lake Radio Observatory in Southern California, where we have an instrument that we share with the University of Maryland staff. This particular instrument sweeps very rapidly in radio frequency, in this case from 55 MHz down to 25 MHz; and we display the signal intensity that we observe in the radio frequency range as a function of time.

To get yourself oriented, the horizontal bands along the lower portion of the diagram are continuous levels of intensity from interference such as communications traffic; the bands at 5-MHz intervals here are put on by the instrument as a means of calibration; and the radio burst from the sun of interest in this case is the vertical feature between 1828 and 1829. We observe it to begin first at the high frequencies, in the

neighborhood of 45 to 50 MHz, and then it drifts very rapidly in frequency in a matter of seconds until it appears also down in the neighborhood of 20 to 30 MHz. In this particular frequency range it lasts for a matter of a fraction of a minute.

We picture this particular kind of radio burst as one that is being generated by a group of energetic particles that is accelerated from low in the corona rapidly out to higher distances in the corona, where the electron density is successively lower and lower. As this burst of energetic particles rushes out along the coronal streamer, it excites plasma oscillations close to the electron plasma frequency at each level, and then from the plasma oscillations we get electromagnetic radiation at successively lower frequencies corresponding to higher altitudes in the corona.

We can see in Figure 2 what this kind of radio burst looks like at much lower frequencies. This particular sample was obtained from the recent Radio Astronomy Explorer satellite. We display relative intensity as a function of time as observed by the satellite at several radio frequencies, going from the neighborhood of 4 MHz down to about 0.5 MHz. You can see in these intensity-versus-time profiles several typical features of this particular type of radio ourburst, such as the very rapid onset which drifts to occur at successively lower frequencies, and then the approximately exponential decay in time. From the decay of the bursts, which is thought to be due in part to electron-proton collisions in the coronal streamer, where the radiation is generated, we can analyze the electron temperature in the corona. If we then combine this with other information about the corona, we can attempt to generate a model of the density and temperature distribution in the coronal streamer where the bursts occur. And an example of this analysis is shown in Figure 3, where in this case the data were all obtained from an experiment on the ATS II spacecraft.

We have plotted here along the left-hand axis electron density in the corona as a function of distance from the center of the sun in solar radii. The right-hand axis shows the electron temperature. As I said, by analyzing the decay times of the radio bursts which are thought to be due to collision phenomena in the streamer, we deduce the temperature profile. For reference, the solid line labeled "average temperature" is a model of the temperature distribution in the average ambient solar corona. From the burst decay times observed on the ground and with the satellite experiment, we get for comparison a model of the temperature distribution in the active-region coronal streamer where the bursts are

thought to be generated. This analysis is performed by calculating the point in the corona where one has a pressure equilibrium between the gas and magnetic pressure in the average corona and the gas and magnetic pressure in the coronal streamer where we are observing the bursts.

The density distribution which goes along with the temperature model shown here for the coronal streamer is the line labeled "Model I." For comparison, the lower solid curve is a model of the density distribution in the average solar corona.

As a means of having a second alternative for investigating the models of the density and temperature distribution in the streamer, a separate calculation can be made in which one says, "Let's see what happens if the coronal-streamer electron temperatures are essentially equal to the average coronal temperature." One then gets a density distribution shown by the curve here labeled "Model II."

So, from an analysis of this particular type of radio burst, we can generate essentially limiting models to the temperature and density distribution in the active-region coronal streamer. Our own preference at this point, I think, is to favor Model II, which has the higher temperatures that are more consistent with the space probe measurements close to the earth and has the somewhat lower densities which show a smaller enhancement of the coronal-streamer density over the average coronal density towards the orbit of the earth. But to really resolve these two differences, we will be using the much more detailed measurements similar to the ones I showed you from the RAE satellite, which should enable us to learn a good bit more about the distribution of the streamers in the corona. Also, from studying the rise- and decay-time structure of the solar bursts, we can begin to study some of the physics of the mechanism that actually generates the radio bursts in the corona.

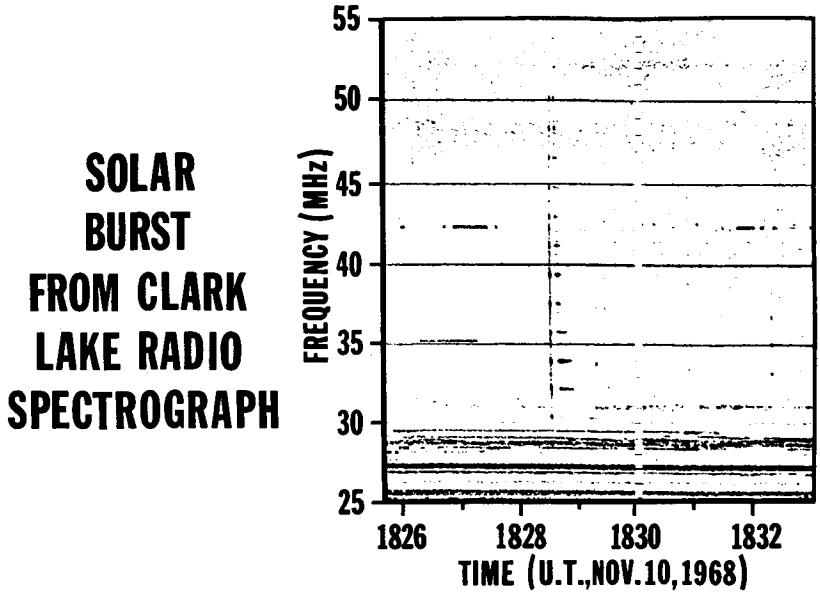

Figure 1

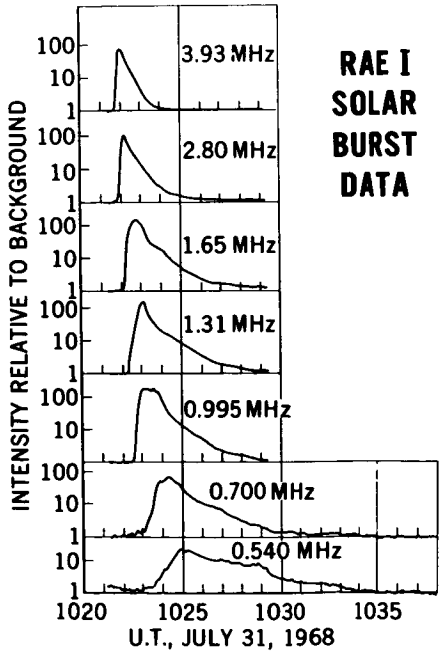

Figure 2

CORONAL STREAMER MODELS FROM ATS II DATA

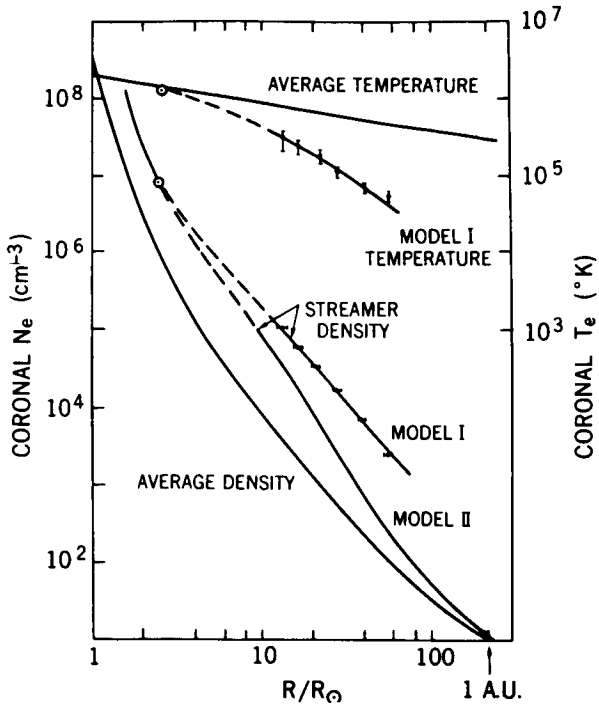

Figure 3

HIGH ENERGY SOLAR FLARE X-RAYS

Stephen S. Holt

CHAIRMAN:

. . . I'll proceed to ask Dr. Stephen Holt to discuss high energy solar flare X-rays.

DR. HOLT:

Very high energy X-rays—and by that I means X-rays with energies in excess of 100 kilovolts or so—are observed from the sun only during very large solar flares, and even then only for a very few minutes. Unlike the lower energy X-ray measurements you heard about a little bit earlier, which are essentially measures of the thermal nature of the emitting region, the very high energy X-rays are a direct reflection of the high energy electrons in the source region.

Figure 1, the lower trace represents the very high energy X-ray flux; these are X-rays about 80 kilovolts measured as a function of time on the OGO 3 satellite. There are several things to notice about this figure. The first is that the X-rays appear to have very impulsive onsets; there seem to be several bursts which comprise this emission. These onsets appear to have rise times of the order of seconds, while the decay time of each of these bursts seems to be about a minute.

If we compare the radio emission at the highest frequencies we measure (the upper trace is 17,000-MHz data measured on the ground for the same flare, July 7, 1966), the microwave emission appears to be identical to the trace of the X-ray emission, which leads us to believe that the source region for both these emissions must be the same. Therefore, whatever information we try to extract from the X-rays must be consistent with the radio emission.

In Figure 2, we have presented the differential X-ray spectrum measured at the time of maximum for this same flare, and you can see that it is well represented by a straight line on this log/log plot, which implies that the X-rays and, therefore, the electrons which produce the X-rays, must be well represented by a power law distribution. The two lines drawn in are for the two choices of the differential electron spectrum indicated.

The shape of this spectrum, it turns out, is preserved throughout the whole decay of the X-ray emission, a fact which leads to two important results. The first is that this power law representation must be a fair representation of the actual accelerated spectrum; and the second, that these electrons must lose energy predominantly by collision loss, since that is the only loss mechanism we can think of which preserves the shape of the spectrum in the absence of post-acceleration.

If we take the observed e-folding decay time of one minute, we deduce a hydrogen density of about 10^{10} hydrogen atoms per cubic centimeter. Knowing the hydrogen density and the absolute magnitude of the X-ray emission, we can, in principle, try to calculate the radio emission because we then know the total number of electrons. However, we have to bear in mind the fact that the radio emission is not a function just of the ambient magnetic field, because the actually observed radio emission depends also upon propagation and suppression effects which, in turn, depend upon the density and the pitch angle distribution of the electrons, and so on.

In Figure 3 we have tried to construct a few models which take all these parameters into account in order to fit the observed radio emission. The black dots are the observed radio emission, again for the same flare; these two traces are very, very simple models in the sense that we have assumed that the magnetic field is uniform and constant, and that the density is constant in the region. But we have been able to reproduce the general shape of the radio emission. In addition, the models demand that the observed radio emission should have a change of polarization; the asterisks represent where the observed change of polarization should occur. In fact, there is such a change of polarization observed at a frequency right between the two.

So that in addition to finding, from the X-ray data alone, that the acceleration of the electrons appears to be impulsive with a power law distribution in the spectral shape, consistency with the radio data demands that the source region for the X-ray emission must have a density of something like 10^{10} hydrogen atoms per cubic centimeter, and that the ambient magnetic field in the region must be something like 250 gauss.

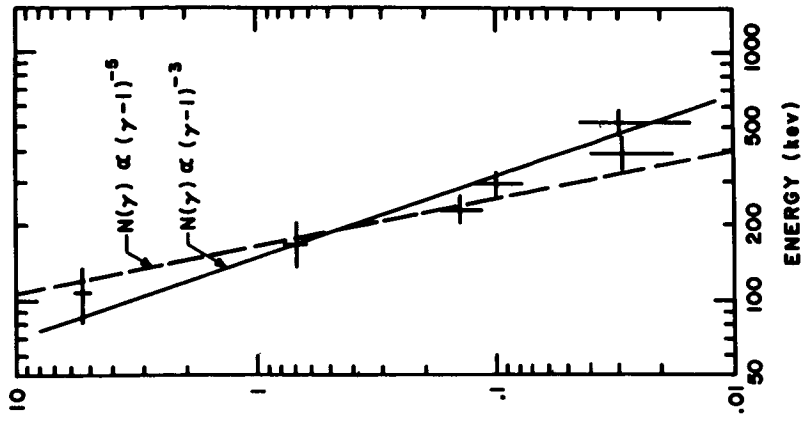

Figure 2

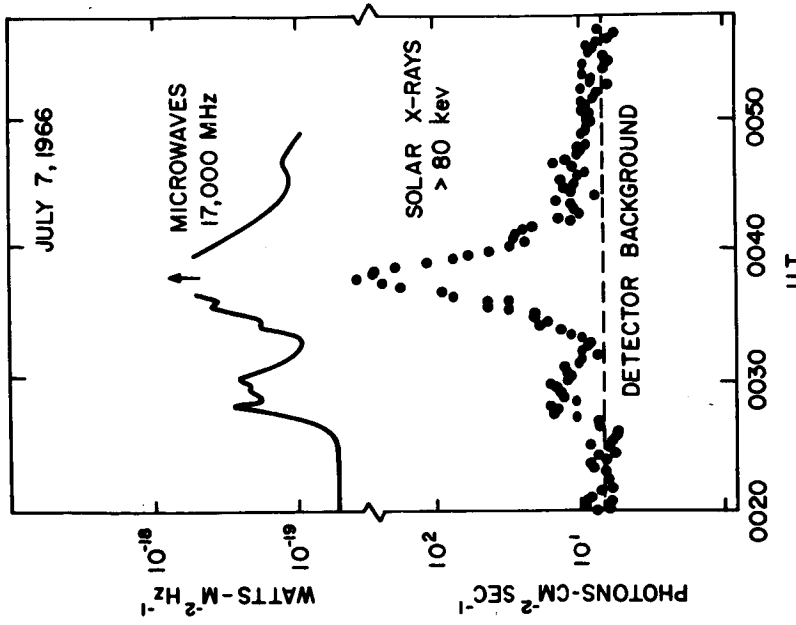

Figure 1

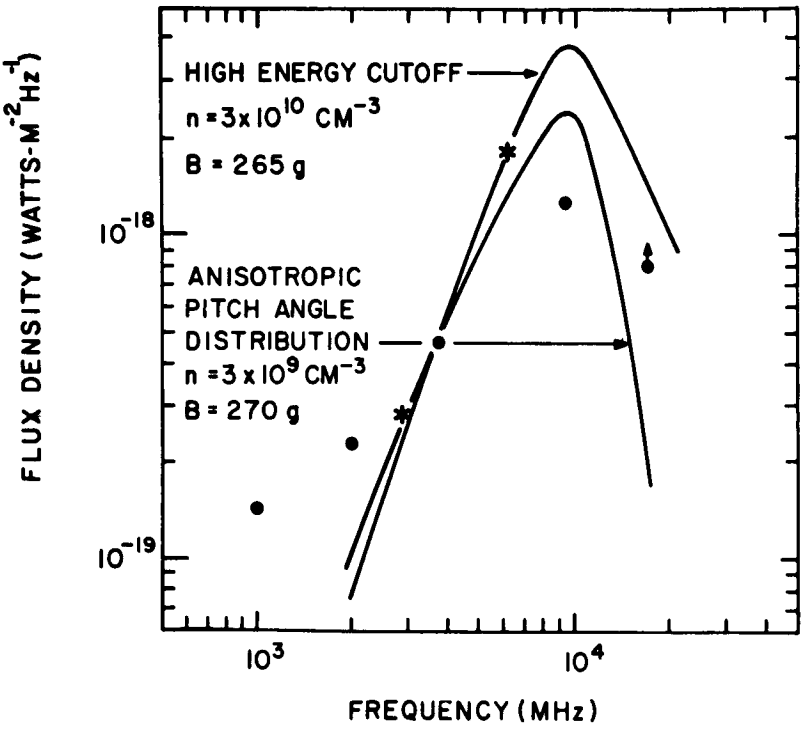
HIGH ENERGY CUTOFF
n = 3 x 10^10 CM^-3
B = 265 g
ANISOTROPIC
PITCH ANGLE
DISTRIBUTION
n = 3 x 10^9 CM^-3
B = 270 g
10^-18
10^-19
10^3
10^4
FREQUENCY (MHz)
FLUX DENSITY (WATTS-M^-2Hz^-1)

Figure 3

What we (C. Wolff, J. Cassinelli, and myself) have done is attempt to construct a self-consistent model of the solar wind which allows for solar rotation and which has the magnetic field included. The three basic equations are the equation of motion, the equation of continuity, and an energy equation which is simply a bookkeeping device that tells you the form in which energy is being carried along. We have been careful about putting in all of the relevant forms of energy transport (we believe); the most important one is transport by electron conduction. This was specifically not included in the earlier models. There was an attempt to include it by adopting a mean polytropic index, but this didn't turn out to be terribly successful. The improvement in this model over the previous models lies in the details of the energy equation.

The model is in good agreement with observations at quiet times near the orbit of earth. It has a temperature of 300,000°K, a velocity of 315 kilometers a second, and an electron density of 6.4 per cubic centimeter. These are reasonable values, as I said, for quiet times; and this is a particularly relevant place to make the comparison, because it's only at quiet times that you are likely to have one of the other assumptions that is built into the problem, namely, azimuthal symmetry. You assume as you go all the way around the sun that the solar wind is more or less the same all the way along. This is undoubtedly not true during active times, and hence this comparison is appropriate.

If we look at Figure 1, this is the solution for the azimuthal component of the solar wind velocity, and this follows directly from the radial solution. If you have the radial solution there is an equation for the azimuthal velocity. It reaches a maximum rotational velocity, azimuthal velocity w_ϕ , of 7.5 km/sec, and this occurs at about 15 solar radii. It then decreases to a value of 2.5 km/sec near the orbit of earth; the value of 2.5 is within the probable error of the measurements for quiet times. The Alfvén point r_A (where the radial Alfvén speed and the radial bulk velocity are equal) is marked. It is in fact the properties of the solar wind at the Alfvén point which determine the azimuthal velocity at the orbit of earth.

The integrations are a little tricky. There are three critical points in the solution, and the solution must pass through all three of them. I won't dwell on this point. It's simply a practical pain in the neck that has to be taken into account.

Lastly, in Figure 2, we will have a look at the solution as it comes into the solar corona. The distance from the sun in solar radii is plotted versus the electron densities which have been determined through decades of eclipse observations. You see that the solution does fairly well. The

THE SOLAR CORONA AND THE SOLAR WIND

John C. Brandt

CHAIRMAN:

So at this point then I will call for the next talk since the continuity is reasonable, and ask Dr. John Brandt to discuss the solar corona and the solar wind.

DR. BRANDT:

The solar wind provides not only a physical but a logical connection between the sun and the other bodies in the solar system, and we get at no extra charge a very nice plasma physics laboratory to see if we know what we are doing in this particular field.

Up until fairly recently, most of the available models of the solar wind ignored a rather substantial amount of the physics involved: namely, they assumed that the sun was nonmagnetic; they assumed that it didn't rotate; and by and large they assumed it was inviscid.

Here, I would like to focus briefly on the fact that the solar wind has an azimuthal or rotational component besides the radial flow out of the sun. This component arises because the sun is rotating and because the magnetic field lines tend to couple the outflowing plasma to the sun, and to some degree there is a tendency towards co-rotation. Naturally, if you wish to treat this problem, one must construct models with the sun rotating and with the magnetic field included.

There have been attempts at these, but the agreement has been poor. We have observations of what the azimuthal velocity is near the earth, both by studies of comets and from space probes, and we know that the value is somewhere in the range about 2 kilometers per second or higher; a value of 2 to 6 kilometers a second would be appropriate for quiet times. The available models give values of 1 kilometer or less, and in some cases much less. On the other hand, the model, if we are to believe it, must reproduce the corona. It should look like the corona; the density should be approximately correct. Some of the models that have been constructed so far do not look like the corona. These models miss the density by about a factor of 10, and the solution is really not applicable.

model with the solid dots comes from Allen's *Astrophysical Quantities*, which is kind of a bible on these things. The error bars correspond to an assumed error of 50 percent, which is quite optimistic considering the accuracy. The other two models are models constructed by van de Hulst and by Michard. Both are supposed to be quiet sun models. You can see there is quite a bit of disagreement. But luckily the solution goes sort of through the whole lot.

We know that the solution should not be extended below about two solar radii, and the reason for this is the fact that energy deposition due to mechanical heating of the corona is important below two solar radii, and if you wish to go into this region you must have a source term in the energy equation. We do not have it and for good reason: it is very hard to specify. But that is not particularly relevant; one can fit the model outside of this region.

The conclusion here is that we have a model which is in reasonable agreement with observations near the sun and in reasonable agreement with spacecraft near the orbit of the earth.

One of the reasons for investigating such a model is to compute the e-folding time for braking of the sun. This is an angular momentum sink, probably the most important angular momentum sink in the lifetime of stars like the sun. This will brake the solar rotation by a factor of e in 5×10^9 years, which sounds like rather an inefficient process; but, of course, that figure is the age of the sun. So a considerable amount of braking is going on, and we have now direct evidence for this.

This is certainly not a final or definitive model, but I do think it is an improvement over what has been available previously.

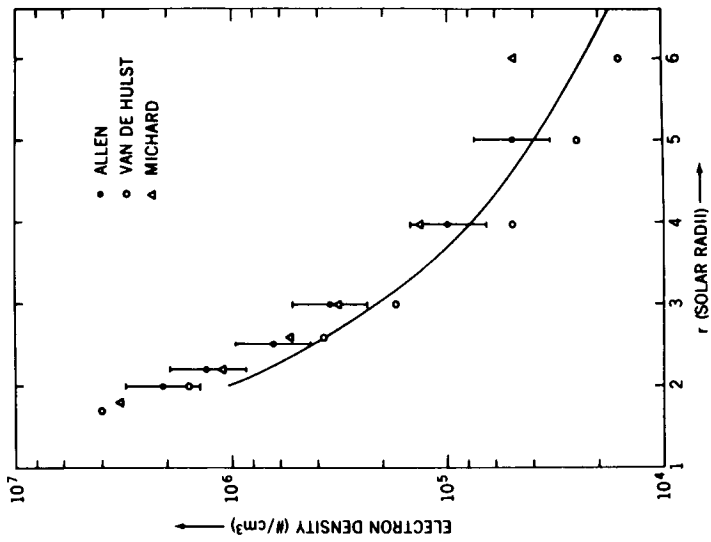

Figure 2

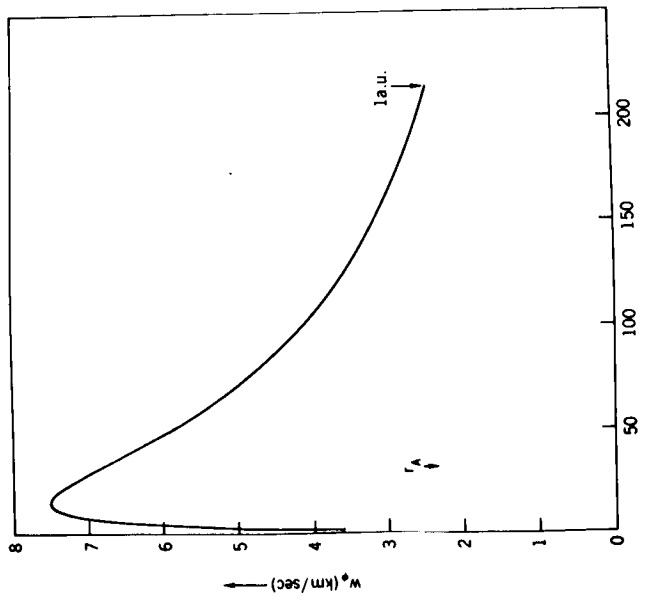

Figure 1

INTERACTION OF THE SOLAR WIND WITH THE MOON

Norman F. Ness

CHAIRMAN:

This afternoon's session is concerned with interplanetary space and its characteristics and the characteristics of the particles and radiations that populate it, and with astronomy in the many forms as practiced here at Goddard. To begin the session, I will ask Dr. Norman Ness to speak on the interaction of the solar wind with the moon. Dr. Ness.

DR. NESS:

We are all familiar with the significant effects of the solar wind interaction with the earth's magnetic field. Shown schematically in Figure 1 in a noon-midnight meridian plane is the manner in which the solar wind contains the geomagnetic field. We see the radiation belts and the quasi-trapped particles forming the magnetosphere and also see lines of force extended behind the earth that form a magnetic tail somewhat analogous geometrically, and perhaps physically in its properties, to cometary tails.

In 1966 the Soviet spacecraft Luna 10 was placed in orbit about the moon, and during a full-moon period the Soviets reported no evidence for the existence of the earth's magnetic tail. In 1966 also, the United States launched an abortive attempt to orbit the moon, Explorer 33, but with a secondary orbital capability of very high apogee. This spacecraft established definitively the existence of the geomagnetic tail out to 80 earth radii.

There are other results associated with the Luna 10 spacecraft which were somewhat difficult to comprehend. Figure 2 presents one theoretical model for the solar wind interaction with the moon. In the absence of an appreciable lunar magnetic field, the solar wind directly impacts the lunar surface, the bow shock is not detached but is tied on to the lunar surface, and a pseudo magnetosphere is formed associated with magnetic field lines conductively trapped in the interior of the moon. Luna 10 reported evidence for the existence of a pseudo magnetosphere.

In 1967 the United States was successful in launching Explorer 35 in orbit about the moon, and since that time we have studied magnetic field, plasma, and particle data in investigating the physical environment of the moon. I summarize results principally from the GSFC magnetic field experiment worked on jointly with my colleagues, Ken Behannon, Y. C. Whang, and Harold Taylor.

Figure 3 shows a typical set of experimental data as the spacecraft passes behind the moon. The sketch in the upper left-hand corner projects the orbit on the plane of the ecliptic. As the spacecraft passes behind the moon through the optical shadow and therefore also the solar wind shadow, the direction of the magnetic field changes only slightly, if at all, through this shadow region. No evidence is found for the existence of a shock wave; no evidence is found for significant distortion of the interplanetary magnetic field. Small perturbations of the magnitude, however, plus and/or minus in the penumbral regions, a positive anomaly in the interior in the umbral region, and a negative anomaly are noticed in this pass through the plasma shadow.

Depending upon solar wind conditions, the magnitude and the location of the magnitude anomalies change. But the conclusion is always reached that the direction of the interplanetary magnetic field is never much distorted behind the moon when compared with the interplanetary magnetic field direction in front of the moon. These results do not support those of Luna 10.

A recent theoretical study of the solar wind flow past the moon assumes that the moon acts as a sponge so that it absorbs the entire solar plasma flow, creating a plasma void. The readjustment of the interplanetary magnetic field as it is convected through the lunar body leads to the induction of currents associated with the diamagnetic plasma.

Figure 4 summarizes the theoretical results. Projected on a plane defined by the direction of the magnetic field and the solar wind velocity, the plasma shadow is seen. Electrical currents induced in the penumbra regions distort the interplanetary field slightly and lead to magnitude anomalies as large as 25 percent plus in the umbra and a few percent minus in the penumbra regions.

A complete study of the theoretical problem is extremely difficult because the real solar wind is anti-isotropic at times, since it is a magnetized medium. This limited first solution however, confirms our experimental results and suggests that the moon itself is not sufficiently

conducting electrically to accrete the interplanetary magnetic field, as had originally been hypothesized might be possible by Gold and others.

Figure 5 relates to our physical interpretation of these results. The moon is not sufficiently electrically conducting in its interior to accrete the interplanetary magnetic field, nor in fact to have any effect as slight changes are propagated through the body. We have deduced an effectivy electrical conductivity of 10^{-5} mhos/meter. As a function of lunar depth we have assumed an olivine model characteristic of the earth's mantle material and assumed a chondritic meteorite radioactivity composition in the moon. If the moon is old, say 4.9 billion years, and melting takes place at a depth greater than 300 kilometers, then the electrical conductivity would be extremely high. Our experimental results exclude this possibility. If the moon is very young, less than one billion years old, then we are within the realm of a chondritic composition moon, i.e., a relatively cold moon, since it is the temperature of the interior of the moon which determines the electrical conductivity.

These results suggest that the moon is relatively nonconducting electrically, relatively cold, and a body which absorbs the particle flux incident on its surface and does not give much support, at least at the present time, to a "hot moon" theory.

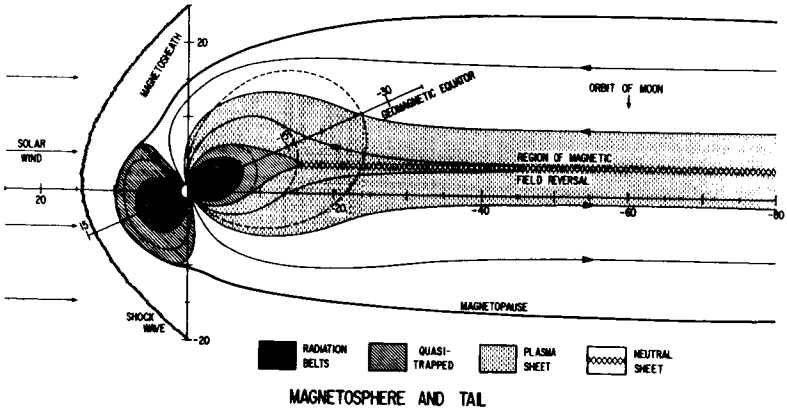

Figure 1

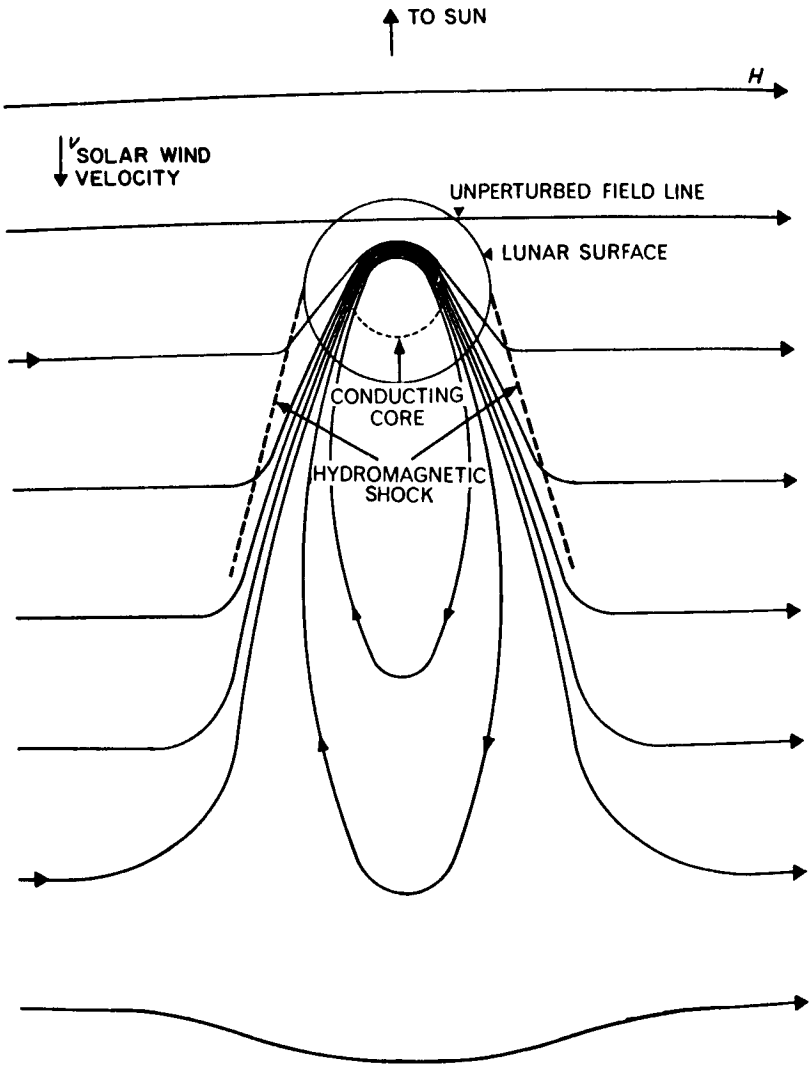
TO SUN
H
SOLAR WIND
VELOCITY
UNPERTURBED FIELD LINE
LUNAR SURFACE
CONDUCTING
CORE
HYDROMAGNETIC
SHOCK

Figure 2

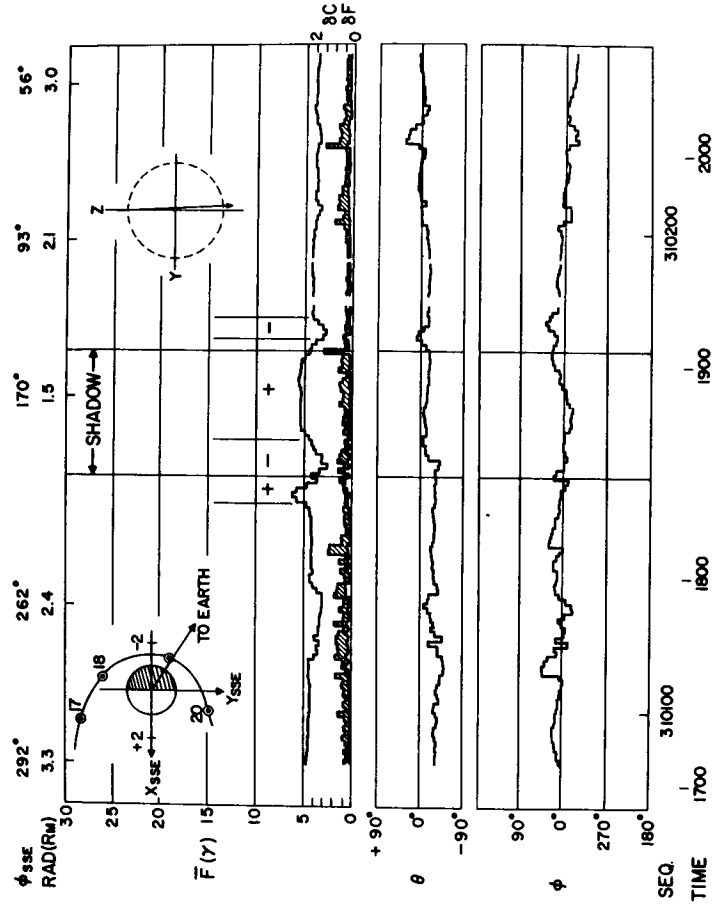
ϕ_{SSE}
RAD(Rм)
292°
262°
170°
93°
56°
3.3
2.4
1.5
2.1
3.0
SHADOW
TO EARTH
X_{SSE}
Y_{SSE}
Z
Y
$\bar{F}(\gamma)$
30
25
20
15
10
5
0
δC
δF
+90°
0°
-90°
θ
90°
0°
270°
180°
φ
SEQ.
TIME
310100
310200
1700
1800
1900
2000
23 APRIL 1968

Figure 3

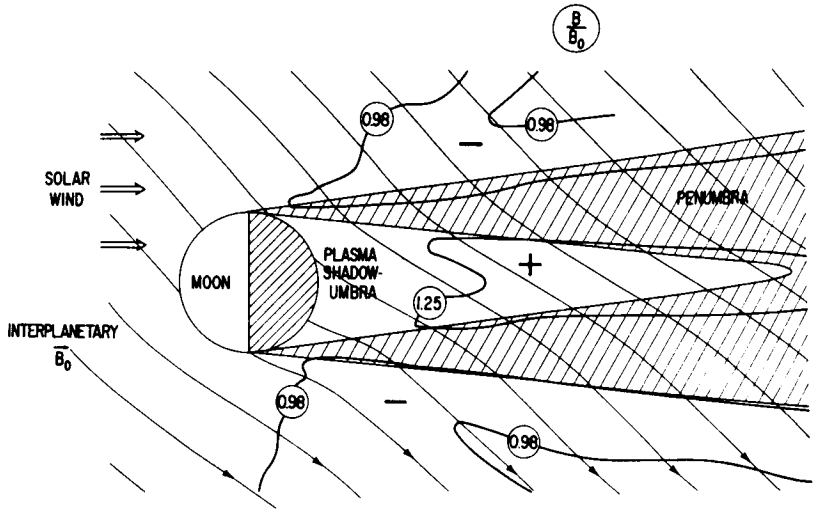

Figure 4

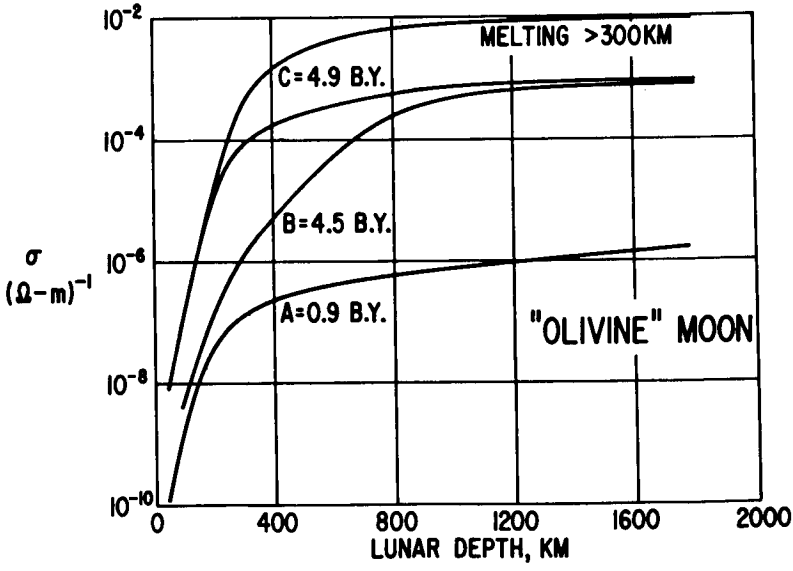

Figure 5

HYDROMAGNETIC DISCONTINUITIES IN THE SOLAR WIND

Leonard F. Burlaga

CHAIRMAN:

Our next speaker continues the discussion of the properties of the solar wind. He will discuss hydromagnetic discontinuities in the solar wind. This is Dr. Leonard Burlaga.

DR. BURLAGA:

The early studies of the interplanetary medium were concerned primarily with its average properties on a scale such as you see in Figure 1. It was established, by direct observations, that within about ± .3 astronomical unit of the earth there is a hot plasma streaming more or less radially from the sun with the velocity $\vec{V}$, and carrying with it a fluctuating, spiral-shaped magnetic field $\vec{B}$.

With the availability of more accurate and high-time-resolution magnetic field and plasma data, it is now possible to look at the interplanetary medium on a much smaller scale. In effect, we can magnify regions that are relatively the size of the small dot near the top of Figure 1 and study the structure of these regions in detail.

In addition to giving morphological results of astronomical interest, such microscale studies provide an opportunity to study fundamental physical processes under conditions which can't be simulated in the laboratory—processes involving the balance and exchange of magnetic-field and particle energy under conditions where the magnetic field energy density and the particle energy density are comparable.

I shall first describe some observations of just one type of microscale structure which I have found, then I shall show how they can be interpreted in terms of hydromagnetic theory, and finally I shall show you how one can apply these results to establish that the electrons are sometimes hotter than protons in the solar wind.

Figure 2 shows some microscale observations from Pioneer 6. At the top of the figure is the magnetic field intensity measured in gammas; the

magnetic field direction is shown in the next two blocks; then follow the plasma proton density, the thermal speed (which is a measure of the temperature), and bulk speed. These six categories are plotted as a function of time for an interval of one hour. The plasma data were obtained by Bridge and Lazarus of MIT, and the magnetic field by N. Ness.

The most significant feature in Figure 2 is the cascade of discontinuities. You can see that across each discontinuity there is a decrease in the magnetic field intensity and a corresponding increase in the density. There is essentially no change in the thermal speed throughout this entire region.

These observations are readily explained in terms of hydromagnetic theory. This theory predicts that there can exist discontinuities across which any changes of plasma and magnetic field parameters can occur, subject to the condition that the sum of the particle pressure and the magnetic field pressure is the same on both sides of the discontinuity.

You can see that, at each discontinuity in Figure 2, an increase in density causes an increase in particle pressure, but this is compensated by a decrease in the magnetic field pressure. The pressure balance is demonstrated more precisely in Figure 3, where the magnetic field intensity squared is plotted versus the density, for the points in the region in Figure 2. Note the linear relationship. This relationship and the fact that the proton temperature was a constant throughout the region imply that the pressure was a constant throughout the entire region. Thus, in particular, the pressure was continuous across each of the discontinuities in the region as required for a tangential discontinuity.

Electrons as well as the protons contribute to the pressure balance. From the slope, s, of this line, one can determine the ratio of the electron temperature to the proton temperature. During this determination, I found that the electrons are about four times as hot as the protons, thus qualitatively confirming the theoretical prediction of Sturrock and Hartle.

These results represent the first observation of a hydromagnetic tangential discontinuity under interplanetary conditions, and the first determination of the ratio of the electron temperature to the proton temperature. They illustrate some of the results that we have obtained from microscale studies during the past year.

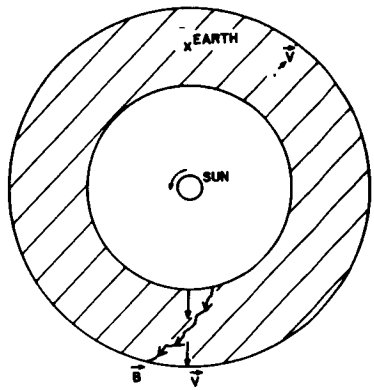

Figure 1

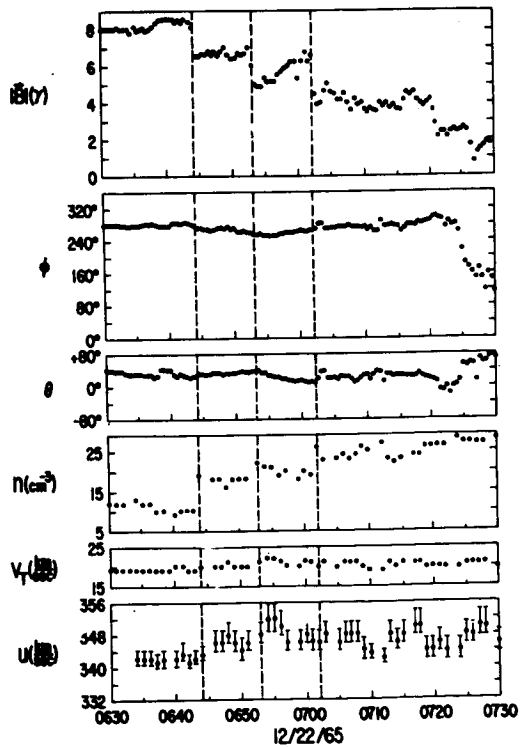

Figure 2

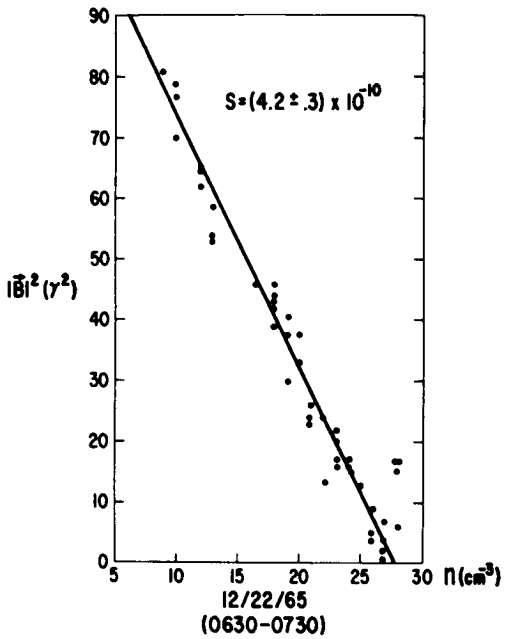

Figure 3

COSMIC RAY AND SOLAR FLARE ELECTRONS

Thomas L. Cline

CHAIRMAN:

Our next subject moves to the cosmic radiation. Dr. Thomas Cline will talk about cosmic ray and solar flare electrons.

DR. CLINE:

Cosmic radiation is one of the oldest of the topics we are discussing today. Certainly it is the granddaddy of the various particle disciplines in the space sciences. As you know, it originally developed as the study of properties of the relativistic protons and other nuclei from beyond the solar system, and later came to include the study of similar particle radiations from solar flares.

Our personal interest has lately been in the relativistic electrons and positrons in both the galactic and the solar radiations, and in their related X-rays. These particles have kinetic energies from a few hundred kilovolts to a few Mev, in the vicinity of, and somewhat above, the electron rest-mass energy. This research program is thus somewhat analogous to the classical study of cosmic-ray protons near 1 Bev. Moreover, these particles are uniquely related to cosmic-ray and solar protons and to certain electromagnetic radiations, in such a way that their study eventually should disclose a considerable amount of information on the nature of the cosmic-ray and solar processes—information which is unavailable by other means. These particles can, of course, be observed only with spacecraft beyond the earth's immediate environment. The solar X-ray studies stemming from our program were outlined earlier today by Stephen Holt; the positron observations also are relevant, but the details of those experiments are outside the scope of the short outline that follows.

Concentrating on the interplanetary electrons of energies above 1 Mev, we have in Figure 1 a compilation of the observed intensities of cosmic-ray electrons versus energy; one can see that this spectrum has a definite structure, as it might if it were influenced by several parameters. About a decade ago, theoreticians predicted the existence of electrons having energies in the Bev region like cosmic-ray protons; these particles

were subsequently observed by means of balloons. For the following several years, the spectrum was expected to be flat below 25 to 100 Mev, since the electron intensity was calculated on the assumption of a single source, namely, meson production in interstellar space. However, with data from F. McDonald's IMP 1 cosmic-ray detector in 1964, we found a component of increased intensity in the very-low-energy relativistic region. The study of this interplanetary population of electrons, with velocities like those of cosmic-ray protons, was augmented during 1968 with the IMP 4 results of Simnett and McDonald, using data taken in 1967, and by our own results from a new electron detector flown in 1968 on OGO 5. These observations, shown in Figure 1, verified the existence of this intensity turn-up at the low-energy end and determined its spectral value perhaps somewhat more accurately, depending on assumptions of solar modulation during the intervening years.

Comparisons between the observed spectrum and the calculated details of the electron spectrum that one expects from cosmic-ray production show several interesting features. First, knock-on electrons of a few Mev energy result only from interactions in interstellar space of cosmic-ray protons of very high energies; second, the high-energy electrons at or above 100 Mev result from meson production by protons of medium to high energies. The spectrum of electrons resulting from direct acceleration is less easily predicted. Positron production, on the other hand, results only from secondary production and can be accurately calculated; the higher-energy positrons, again, come from meson production by very energetic cosmic rays, and positrons near 1 Mev result from beta decays of excited nuclei. Finally, the production rate for this last-named interaction is sensitive to the intensity of very-low-energy cosmic rays. This quantity is unknown, being extremely distorted by the modulation of cosmic rays in the solar system. Thus, the comparison between these calculations and the intensities of positrons and of electrons at all energies will, in fact, provide the only direct handle on the unmodulated, or interstellar, cosmic-ray proton spectrum, particularly at the low energies, where the uncertainty may be the greatest.

Already several results have begun to emerge. First, the fact that, at the low-energy region from 2 to 10 Mev, the electron data do fit the calculated knock-on spectrum fairly well shows that the hypothesis of a galactic origin of these interplanetary electrons is tenable; also, the relative amount of soft-shower, or degraded meson-decay, electrons, indicating a large travel path, must be small. By comparison, the low-energy electron component deep in our atmosphere is mostly composed of soft showers, in which the positron-to-electron ratio is about 0.5. Consistant with this

knock-on fit is the result from our OGO 5 experiment, not illustrated here, that the positron-to-electron ratio at a few Mev is quite low, perhaps about 0.1. Finally, these results also indicate that, since knock-ons are the main source of electrons at those energies, a comparison with calculations shows that the cosmic-ray proton spectrum at several Bev, outside the solar system, is very much like that inside.

The other contributor to the population of interplanetary electrons of a few Mev energy is the production by solar flares. In Figure 2 are shown distributions of the intensities of solar particles observed after one flare. These are the first directly detected interplanetary solar-flare electrons of relativistic energies. This observation, which we made with F. McDonald using IMP 3 has been recently supplemented by a variety of solar-flare electron data from IMP 4 and OGO 5. In this figure, the observed intensity distributions of 3 to 12 Mev electrons and of three different energy groups of protons from the flare of July 7, 1966, are plotted. On the left are the time histories; on the right, taking into account the velocity parameter for each population, are the intensity distributions against distance traveled. These transformstions were made by converting from time to distance traveled with a common normalization at peak intensity. These curves not only fit each other; but also fit the calculated curve for simple diffusion, when the zero of time is adjusted to the injection time.

These results have several implications: First, all observed solar particles may, under the appropriate circumstances, obey simple diffusion in a velocity-ordered manner which is independent of the rigidity parameter. Second, this result allows one, for the first time, to calculate the source spectra of relativistic flare electrons. Third, it is found by comparison with our X-ray results that only a small fraction of the electrons generated at the sun can escape from the X-ray-generating region into interplanetary space. And, fourth, by variation of the zero of time in the calculated diffusion fit (not shown in Figure 2) to fit the electron data from IMP, the electron injection time was empirically found to be essentially identical to the X-ray burst time we observed with OGO 3. This result confirms the identification of the interplanetary solar electrons as being from the same population of solar electrons responsible for the microwave and the X-ray bursts.

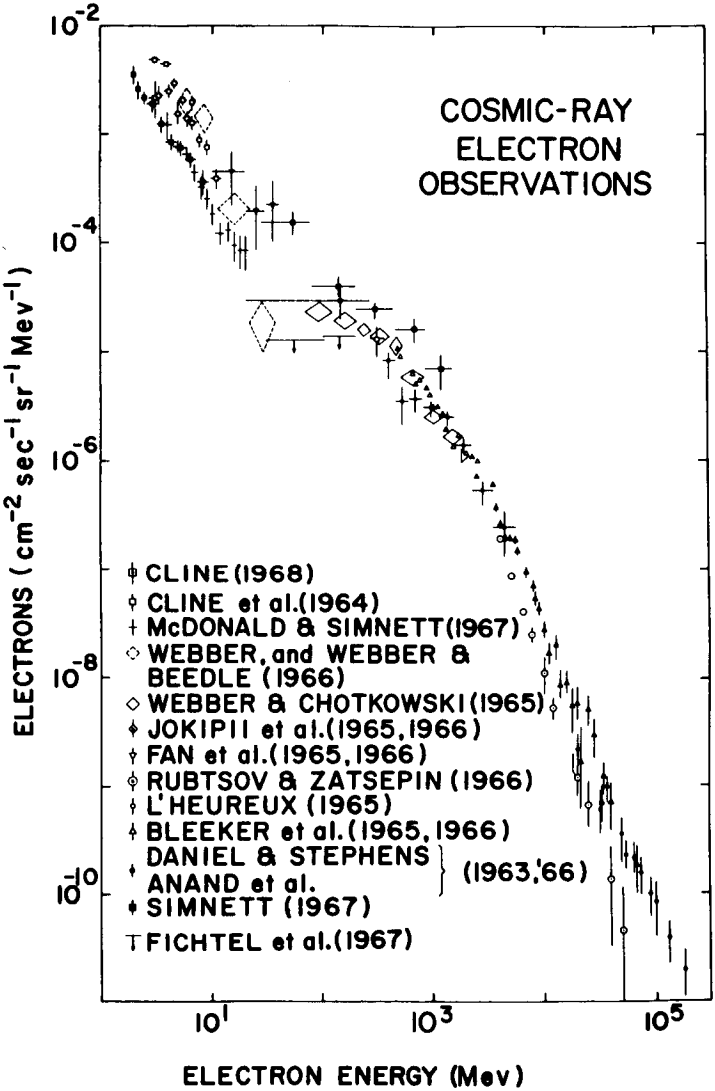
COSMIC-RAY
ELECTRON
OBSERVATIONS
CLINE (1968)
CLINE et al. (1964)
McDONALD & SIMNETT (1967)
WEBBER, and WEBBER & BEEDLE (1966)
WEBBER & CHOTKOWSKI (1965)
JOKIPII et al. (1965, 1966)
FAN et al. (1965, 1966)
RUBTSOV & ZATSEPIN (1966)
L'HEUREUX (1965)
BLEEKER et al. (1965, 1966)
DANIEL & STEPHENS
ANAND et al.
(1963, '66)
SIMNETT (1967)
FICHTEL et al. (1967)
ELECTRONS (cm⁻² sec⁻¹ sr⁻¹ Mev⁻¹)
ELECTRON ENERGY (Mev)

Figure 1

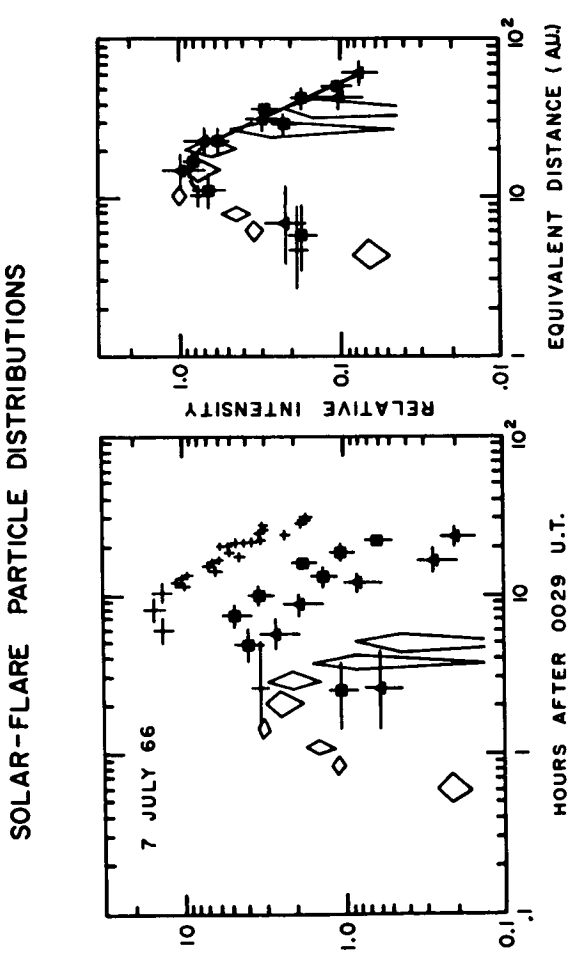
SOLAR-FLARE PARTICLE DISTRIBUTIONS
7 JULY 66
PARTICLES (cm⁻² sec⁻¹ sr⁻¹)
RELATIVE INTENSITY
HOURS AFTER 0029 U.T.
EQUIVALENT DISTANCE (A.U.)
▲ = 59 TO 80 Mev PROTONS (R = 330 TO 400 Mv, β = .34 TO .39)
■ = 38 TO 59 Mev PROTONS (R = 260 TO 330 Mv, β = .28 TO .34)
+ = 16 TO 38 Mev PROTONS (R = 175 TO 260 Mv, β = .18 TO .28)
◇ = 3 TO 12 Mev ELECTRONS (R = 3.5 TO 12.5 Mv, β = 0.99)

Figure 2

GALACTIC AND SOLAR COSMIC RAYS

Frank B. McDonald

CHAIRMAN:

Our next speaker will be Dr. Frank McDonald, who will talk about galactic and solar cosmic rays.

DR. McDONALD:

The galactic cosmic rays provide us with our only direct sample of matter originating outside the solar system. In the past few years, with the evolution of particle detectors, with the availability of scientific spacecraft with orbits outside the magnetosphere, such as IMP and OGO, we have been able to analyze the chemical composition of this relativistic interstellar gas with a precision that is much greater than we had formerly been able to achieve for stellar and solar composition. It is these measurements that I would like to discuss briefly today.

First, how does one do chemical composition on elements that are close to relativistic velocities? I'd like to illustrate this by showing in Figure 1 the detector system that was flown on OGO 5. In this system we see examples of how one does multiple parameter analysis.

In the first device, which is a dE/dx Cerenkov counter, one measures two parameters: the Cerenkov output, which is proportional to $Z^2(1 - 1/\beta^2 n^2)$, where β is the ratio of the velocity of the particle to c (the velocity of light); and for dE/dx, one measures a quantity which is proportional to Z^2/β^2. And so from this you can isolate particles according to Z, the charge, and according to the velocity.

Now in the second device, what we do is measure the particles which stop; and so, in addition to measuring dE/dx, we also determine their total energy. The same thing is true in the solid-state device to the right, which goes down to much lower energies; and so with these devices we measure $dE/dx \sim Z^2/\beta^2$, and then we measure the total energy, which is $\sim m\beta^2/2$. This means as we go down to stopping particles, we now have a mass spectrometer as well as identifying the various elements. It is this multiple parameter analysis, free of atmospheric and magnetospheric effects, which enables one to do much more precise studies on the chemical composition.

To show what kind of charge distributions we get, Figure 2 shows a representative sample from OGO 5. This was done in collaboration with Bonnard Teegarden, V. K. Balasubrahmanyan, and originally George Ludwig. And what we see here then is the very excellent resolution of individual elements.

Now, back when John Naugle was doing this, they used to divide things up into Z greater than 10, and carbon, nitrogen and oxygen, and then lump lithium, beryllium, and boron together and worry about the spillover between boron and carbon.

I think my wife is convinced that the reason we made such progress is the fact that we have got the woman out of the system, the nuclear emulsion scanner. And so that's probably the principal reason for the improved resolution - - -

VOICE:

(Unintelligible.) (Laughter.)

DR. McDONALD:

So what we see is a very pronounced even/odd effect as we go carbon, nitrogen, oxygen. Then as we look at a lower scale here, we see neon; we actually see evidence that fluorine is resolved despite the evidence to the contrary from the anti-fluoridation league at the University of Chicago, who was claiming for a long time that there was no fluorine, and now we see it well resolved. And now we jump along and see neon, magnesium, silicon with the intervening odd elements not resolved as yet.

The other surprise which people have known for a long time was the presence of lithium, beryllium, and boron, which we see now more clearly and more accurately.

Now what we can do as a first step is to look at the measurements of lithium, beryllium, and boron; we know they shouldn't be in the source region, simply because the temperatures are too high; they would be destroyed by the nuclear reactions that would take place. They have to be generated by the fragmentation of carbon, oxygen, and heavier elements. We can run these energetic heavy nuclei through the standard slab of interstellar gas and calculate how much material we have to have to produce the observed lithium, beryllium, and boron. It turns out that if

we know the nuclear cross-sections for the fragmentation, this turns out to be 4.5 grams, with the precision really being limited by our knowledge of the fragmentation parameters.

Now we can check this to a second order by looking at the production of other secondary particles such as helium 3 and deuterium. We look there; again we see the same 4 to 5 grams.

There is a third-order correction, a third-order test, which we can apply, and in Figure 3 we see the energy distribution of carbon, oxygen, boron, and neon. Now the effect that one expects to see coming into play because of the presence of the 4.5 grams, as one goes to lower and lower energies, is the suppression, say, of carbon and oxygen relative to helium. In other words, if one makes a diagram of the ratio of carbon to helium, if there were no material this would simply be a constant. Then assume (and it's valid, probably, encouraged by the fact that this is what is observed by Fichtel's group here in solar cosmic rays) that carbon and helium have the same energy spectrum at the source.

Now, if you add material, you expect the low-energy carbon to lose its energy at a faster rate than the helium nuclei of the same velocity, and to fall out of the beam, and so the relative spectra will drop off as you go to lower energies. What one sees—the ratio of carbon to helium—is actually rising as one goes down below 100 Mev. So while we have a model for simple injection and diffusion which explains the major features, when we go and look at the secondary features, then we find that some revision to the basic model is needed. And we don't have the answer yet. People have proposed that one add local sources nearby in the galaxy, which are rich in heavy elements. This rectifies this particular situation, but doesn't explain why one sees so much low-energy helium 3, lithium, beryllium, and boron. So it means we are going to have to go back and change some of the simple assumptions used in the original model.

CHAIRMAN:

Thank you, Dr. McDonald. The problem you thought you had solved isn't solved at all.

DR. McDONALD:

It keeps us off the street.

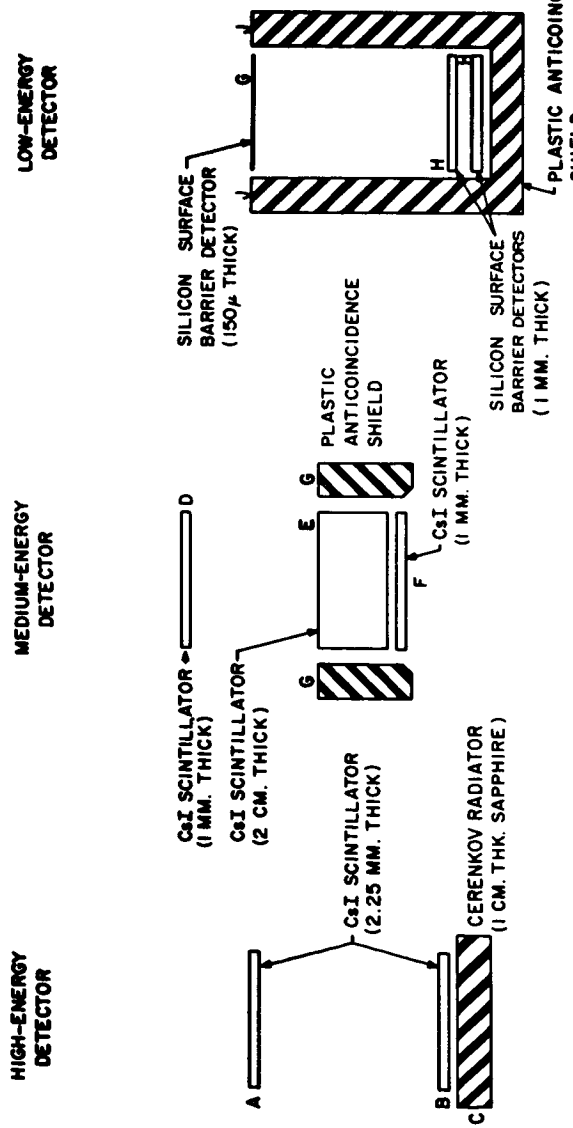
OGO 5 DETECTOR SYSTEM
HIGH-ENERGY DETECTOR
MEDIUM-ENERGY DETECTOR
LOW-ENERGY DETECTOR
CsI SCINTILLATOR (1 MM. THICK)
CsI SCINTILLATOR (2 CM. THICK)
CsI SCINTILLATOR (2.25 MM. THICK)
CERENKOV RADIATOR (1 CM. THK. SAPPHIRE)
PLASTIC ANTICOINCIDENCE SHIELD
CsI SCINTILLATOR (1 MM. THICK)
SILICON SURFACE BARRIER DETECTOR (150μ THICK)
SILICON SURFACE BARRIER DETECTORS (1 MM. THICK)
PLASTIC ANTICOINCIDENCE SHIELD
A
B
C
D
E
F
G
H

Figure 1

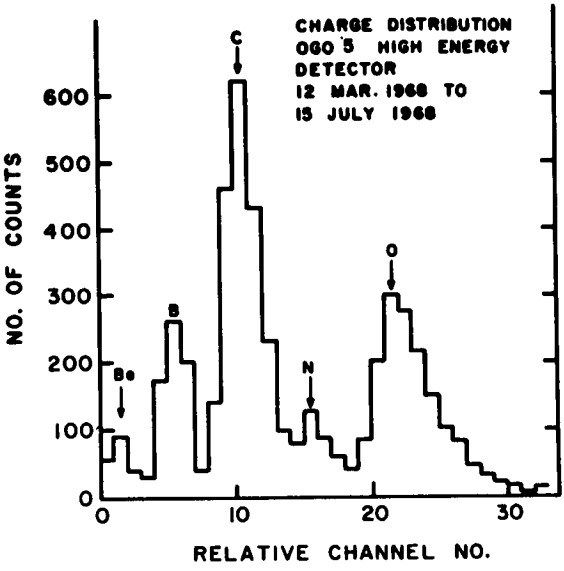
CHARGE DISTRIBUTION
OGO 5 HIGH ENERGY
DETECTOR
12 MAR. 1968 TO
15 JULY 1968
C
O
B
N
Be
NO. OF COUNTS
RELATIVE CHANNEL NO.

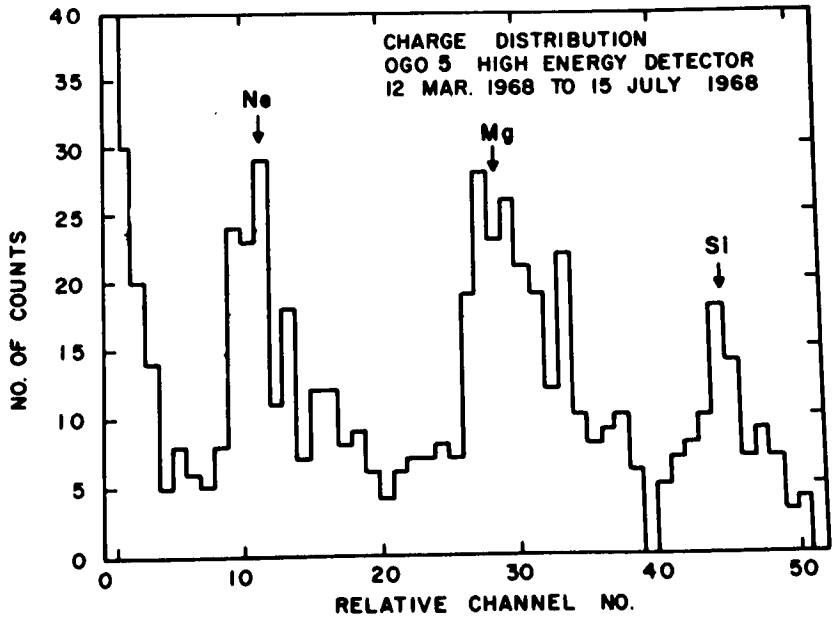
CHARGE DISTRIBUTION
OGO 5 HIGH ENERGY DETECTOR
12 MAR. 1968 TO 15 JULY 1968
Ne
Mg
Si
NO. OF COUNTS
RELATIVE CHANNEL NO.

Figure 2

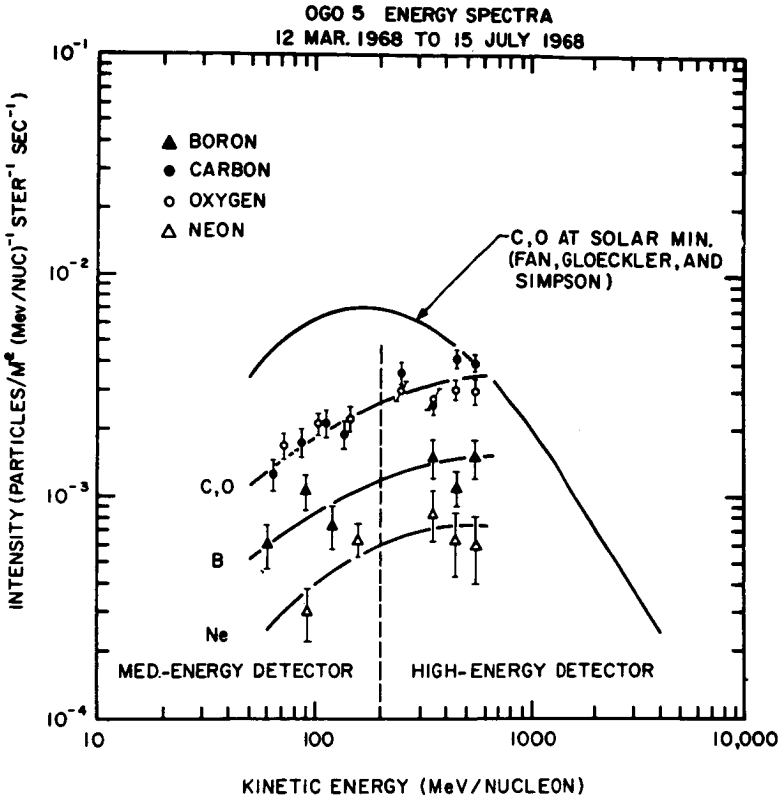
OGO 5 ENERGY SPECTRA
12 MAR. 1968 TO 15 JULY 1968
▲ BORON
● CARBON
o OXYGEN
△ NEON
C,O AT SOLAR MIN.
(FAN, GLOECKLER, AND
SIMPSON)
C,O
B
Ne
MED.-ENERGY DETECTOR
HIGH-ENERGY DETECTOR
INTENSITY (PARTICLES/M² (Mev/NUC)⁻¹ STER⁻¹ SEC⁻¹)
KINETIC ENERGY (MeV/NUCLEON)
10⁻¹
10⁻²
10⁻³
10⁻⁴
10
100
1000
10,000

Figure 3

CARBON 12 TO CARBON 13 RATIO IN THE INTERSTELLAR MEDIUM

Patrick Thaddeus

CHAIRMAN:

Our next speaker is concerned with the carbon 12 to carbon 13 ratio in the interstellar medium. Dr. Patrick Thaddeus will tell us about his measurement of this ratio.

DR. THADDEUS:

During the past year we have obtained a number of very high resolution stellar spectra with the Lick Observatory 120" telescope in order to obtain information on the short-wavelength spectrum of cosmic background radiation. The intensity of the background radiation (which lies in the millimeter and sub-millimeter region) is obtained from the ratio of intensities of the exceedingly faint interstellar lines of the molecules CN, CH, and CH^+. Most of these lines are in fact too weak to be detected in a single spectrogram, and we therefore resorted to a technique of plate synthesis in order to improve the signal-to-noise ratio.

With the increased sensitivity so obtained, which represents a new order of sensitivity in stellar spectroscopy, we have detected in the spectrum of the star ζ Ophiuchi, a second-magnitude star reasonably close to the galactic plane, a new interstellar line unrelated to the problem of background radiation, but of unusual interest in its own right. This new line lies just to the blue of the well-known interstellar line at 4232 Å due to $C^{12}H^+$, a chemically unstable but physically stable radical that is found in the interstellar medium. It is probably due to the isotopic species $C^{13}H^+$.

Figure 1 shows the observational data—the synthesis in a large digital computer of 25 spectra of Zeta Ophiuchi, each obtained at the very high dispersion of 1.3 Å per millimeter, and broadened to 5 millimeters in order to store a large amount of information on each plate. We have first traced the spectra on a densitometer, recorded the information on magnetic tape, and then on the computer numerically calibrated for the

nonlinear characteristics of the emulsion, and finally added the individual spectra together in order to increase the signal-to-noise ratio.

The original spectra cover the entire wavelength interval from 3650 to 4320 Å; but have so far been added together, as we see in Figure 1, only in the vicinity of the strongest lines of CN, CH^+, and CH. That is, we've only synthesized the spectra in a very narrow wavelength interval of a few Å about the lines that we were concerned about for the problem of background radiation.

Here in Figure 1 we have 4232 of CH^+, and right here beside it we have a small feature which can hardly be seen on this scale. Figure 2, however, shows this in greater detail.

This figure is a blow-up of the central part of the previous spectrum. Just to the left of the strong line, at exactly the expected isotope shift of .26 Å, is the weak feature attributed to $C^{13}H^+$. When it is subjected to the usual statistical significance tests, there is very little doubt that the feature is real. So from the intensities of the weak line and of the strong line, making a proper correction for the curve of growth of the interstellar lines, one determines in the line of sight the abundance ratio of $C^{12}H^+$ to $C^{13}H^+$. This is found to be $[C^{12}/C^{13}] = 82\ (+55, -15)$.

Presumably this is the ratio of the carbon isotopes, as well as the ratio of the molecular species. And although the measurement applies only to a single interstellar cloud, it most probably holds for the entire interstellar medium in the vicinity of the sun.

I might add parenthetically that this is the first interstellar isotope which is known with any precision. People for a long time have sought the deuterium to hydrogen ratio by looking for the radio hyperfine line of D. Barrett and Rogers at MIT a few years ago observed the λ-doublet of $O^{18}H$, and determined very approximately the O^{16}/O^{18} ratio. All they could show was that it was approximately terrestrial.

We can appreciate the importance of the ratio of the observed carbon isotopes when we compare it to the ratio of those observed on the earth, and in the atmospheres of certain stars. The terrestrial value is 89, and this is a value which we know from planetary and stellar spectroscopy to prevail on the sun and on Venus as well. It's therefore the value for the solar system.

Our observations thus at once suggest that the composition of the interstellar medium has remained quite stable, dynamically or statically,

during the five billion years since the solar system was formed. And in addition, in a small but important way, the measurement gives support to the concept of the cosmic abundance of the elements.

There is also the significant circumstance that in the CNO bi-cycle of nuclear burning the C^{12}/C^{13} ratio is determined directly by simple physics—that is, by the ratio of nuclear cross-sections which can be measured in the laboratory. It is expected to be about 4. In fact, it's been known now for over 30 years that a ratio of approximately this magnitude does prevail in the atmospheres of a whole class of cool carbon stars.

Thus our results suggest that these stars, although they may be losing mass, have contributed little to the overall composition of the interstellar material.

And thus in conclusion, it can be said that we have obtained a single, but very significant, piece of information relative to the exchange of matter between the interstellar medium and the stars.

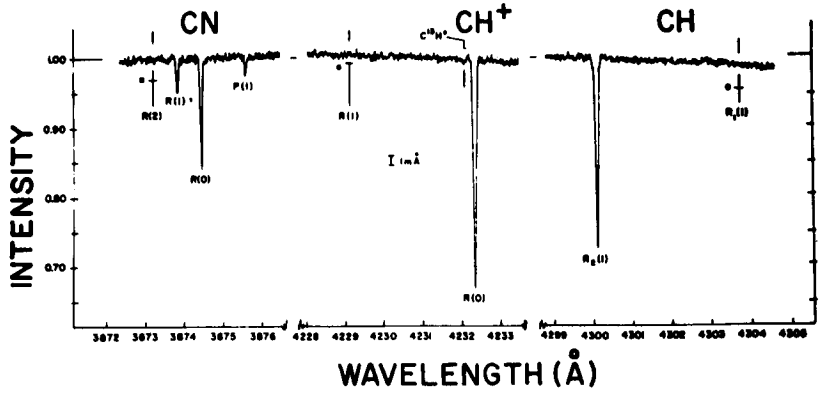

Figure 1

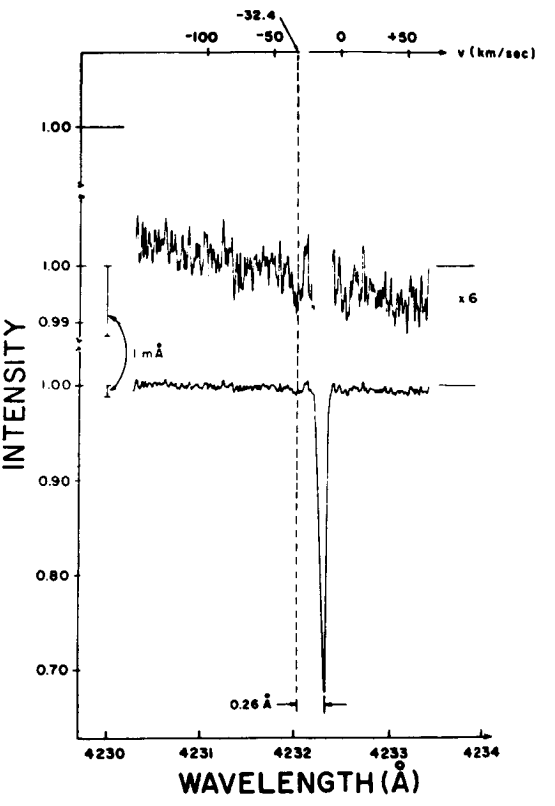
-32.4
-100
-50
0
+50
v (km/sec)
1.00
1.00
0.99
1.00
x 6
1 mÅ
INTENSITY
0.90
0.80
0.70
0.26 Å
4230
4231
4232
4233
4234
WAVELENGTH (Å)

Figure 2

PHOTOMETRY OF CEPHEID VARIABLES

Thomas N. Kelsall

CHAIRMAN:

We have now entered the realm of astronomy clearly, and our next speaker will continue in this region. His topic is the photometry of cepheid variable stars, and this is Mr. Thomas Kelsall.

MR. KELSALL:

The cepheid variables are physically pulsating variables with periods between 1.5 and 100 days. A salient feature of the cepheids is that they obey a period-luminosity relationship; that is, there is a reasonably strict linear correlation between the intrinsic magnitude of a cepheid and the log of its period. This relationship has made the cepheids useful as distance indicators, and delineators of galactic structure. They have also aided in the determination of an extragalactic distance scale, which is critical to the evaluation of the Hubble constant. They are most interesting stars.

There are two distinct classes of cepheids: Population I cepheids and Population II cepheids. While this pigeonholding is very rough, the basic distinction is that the Pop. I cepheids have a metal content – metals being all elements heavier than helium – of 1 to 4 percent by mass; but Pop. II cepheids have a metal content 1/10 to 1/1000 that of the Pop. I cepheids. To make full use of the period-luminosity relationship, it is essential to make this Pop. I and II segregation; but it is observationally very hard to distinguish between these two types in the period range 1.5 to 13 days. From my observations of the cepheids, in a particular photometric scheme, I have found a very nice way of segregating the metal-rich and the metal-poor cepheids.

One modus operandi for an astronomer is to use a photometric system which is a combination of a telescope, color filters, photomultiplier detector, and a standard observational procedure. In Figure 1, the filter characteristics are shown for three representative photometric systems. My observations were made in the Strömgren-Crawford composite system. In any photometric system the working quantities are the magnitudes, the colors (differences between

magnitudes), and color indices (differences between colors). For example, in the UBV system there are the ultraviolet (U), blue (B), and visual (V) magnitudes; the colors U–B and B–V; and the color index Q made up from the two colors. The working quantities in the three systems are shown in Figure 1. It is pertinent to point out that in the Strömgren-Crawford system the colors and color indices can be related to physical quantities such as the electron pressure, effective temperature, metal content, etc., of the star.

During a single pulsation of a cepheid, the variation of any particular color with time is approximately sinusoidal. Any two colors for the same star during a pulsational cycle will differ slightly in amplitude and phase. Beating a color against any other will create color-color Lissajous figures. Examples of these color-color Lissajous figures for two stars, in the various photometric systems, are illustrated in Figure 2. ST Tau is a Pop. II cepheid, while δ Cep is the classical example of a Pop. I cepheid. The geometric forms of the figures – open, and double- and triple-loop – illustrate the full multitude of possible shapes.

There are a number of things that can be discussed about these Lissajous figures, but let me just stress one thing: the total area enclosed by a Lissajous figure. Taking a purely phenomenological approach, we just measure these areas and then see what happens. The results are shown in Figure 3, where the total areas of selected color-color Lissajous figures, in the three photometric systems, are plotted as functions of the log of the cepheid periods. The crosses are the Pop. II (metal-poor), and the dots and triangles are the Pop. I (metal-rich), cepheids. We note that in both the 6-color and uvby;ABC systems there is the desired good discrimination of the two populations. This is not true in the more popular UBV system.

It is rather difficult to give even a qualitative reason for the discrimination. However, as I mentioned, in the uvby;ABC system the colors and color indices can be related to physical thermodynamic properties of the stars. It appears that for this system the color-color Lissajous figures are like thermodynamic work cycles, and thus the areas of the Lissajous figures are related to the work done during a pulsation; and this is different for the two populations.

In addition, I believe that the scatter in particular uvby;ABC Lissajous areas can be interpreted in terms of chemical compositional differences of the cepheids. If this is true, these areas will aid in the determination of the "chemical morphology" of the nearby regions of our galaxy.

COLOR SYSTEMS

UBV	6 - COLOR	STRÖMGREN - CRAWFORD
	FILTERS	
U - 3550 Å B - 4440 V - 5500	U - 3530 Å V - 4220 B - 4880 G - 5700 R - 7190 I - 10,300	u - 3450 Å v - 4110 b - 4700 y - 5500 A - 4375 B - 4275 C - 4160
	WORKING QUANTITIES	
U B V U-B U-V B-V $Q=[U-B]=(U-B)-0.90^{X}(B-V)$	U-V V-B B-G G-R R-I U-G V-G G-I	$c_1=(u-v)-(v-b)$ $m_1=(v-b)-(b-y)$ b-y G= B-A N= C-B

Figure 1

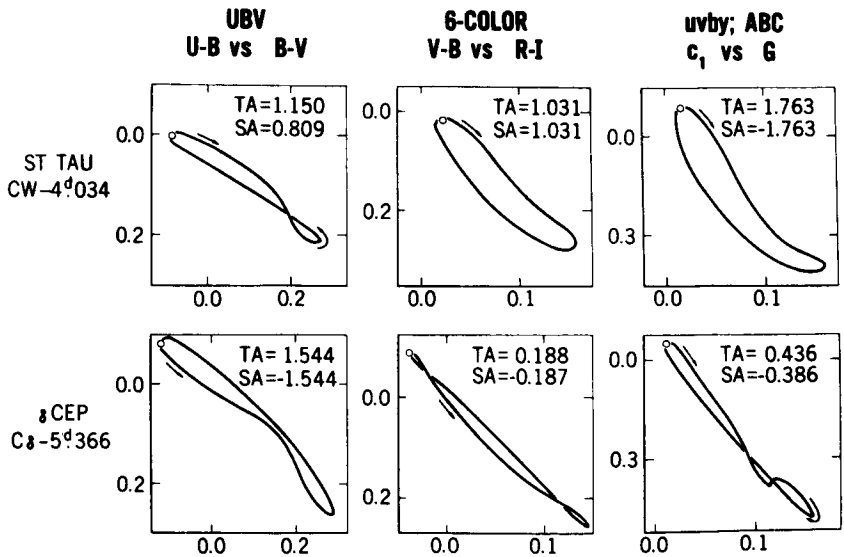

Figure 2

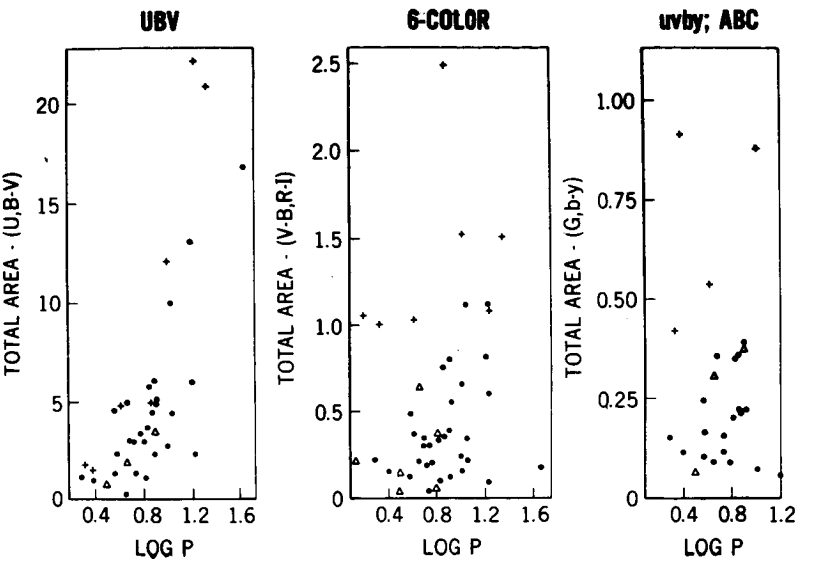
UBV
6-COLOR
uvby; ABC
TOTAL AREA - (U,B-V)
TOTAL AREA - (V-B,R-I)
TOTAL AREA - (G,b-y)
LOG P
LOG P
LOG P

Figure 3

THE ULTRAVIOLET SPECTRA OF ζ PUPPIS AND γ VELORUM

Theodore P. Stecher

CHAIRMAN:

We move now to the subject of ultraviolet observations. Our next speaker is Theodore Stecher. Mr. Stecher will tell us about ultraviolet stellar observations.

MR. STECHER:

Two stars have been observed in the rocket ultraviolet which are of interest to this symposium. They are ζ Puppis 05f and γ Velorum WC8. The observations were made from an Aerobee rocket. The payload consisted of a 13-inch f/10 telescope with an attached photoelectric spectral scanner with three exit slits. The resolution was 10 Å, and the wavelength interval scanned was from 1150 to 4000 Å. The results were telemetered to the ground, recorded on digital tape, and processed in a computer. The whole rocket with attached payload was pointed to the programmed stars with an accuracy of 10 to 20 seconds of arc, depending on the stellar magnitude. This was accomplished with a startracker and a gyroscopic inertial platform. The payload was parachuted to the ground and recovered in good condition. Two scans of 20 seconds' duration were made on each programmed star. On this flight four stars were observed, α Canis Majoris, ϵ Canis Majoris, ζ Puppis, and γ Velorum. The first two stars would appear to be interpretable in terms of standard atmospheric theory, and are the subject of another paper.

Figure 1 is the spectrum of ζ Puppis in the 1800 to 3100 Å range. The flux is in terms of ergs $cm^{-2}s^{-1}A^{-1} \times 10^{-9}$ at the top of the earth's atmosphere. This region is quite free of strong lines and therefore can be used to obtain an effective temperature by comparing its energy distribution to that of a model atmosphere. The problem is doing this is twofold: first, is the model sufficiently representative of the star to integrate over the unobserved energy, especially below the Lyman limit, and give a reasonable T_e? i.e., is the physics complete enough? and, second, what is the correction for interstellar extinction? Using continuous stellar models with no correction for interstellar extinction, the effective temperature is 28,000°K. This of course is incorrect. The

correction for extinction at 2000 Å is~5 times the B – V color excess (from my previous work). With the most probable color excess, the effective temperature is 40,000°K. The difference between a 40,000°K and a 50,000°K model at 2000 Å is only 0.1 magnitude when the models are normalized to the visual flux. This is because 2000 Å is still way out on the red end of the Planck curve at these temperatures. An error in the color excess of +0.02 mag could therefore result in a temperature of 50,000°K. An error of this size is a distinct probability. The color excess and temperature of ζ Puppis are important to our discussion here, since the 2000 Å region of γ Velorum appears to have the same energy distribution. If we assume that ζ Puppis and γ Velorum are physically associated in space, as has been suggested by several investigators, then the correction for interstellar extinction can be assumed to be the same and the effective temperature of the two stars is the same – 40.000°K.

In Figure 2 the short-wavelength region of ζ Puppis is shown. The remarkable thing to note is the P-Cygni type of profile in the resonant lines, C IV, Si IV, NV, C III, etc. The excitation in this star is sufficiently high that the N IV line at λ1718 is also in emission with a doppler-shifted absorption core. The level is 16 volts up and should be useful in determining the structure of the envelope. The wavelength shift between the emission peak and the blue-shifted absorption minimum in C IV is 18Å, which corresponds to a velocity of 3400 km/sec. or ~1 percent of the speed of light. While this is an upper limit and the real velocity is model-dependent, it will be large. The time constant on the amplifier was set to rise to $\frac{1}{e}$th of the true signal level over the scanning bandpass of 10 Å. When corrected for instrumental profile, the absorption line center should be quite black and indicates a large steady-state mass loss.

The absorption at λ1216 is due to interstellar hydrogen. The line is formed by radiation damping and can therefore be used to obtain the amount of neutral hydrogen between the earth and ζ Puppis. The small equivalent width–4 Å–indicated a low column density for neutral hydrogen, which is consistent with the small reddening correction in the visual region. Finally, one should note that in many respects the ultraviolet spectrum of this star is similar to that of a Wolf-Rayet star. In fact, most of the criteria for inclusion in the Wolf-Rayet phenomena discussed at this symposium would be met by this spectrum if we ignored the wavelength scale (which was not one of the criteria).

Having presented the "control star," let us proceed to Figure 3, which is the 1800 to 3100 Å scan of γ Velorum. The continuum is less obvious, but a reasonable estimate can still be made. In addition to the

Wolf-Rayet continuum, there is also the O star, and a small contribution from γ^1 Velorum. The lines of the O star are not noticeable, so it is reasonable to assume that most of the continuum is due to the Wolf-Rayet component itself. With these assumptions and the same correction for extinction we had for ζ Puppis, the effective temperature is 40,000°K. This is of course under the assumption that a hydrogen-helium atmosphere is applicable to this star. If a helium-carbon atmosphere should be the case, changes in the far ultraviolet could alter the temperature. A check against Hanbury-Brown's angular diameter, the observable flux, and the flux of the model at λ1900 produced good agreement.

The strong line at λ2296 is the strong permitted ^1D to $^1P0$ in the carbon III singlets. The even more intense line λ1909 is the intercombination line of carbon III. The intercombination line has an oscillator strength that is smaller by a factor of 1,000,000 than for the permitted line, and this poses an interesting question as to the formation processes of the two lines. Dr. West and I have been looking at this problem, and it appears that stimulated emission is necessary to produce the C III line. The required overpopulation of the triplets with respect to the singlets is most likely due to the dilute radiation field in the envelope and/or to mechanisms as yet unspecified. The result is Laser action.

The only other line clearly identified in the spectrum is due to C IV at λ2524. The atomic data for the high excitation present in these stars are far too incomplete to allow satisfactory identification of most of these lines. It should be remembered that the lines in the ultraviolet contain a considerable amount of energy. The continuum is many times more intense in the UV, and therefore for a line to show up it must be intense.

The far ultraviolet spectral scan of γ Velorum appears in Figure 4. It overlaps with the previous spectrum and again shows the λ2296 and λ1909 lines of carbon III. The Hα line of He II appears to be quite broad. The broad general absorption between λ1700 and λ1300 is due to molecular oxygen in the earth's atmosphere. There is sufficient information to correct it out and this is presently being done. The C IV line at λ1550 is in emission and absorption again, indicating an expanding envelope, although the velocity–1500 km/sec–is less than the velocity in ζ Puppis by a factor of 2. This is also evident in the other resonant lines, C II, Si IV, etc. Again there are a large number of lines belonging to the star that are unidentified.

There is one interesting possibility on unidentified lines that should be mentioned. This is the question of the physical reality of the quark. This mathematical particle, which has had such great success in SU3 theory, may or may not exist in nature. If quarks are physically real, they would presumably be produced through cosmic ray reactions in the interstellar medium, thermalize, and be present through the star formation process in younger stars. The quark of charge 1/3 would bind itself to C, N, and O at interior temperatures. The Wolf-Rayet stars offer the most likely possibility of detecting the quarks by observing the spectral lines due to carbon of charge 1-2/3, 2-2/3 and nitrogen of charge 1-2/3, 2-2/3, etc. The long path length through the envelope of the star, coupled with the probable overabundance of these elements, can greatly increase the current upper limit on these particles. Accurate theoretical wavelengths are needed for the quarked atoms, along with more complete multiplet tables.

Nitrogen V appears in absorption, and N IV is probably present in emission in γ Velorum. The lines are weaker than in ζ Puppis, but seem clear enough to add the presence of nitrogen to a carbon Wolf-Rayet star. A number of interstellar lines appear in the spectra of both stars: C II, Si II, Al II, O I, Fe II, Cr II, etc. There is also the possibility of the autoionization of Al I and Ca I. The hydrogen Lyman-α equivalent of γ Velorum is similar to that of ζ Puppis, indicating a low column density of neutral hydrogen and implying the correctness of the interstellar extinction correction.

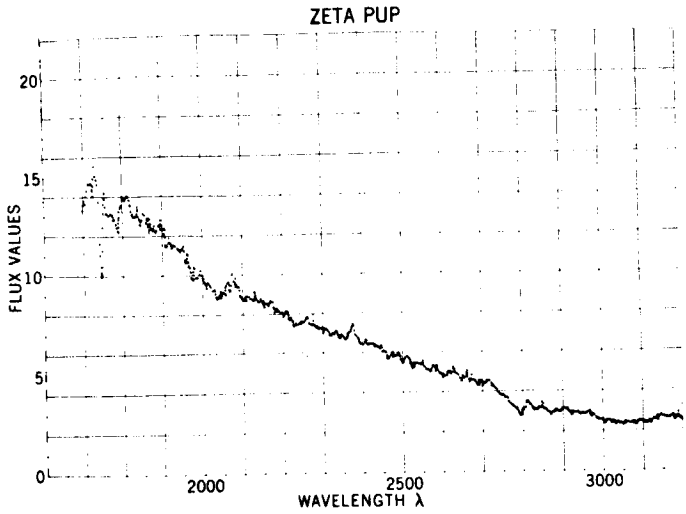

Figure 1

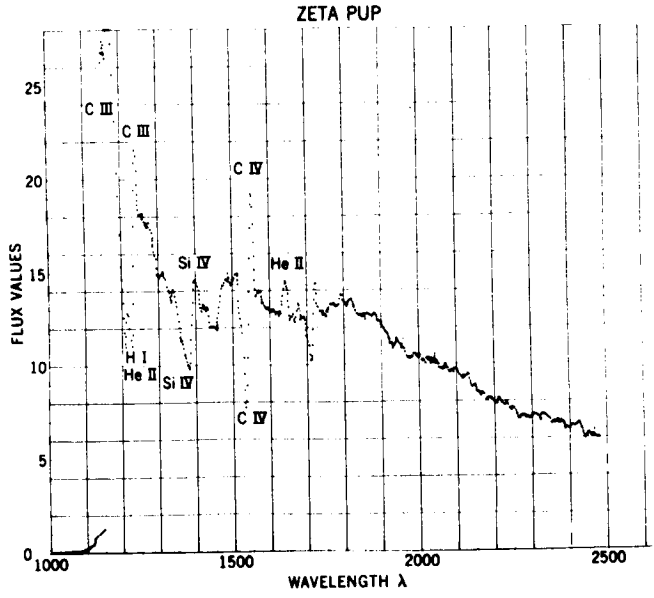

Figure 2

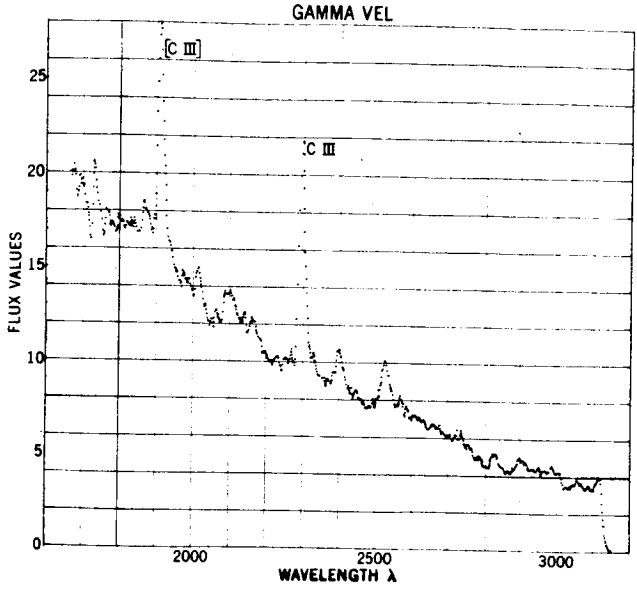

Figure 3

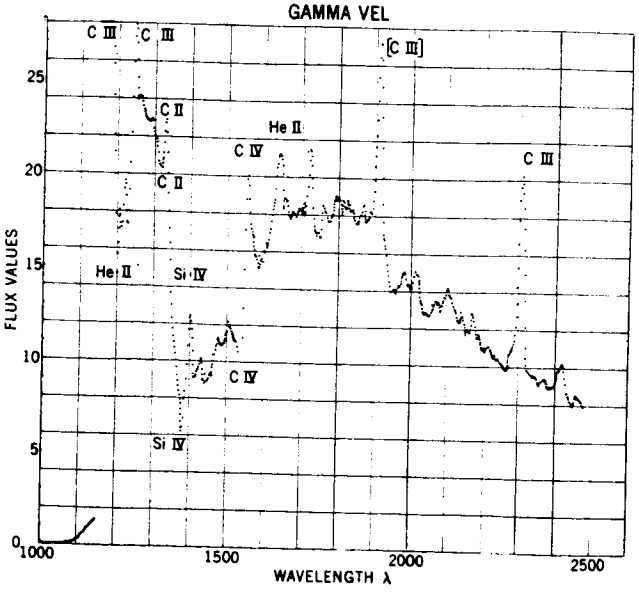

Figure 4

FAR ULTRAVIOLET PHOTOMETRIC OBSERVATION OF INTENSE EXTRATERRESTRIAL SOURCES

Donald F. Heath

CHAIRMAN:

We have now fully entered the region of ultraviolet observations, and our next speaker will continue in this area by telling us about far ultraviolet photometric observation of intense extraterrestrial sources. This is Dr. Donald Heath.

DR. HEATH:

A far ultraviolet polarization analyzer filter photometer for measuring the intensity and polarization of Lyman alpha in the night airglow was launched from Wallops Island near local midnight on January 21, 1968, aboard a Nike Tomahawk, and reached an apogee of 296 kilometers. The polarization filter photometer, with a 6° field, scanned the sky at 9/10 of one rps perpendicular to the spin axis. The spin axis precessed on a 60° cone with a period of 150 seconds. The upper section of the cone was in the direction of the zenith, and the lower section was in the direction of north.

Under the conditions where the emitting wavelengths are known and the intensity increases as one goes to shorter wavelengths, one can use subtractive filter techniques to great advantage. A lithium fluoride polarization analyzer in front of the Geneva-action filter wheel and a 542 G photomultiplier turned through 720° for each of the four filter positions of the wheel. These were: open, calcium fluoride, sapphire, and a blank, for a total cycle time of 8 seconds.

Figure 1 shows a section of the telemetry record where the photometer recorded an intense UV source in Canis Major. Channel C, with the sapphire filter in, has a peak sensitivity at 1,500 Å and equivalent width of 200 Å. Channel B, with calcium fluoride inserted, has, after subtracting channel C, an equivalent width of 190 Å and a peak sensitivity at 1,350 Å. And, finally, Channel A, which is open, with only the polarization analyzer in front of it, after subtracting channels B and C has an equivalent width of 90 Å and a peak sensitivity at 1,210 Å.

A range-switching linear electrometer covered four decades of signals. In the telemetry record in Figure 1 can be seen several effects. There is horizon brightening in the north in Channels B and C, which also carries over into Channel A. The solar zenith angle was 164°. In the southern section of the sky there is no horizon brightening observed. We have this intense source in Canis Major which was observed in all telemetry records.

And, finally, we have the ultraviolet albedo of the earth measured at Lyman alpha. The albedo increased gradually until it reached a maximum of .50 at 296 kilometers. The center of the earth-directed Lyman alpha signal minimum in conjunction with the magnetometer data was used to determine the aspect solution of the photometer.

Figure 2 shows the coverage of the celestial sphere. The locations of the UV sources observed in this flight are indicated by the squares, and the shading indicates the approximate size. The circles represent the sources which were reported by Kupperian, Boggess, and Milligan in 1958, which generally have not been accepted as being real. The lower arc represents the lower horizon, while the upper arc represents the upper limits of the coverage of the photometer as it swept across the celestial sphere.

All of the five UV sources were observed in all three filter positions at least once and sometimes twice in an 8-second interval, and also at 150 seconds; and one observation was also made again at 300 seconds. This is indicated by the type of cross-hatching. The sources all emit more flux than the brightest UV stars, such as ϵ Canis Majoris, ζ Puppis, and γ Velorum. Typically the source in Canis Major emits ten times more flux in the vicinity of Lyman alpha and five times more flux at 1,350 and 1,500 Å than the brightest UV stars. The diffuse source observed in Canes Venatici was brightest at 1,350 and 1,500 Å with essentially nothing at Lyman alpha. The source in Sextons, just south of Leo, about 9° in diameter, and the source in Canis Major were essentially identical in size and as to the types of output. Two smaller sources, about 3° in diameter, one in Caelum and the other in Pisces, are about twice as bright in the vicinity of Lyman alpha as are the aforementioned two sources.

There is always a question of a calibration error, and I think that this can be ruled out because the measured nighttime Lyman alpha night glow signal at 296 kilometers was 3.5 kilorayleighs which is a reasonable value for this part of the solar cycle. The source in Canis Major correlates very well with an H alpha nebula reported by Abt, Morgan, and Stromgren in 1957.

At the moment I don't have any explanation as to why we did not see the previously reported intense source in Orion except that we may not have complete coverage of the sky. Also I did not observe the very broad diffuse source reported by Kupperian, Boggess, and Milligan in the Vela-Puppis region.

CHAIRMAN:

Is there a question or comment on this perhaps startling observation? Yes?

MEMBER OF AUDIENCE:

Did you observe any stars with your instrumentation?

DR. HEATH:

The star signals would have been just down in the noise level. There are some signals, but few are very sharp; and I haven't really gone back and tried to identify those yet.

MEMBER OF AUDIENCE:

What sort of angular diameter are you talking about?

DR. HEATH:

These were of the order of the geometrical field of view, which was 6°. There is a possible source of error here, but they appear to be comparable to the angular field of the instrument.

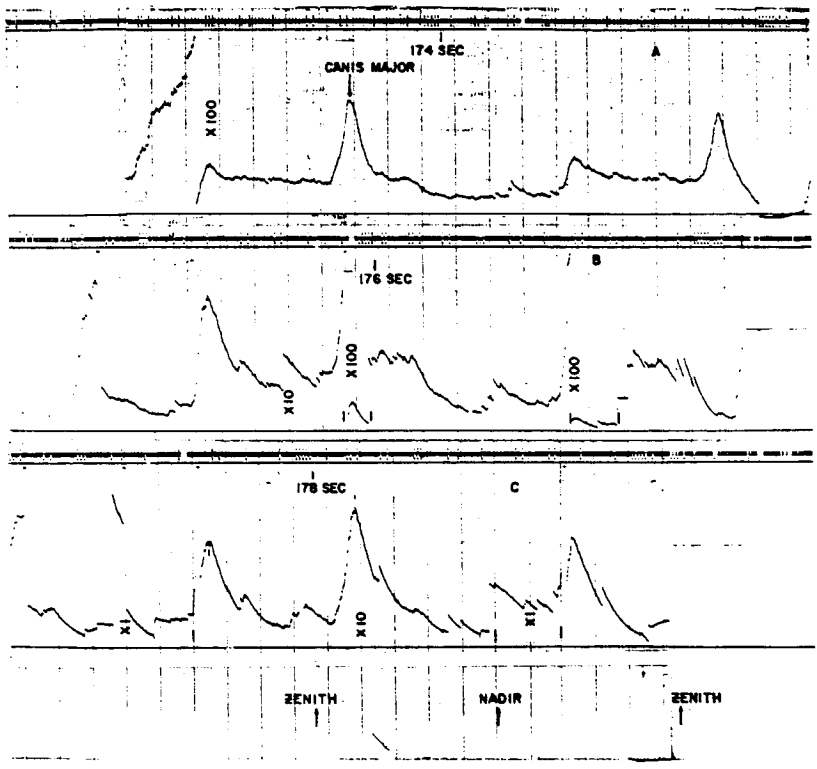
174 SEC
CANIS MAJOR
A
X100
176 SEC
B
X10
X100
X100
178 SEC
C
X1
X10
X1
ZENITH
NADIR
ZENITH

Figure 1

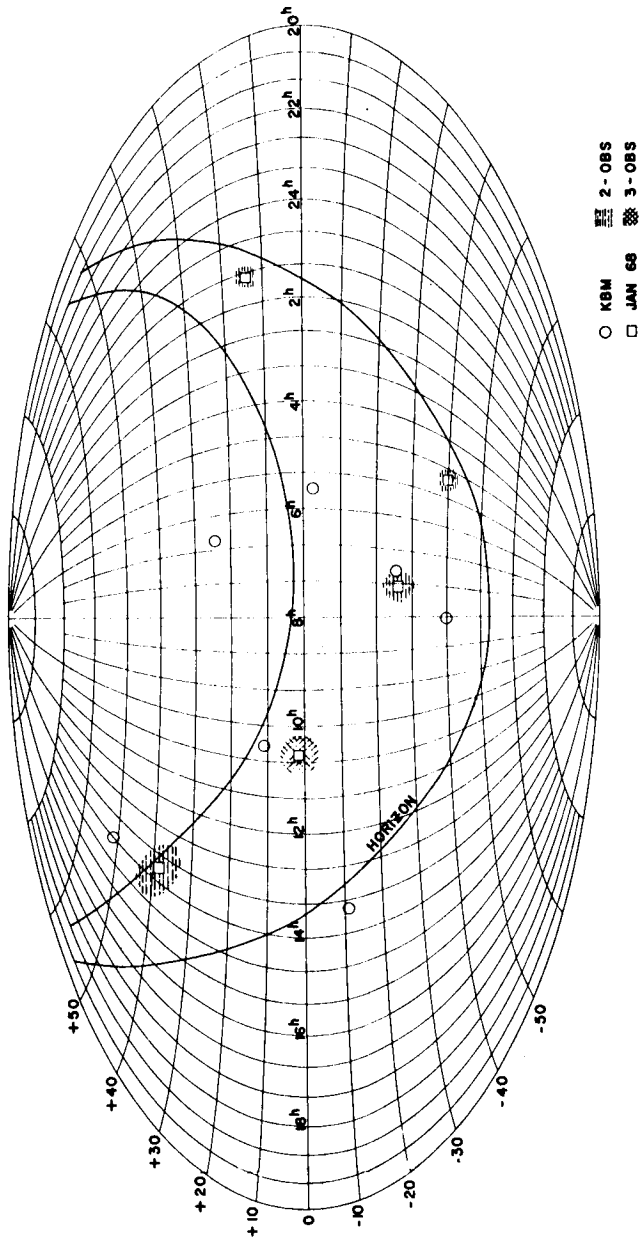

Figure 2

RED SUPERGIANTS

Richard B. Stothers

CHAIRMAN:

The next speaker on our program is Dr. Richard Stothers, and his topic is red supergiants.

DR. STOTHERS:

One of the interesting applications of the study of stellar structure and evolution is the potential verification of basic physical laws and hypotheses. This can be done by comparing observational data with theoretical models based on these laws and hypotheses. The present paper is concerned with the life history of very massive stars and certain hypothetical neutrino processes which occur during the very advanced phases of evolution. First, however, it is necessary to trace briefly the preceding phases of evolution.

When a new star condenses out of the interstellar gas and dust, half of its released gravitational energy heats up its interior, and half is radiated away into space. When the central temperature becomes hot enough to cause two protons to fuse, nuclear reactions replace gravitational contraction as the source of stellar energy. Figure 1 shows the locus of hydrogen-burning stars on a plot of luminosity against surface temperature (or color). Ultimately, hydrogen fusion reactions result in the formation of helium in the stellar core. After the exhaustion of hydrogen at the center, the core begins again to contract until helium ignites. The star is then called a red supergiant because its observed surface is very cool and extended. As helium burns into carbon, the star's surface quickly shrinks and becomes hotter and yellower, eventually giving rise to the configuration known as a blue supergiant. After helium exhaustion at the center, the core recontracts while the surface expands, and the star becomes a red supergiant again. It will remain a red supergiant until it explodes at the end of its active lifetime, in a supernova event.

During the second red-supergiant phase, the star burns carbon, neon, oxygen, and silicon successively in its core until iron is formed. The lifetime of this phase depends critically on whether or not the star emits

energy in the form of neutrinos as well as electromagnetic radiation. If so, the increased energy losses can shorten the lifetime by a factor of at least 10. The processes which give rise to neutrino emission depend on a direct interaction between electrons and neutrinos, as provided by a theory of the universal Fermi interaction due to Feynman and Gell-Mann. These processes are:

$$\gamma + e^- \rightarrow e^- + \nu + \bar{\nu} \ ,$$

$$e^- + e^+ \rightarrow \nu + \bar{\nu} \ .$$

They cannot be observed in a terrestrial laboratory, because of the smallness of the predicted interaction cross-sections. However, the stars with their high-temperature conditions during carbon burning and later phases provide an ideal cosmic laboratory.

The astronomical effects of neutrino emission have to be detected indirectly, because of the insignificant interaction of neutrinos with matter. Once formed inside stars, neutrinos immediately escape. It is therefore necessary to detect their presence through their influence on the evolutionary lifetime. This will be reflected observationally in the relative numbers of stars of nearly the same mass in different evolutionary phases, e.g.,

$$\frac{N_1}{N_2} = \frac{\tau_1}{\tau_2} \ .$$

Since one can calculate τ_1 and τ_2 from theoretical stellar models, it is possible to predict N_1/N_2 theoretically and to compare this ratio with the observed ratio of stars in space.

Clearly, the red supergiants are the crucial stellar group to test the neutrino hypothesis. Since their population is "contaminated" by a number of stars burning helium, we have found it necessary to consider only the most massive stars (20-60 $M_\odot$), in which helium burning occurs mainly in the blue-supergiant configuration.

The results of our comparison are shown in Table 1, where the numbers given as limits take into account the maximum uncertainty in both the theory and the observations. In the first test, the observed number of red supergiants is three; whereas, on the basis of theoretical models which do not include the neutrino processes, at least nine red supergiants should be observed. In the second test, carbon stars (which are

presumed to be red supergiants, although some blue stars with carbon-rich surfaces may also exist in nature) are totally lacking in our sample; however, at least three carbon stars should be present if neutrino emission does not occur. Finally, the third test, using the numbers of yellow supergiants, should be considered more a corroboration than a test because of the small predicted difference in the numbers of stars with and without neutrino emission.

The foregoing results certainly indicate that an evolutionary accelerating mechanism is occurring inside the red supergiants. The only presently known or postulated mechanism is neutrino emission. If our present suspicions are correct, the neutrino processes must be operating in at least the strength suggested by current theory. Thus, astronomical observations, interpreted with the help of stellar models, provide rather good evidence for the existence of a direct electron-neutrino interaction in nature.

STATISTICS OF SUPERGIANTS OF HIGH MASS

OBJECT	OBSERVED NUMBER	EXPECTED NUMBER		OBSERVED NUMBER OF COMPARISON OBJECTS
		ν	no ν	
red supergiants	3	>1	>9	13 blue supergiants
carbon stars	0	0	>3	50 blue supergiants
yellow supergiants	3	3	5	58 blue and red supergiants

Table 1

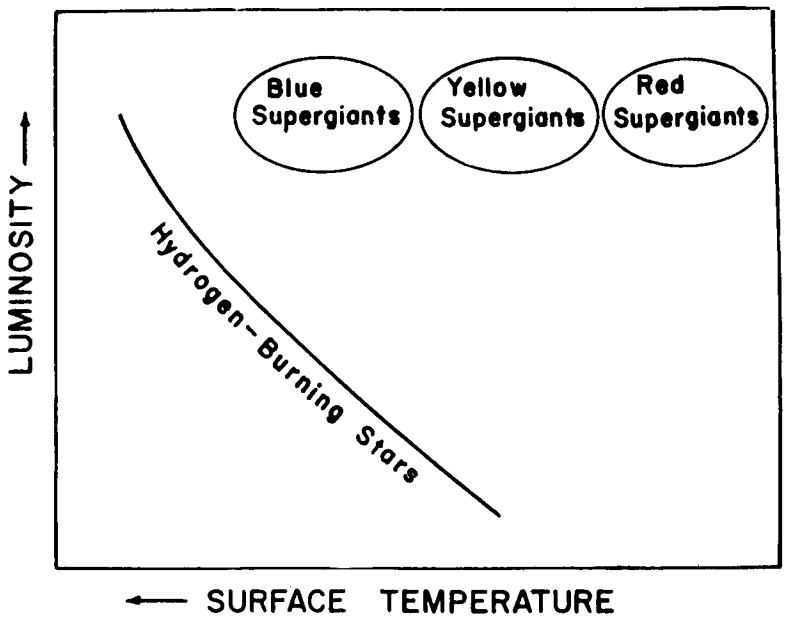
Blue Supergiants
Yellow Supergiants
Red Supergiants
Hydrogen-Burning Stars
LUMINOSITY
SURFACE TEMPERATURE

Figure 1

LONG-WAVELENGTH RADIO ASTRONOMY OF THE GALAXY

Robert G. Stone

CHAIRMAN:

Our next subject moves to the range of radio astronomy. Dr. Robert Stone will discuss long-wavelength radio astronomy of the galaxy.

DR. STONE:

Because the terrestrial ionosphere absorbs, refracts, and reflects incoming radio signals from celestial sources, ground-based observations of radio signals below 10 MHz are possible only under very extreme conditions and then subject to very large uncertainties.

By the time one proceeds down to a few MHz, ground-based observations are useless. For this reason, the RAE satellite, with its two 750-foot-long antennas, represents the first successful attempt from space to study the spectral and spatial distribution of radio signals from celestial sources at these low frequencies.

In addition to the study of a rather fascinating and wide range of dynamic processes occurring within our solar system, one of the primary goals of RAE is to study the spectral and spatial distribution of cosmic noise from our own galactic system.

In Figure 1 is shown a rather simplified model of the galaxy. On the left, a bird's-eye view, we show the sun situated about halfway out in the spiral structure. And on the right, a side view, the sun is shown in the Orion arm. We have three major components: an isotropic component which represents the sum total emission from extragalactic sources; a halo which is part of our galactic system and is a region of synchrotron emission generated by very high energy electrons in weak magnetic fields; and a disk component which contains not only synchrotron regions but also ionized hydrogen.

Now, during the early days of the RAE experiment, the orbit was selected so that the antennas would scan perpendicular to the galactic plane and therefore we would be able to study the galactic center, the

galactic pole direction, and the anticenter, because these are very important quantities to compare in a model. Notice also that as the angle b, galactic latitude, changes we look through more of a halo toward the center and less toward the anticenter.

During the early days of space radio astronomy, all observations were obtained with short electrical dipoles, antennas which are essentially non-directive. In Figure 2 we show such observations. In this case one can obtain only an integrated spectrum. We are not quite sure where the emission comes from, but we can get some general idea of the spectral behavior. This happens to be an extragalactic and disk model which has been fitted to the sum total of observations below 10 MHz. In particular one notes that the spectrum turns down below a few MHz, because of absorption of the intense synchrotron emission in ionized hydrogen regions.

Since this absorption is a function of the electron density and kinetic temperature of the ionized hydrogen regions, as well as path length and frequency, we can, with a suitable model, derive some properties of the medium. For example, in the particular model we have used here, assuming all the absorption occurs within the galactic disc of semi-thickness several hundred parsecs and electron kinetic temperature 10,000°K, we derive a mean electron density of the order of .01 electron per cubic centimeter for the disk.

However, to proceed further than this, one needs to study the distribution in space. I would point out that, since the optical depth does vary inversely as the square of frequency and is a function of path length also, we have a unique opportunity at long radio wavelengths to study the distribution in depth. In other words, we have a depth scale.

In Figure 3 are seen some of the first scans we have obtained with RAE during the first two weeks of its operation. The antennas, I would point out, are still at 450 feet. Also, these are two of the lowest frequencies. We do go up to about 9 MHz.

The resolution is of the order of 1 steradian at these frequencies and this antenna length, and is adequate to show a systematic variation in intensity as one proceeds from the galactic center through the galactic pole to the anticenter, the variation being about 1.5 to 1 at 700 kHz and about 2 to 1 at 2200 kHz.

Next to the observations we have for comparison a simple model involving a disk, halo, and extragalactic component. The agreement is poor towards the galactic center because the model has not taken into account the finite antenna beamwidth. Nevertheless, there is qualitative agreement between the model and experiment away from the galactic center.

We feel that further analysis will enable us to shed some light on the nature and existence of the radio halo and certainly will give us some further insight on the distribution of the ionized component of our galaxy.

CHAIRMAN:

The results which Dr. Stone has presented now and which Mr. Alexander presented earlier, this morning, are the first from the radio astronomy satellite. And we are particularly pleased to have them presented here.

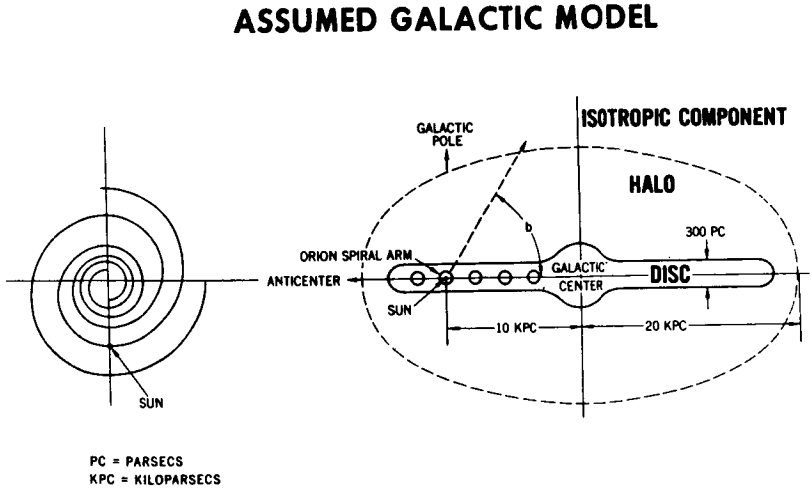

Figure 1

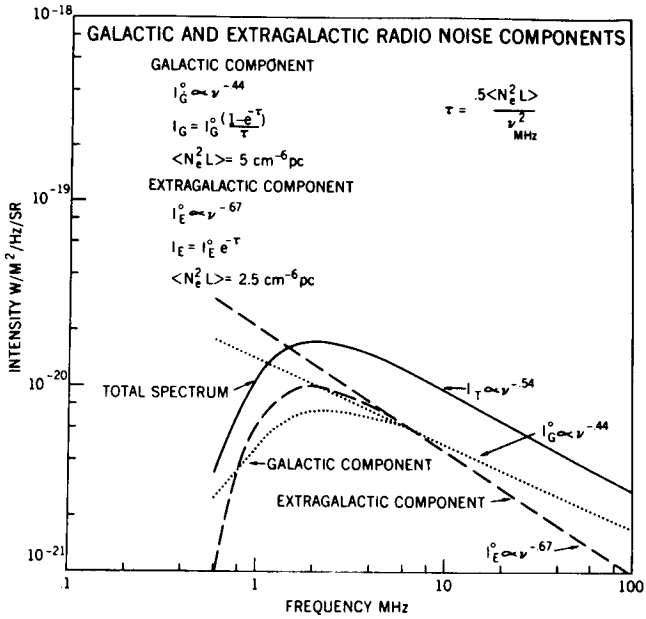

Figure 2

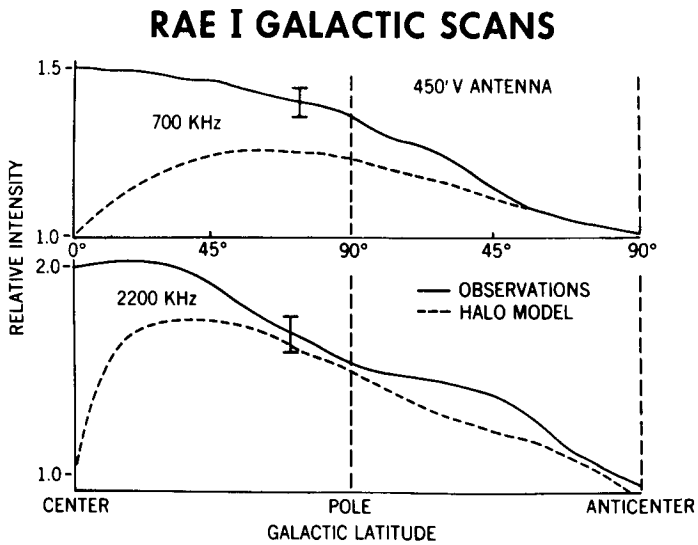

Figure 3

DETECTION OF THE GALACTIC CENTER AT 100 MICRONS

William F. Hoffmann

CHAIRMAN:

Our next speaker will also be concerned with a "first," since he is the one who has made the first measurement of the galactic center in the far infrared region. This is Dr. William Hoffmann, and he will tell us about that measurement.

DR. HOFFMANN:

Last summer the Goddard Institute's balloon-borne far-infrared telescope detected an intense source at a wavelength of 100 microns from the direction of the galactic center. I believe this to be the first object outside the solar system which has been detected in this region of the spectrum.

Figure 1 shows the direction of the source in galactic coordinates. I have shown the galactic plane as a broken line. The galactic center is in the southern sky at minus 29 degrees declination. The object we detected is clearly not a point source. It appears to be extended along the galactic plane at least 6.5 degrees, the extent of the region which we scanned during the flight, and across the galactic plane approximately 2 degrees. The position of the object was determined to be about 3 degrees from the galactic plane. This apparent displacement is within the uncertainty of the determination.

This remarkable agreement of the direction and alignment of the object with the direction and alignment of the galactic plane gives strong evidence that in fact we are seeing the galaxy at a wavelength of 100 microns. The radiation appears to be coming from the central portion of the galaxy, a disk about 1000 parsecs in diameter at a distance of 10,000 parsecs from the solar system. If this is so, the intensity we observed indicates an emission from this region of 3×10^{42} ergs per second in the wavelength range from 80 microns to 120 microns. This is 700 million solar luminosities, and it is equal in radiation flux to the total output of all the stars in that region of the galaxy.

What this means in terms of the whole galaxy is shown in Figure 2. I have plotted, as a function of wavelength, the galactic luminosity by giving the monochromatic luminosity L_ν times the frequency ν, so that this graph can be read directly in watts. The newly measured point at 100 microns is 10^{37} watts. It cannot be explained either in terms of direct starlight emission, which occurs mainly in the visual and near infrared, or in terms of the radio background reported about in a previous paper.

The most remarkable feature of this graph in fact is that the total galactic output at 100 microns, given some reasonable spectral distribution, appears to be equal to or even greater than the previously known galactic radiation at all wavelengths.

A possible mechanism for this radiation is interstellar solid material in the form of small particles which absorv energy in the form of starlight, are heated by it, and re-emit this energy in the far infrared. The broken curve indicates the spectrum one might expect from such grains heated to 30°K.

If in fact we have detected emission from interstellar dust grains, there are two important implications about the composition of the grains. First, in this same study we determined the temperature of the source to be at least 16°K. It could be 30°, as shown in Figure 2, or even somewhat higher. There has been proposed recently a model of interstellar grains composed of graphite particles surrounded by a solid hydrogen mantle. However, under the conditions of interstellar space, solid hydrogen sublimates at 4°K. Thus the 17°K lower limit on the temperature seems to rule out this once promising hypothesis of solid hydrogen on the grains. The second interesting implication comes from something we would like to do in the future. The composition of the grains is extremely interesting in terms of stellar formation, since the initial composition of stars and planets should be determined by the composition of the interstellar material. We hope that by further measurements in neighboring spectral regions we might be able to determine clues as to what the interstellar dust grains are composed of.

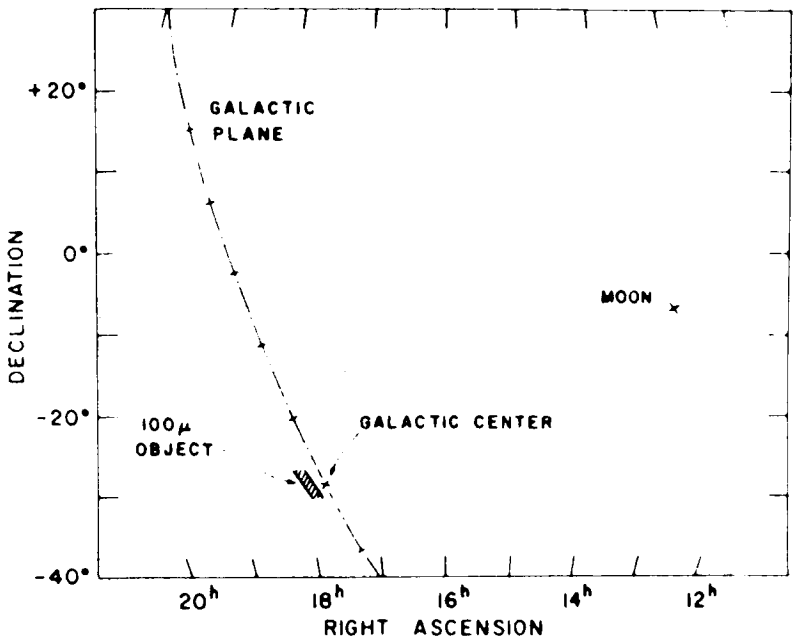

Figure 1

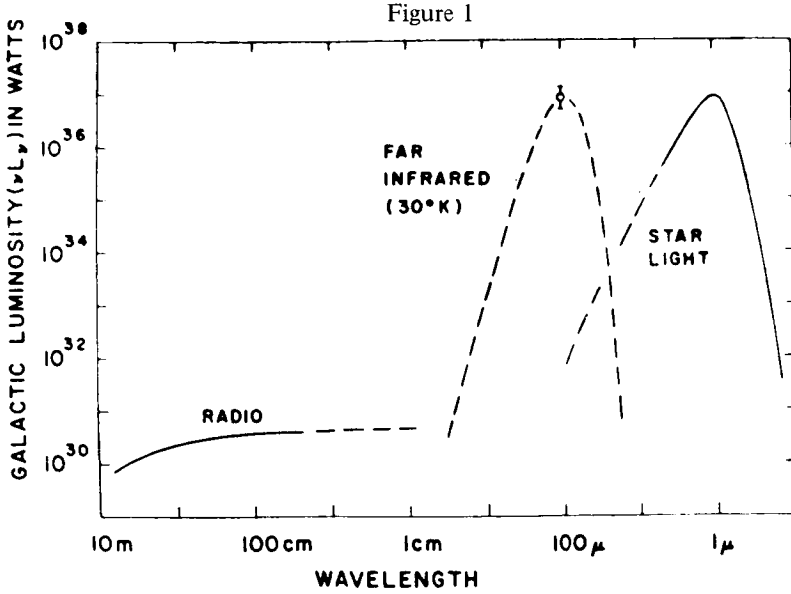

Figure 2

COSMOLOGICAL SIGNIFICANCE OF ISOTROPIC 1-100 MEV GAMMA RADIATION

Floyd W. Stecker

CHAIRMAN:

The final section of our program this afternoon is concerned with gamma-ray astronomy, and the first speaker in this area will be Dr. Floyd Stecker, whose talk is on the cosmological significance of isotropic 1 to 100 Mev gamma radiation. Dr. Stecker.

DR. STECKER:

Studies of the red-shifts of distant galaxies as well as recent X-ray indications of a hot ionized gas in intergalactic space and studies of the gravitational configurations of clusters of galaxies have indicated that as much as 99 percent of the matter in our universe may be spread throughout intergalactic space with a mean density of about one atom for every three cubic feet.

It has also been found that the entire universe is bathed in a primordial radiation field.

For these reasons, I propose that the entire intergalactic medium may be used as an enormous cosmic-ray detector having a radial dimension of 10 billion light years.

This is because cosmic rays traveling through the gas and through the primordial radiation field undergo various interactions, converting some of their energy into gamma-ray energy.

In order to use this cosmic detector, we must calibrate it by making detailed determinations of the proper gamma-ray spectra to expect from the various interactions.

In Figure 1, I list the various interactions which can occur in this intergalactic medium.

Firstly, we may have Compton collisions, which are collisions between high-energy electrons and photons of the universal radiation

field. In these collisions the electrons collide with the photons and impart some of their energy to the photons, boosting the photon energy up into the gamma-ray energy region.

Secondly, we may have bremsstrahlung, which is the electromagnetic radiation given off by cosmic-ray electrons as they pass through the electromagnetic field of atoms of the intergalactic gas and are therefore decelerated.

The third process is inelastic strong interactions which involve the production of subatomic neutral pi-mesons which then decay to produce gamma rays.

A fourth possible process may be matter-antimatter annihilation on the boundary regions of intergalactic matter and antimatter gases. Matter and antimatter nucleons annihilate into mesons, some of which decay into gamma rays.

Because of the universal expansion, gamma rays produced early in the history of the universe will be distinguished by the fact that they are red-shifted to lower energies. Therefore, in theory we can read the whole history of the universe in terms of the gamma-ray spectrum.

I have done detailed calculations of the gamma-ray spectra to be expected from these various high-energy interactions, taking into account the red-shifts, the curvature of the universe, and the expansion of the universe, with the resultant density changes affecting the interaction rate.

In Figure 2, we see the various types of gamma-ray energy spectra that one obtains from these calculations along with the present observations.

Observations below 1 Mev have indicated the power law spectrum (shown in Figure 2 on a logarithmic plot) which may be due to any of the alternative mechanisms of annihilation, bremsstrahlung, or Compton collisions. However, observations above 1 Mev, as evidenced by recent satellite data by Dr. Vette here and Dr. Peterson at the University of California and also the OSO 3 measurements of Clark, Garmire, and Kraushaar, will not fit on any of the first three curves but fall nicely on the curve produced by inelastic high-energy interactions with a maximum red-shift of 100.

Under this interpretation of the gamma-ray observations above 1 Mev, we find the following conclusions. Firstly, this may be the first

evidence indicating the existence of a flux of extragalactic cosmic rays between the galaxies with a present intensity about four orders of magnitude below the galactic cosmic-ray intensity.

Secondly, with the age of the universe being about 10 billion years, we find that these cosmic rays started being produced at about 10 to 100 million years after the initial expansion; this also being the first evidence of any such cosmological time element.

Thirdly, we find that cosmic-ray production in intergalactic space was larger at earlier epochs, that is, at high red-shifts. And this is an additional link in our chain of evidence against the steady-state theory.

CHAIRMAN:

Question?

MEMBER OF AUDIENCE:

(Inaudible.)

DR. STECKER:

Well, of course the Compton mechanism can give you the proper power law below 1 Mev. However, there are difficulties in this interpretation. The electrons which produce the Compton X-rays are being depleted by the same Compton process and therefore one needs a very large energy input of high-energy electrons. This trouble is avoided by the bremsstrahlung explanation. And there is also the possible alternative of matter-antimatter annihilation giving you the right power law. And the interesting fact about this is that this power-law index comes purely out of the cosmology and not out of ad hoc assumptions about the spectral index of the cosmic-ray electrons.

CHAIRMAN:

Yes, Dr. Shapiro?

DR. MAURICE SHAPIRO:

When you said that this could be the first evidence for the presence of an extragalactic cosmic-ray flux, would you not agree that one should qualify that by saying "for the presence of cosmic rays having energies below about 10^{16} electron volts"—namely, the upper limit at which cosmic rays can be trapped in the galaxy?

DR. STECKER:

Yes. That is correct. There is some indication from the spectrum of ultrahigh-energy cosmic rays above 10^{16} electron volts that we are observing on extragalactic component. And, interestingly enough, it is about the same order of magnitude as one would get from the interpretation presented here.

DR. SHAPIRO:

One perhaps could also draw an important conclusion from your conclusions, if they are right, namely, the quantitative figure of a flux down by 10^{-4} from the flux inside the galaxy would imply that people like Burbidge and Hoyle who are trying to sell us an extragalactic origin theory for essentially all cosmic rays would then not very likely be right.

DR. STECKER:

Yes. That is correct. As a matter of fact, the OSO 3 data alone, even if taken as an upper limit, would rule out the hypothesis of a universal cosmic-ray flux with the same intensity as that observed at the earth.

EXTRAGALACTIC GAMMA-RAY PRODUCTION

PROCESS	WHAT'S COLLIDING WITH WHAT	
COMPTON COLLISIONS	COSMIC-RAY ELECTRONS	UNIVERSAL PHOTONS
BREMSSTRAHLUNG (COLLISIONAL ELECTROMAGNETIC RADIATION)	COSMIC-RAY ELECTRONS	INTERGALACTIC GAS
INELASTIC STRONG INTERACTIONS	COSMIC-RAY PROTONS	INTERGALACTIC GAS
ANNIHILATION	INTERGALACTIC MATTER	INTERGALACTIC ANTIMATTER

Figure 1

EXTRAGALACTIC HIGH-ENERGY PHOTON SPECTRA

OBSERVATIONS:

△, ◊ RANGER 3 (METZGER, ET AL.)

• ERS 18 (PETERSON, ET AL.)

OSO 3 (CLARK, ET AL.)

THEORETICAL PREDICTIONS:

A – ANNIHILATION OF ANTIMATTER

B – BREMSSTRAHLUNG

C – COMPTON COLLISIONS

P – COSMIC-RAY INELASTIC P-P COLLISIONS (Z_{MAX} = 100)

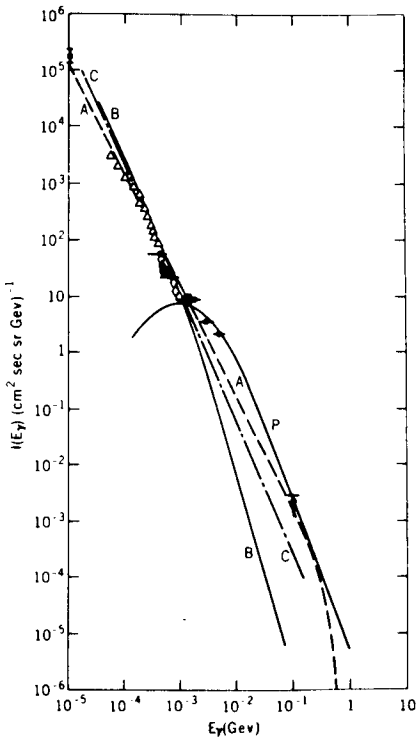

Figure 2

INTERPRETATION OF 0.1 TO 10 MEV GAMMA RAY DATA

Jacob I. Trombka

CHAIRMAN:

Our next speaker is concerned with the problem of how one interprets data, gamma ray data taken in various kinds of detectors. His talk is entitled "Interpretation of 0.1 to 10 Mev Gamma Ray Data." This is Dr. Jacob Trombka.

DR. TROMBKA:

I would like to rephrase this problem in the following manner, that is, the attempt is made in this talk to describe a method by which one can obtain a unique inference as to the nature of the real world from an experimentally derived spectral measurement. The method is briefly outlined in Figure 1. Considering Equation 1 of Figure 1, the information that is desired in terms of correlating various theoretical models with experimental measurements is the true differential energy flux T(E). In order to make such measurement, one uses a detector to interact with the real world T(E), and what one actually observes is the interaction spectrum Y(V)—the so-called pulse height spectrum. The function S(E,V) is the so-called smearing function which is used to describe the interaction process characteristic of the given detector.

The problem now is to obtain the true spectrum T(E) information from the measured pulse height Y(V), knowing only the nature of the interaction process.

Specifically, the problem in the analysis of gamma ray spectra in this particular spectral region lies in the fact that one cannot perform this inverse transform analytically. Numerical methods must therefore be used. The first step in the development of a numerical method is to show that the integral in Equation 1 can be written as sum of discrete components. Remember also that T(E) is not a discrete distribution in energy; but, in terms of the observations that we are interested in, is a continuous energy distribution. It can be shown from information theory that both the integral and T(E) can be described as a sum of discrete energy components

which describe energy intervals ΔE about a given E. In this way we obtain the approximation formula, Equation 2.

In this form a valid numerical transform can be obtained using technique derived from the analysis of variance, and this solution in matrix form is given by Equation 3.

Because of the nature of this numerical method, the solution that one obtains depends strongly upon the algorithms used in obtaining the solution. Thus a very important part of this technique developed here at our laboratories depends on the algorithms used. These algorithms essentially confine the solution to a domain defined by the physical constraints of the problem. This allows us to obtain a unique solution.

A number of illustrations will now be presented in order to show the nature of the problem and the solutions that can be obtained. Let us assume that we are trying to measure a photon spectrum T(E) which can be described by an energy distribution $T(E)dE = E^{-2.3}dE$. Figure 2a shows such a distribution, and T(E)dE is indicated.

The spectrum is measured using, let us say, a $3'' \times 3''$ NaI(Tl) crystal. The pulse height spectrum Y(V)dV that would be obtained is also indicated in Figure 2a. If one attempts to determine the slope of the line of the pulse height spectrum, one finds the slope to be $Y(V)dV = V^{-2.9}dV$, significantly different from T(E). Of course, the shape of Y(V) will depend upon the size of the detector used, the resolution of the detector, the angular distribution of the incident flux, and other such factors. What becomes even more important is that if one assumes that superimposed upon this power law distribution is some type of distribution like the proton inelastic scattering process proposed in the previous paper (see Figure 2b), there is a deviation of T(E)dE from the exponential at higher energies. The problem that occurs is that the detection system damps out this deviation in the true spectrum T(E), and one loses the information concerning this non-exponential process if one analyzes the pulse height spectrum alone. This damping will depend again on such factors as the size of the crystal, the resolution, and the angular distribution of incident flux. Thus one can get almost any type of solution if one mistakenly uses the pulse height spectrum for correlating theory with experiment.

The analytic technique that we have developed here requires no a priori knowledge of the incident flux for obtaining the solution T(E)dE. All that is required is a knowledge of the nature of the interaction process S(E,V) for the given detector used for the observation.

Figure 3 shows both the measured pulse height spectrum and the photon spectrum obtained using the analytic described above.

Here you see a measured atmospheric gamma ray distribution obtained during a balloon flight using a $3'' \times 3''$ NaI(Tl) detector.

The 0.51 Mev annihilation gamma ray peak is easily recognized is the pulse height spectrum.

Now let us perform the numerical transformation and consider the photon spectrum obtained.

Here you see again the 0.51 Mev discrete line very clearly, but some other discrete lines now become more apparent than they were. As I have stated, no a priori knowledge of the incident photon spectrum was used in performing the analysis. What was observed after analysis was another two discrete gamma ray lines which were later identified as the potassium 40 (K-40) line due to the presence of this material in the atmosphere plus a magnesium 24 (Mg-24) line which can be attributed to the excitation by the incident cosmic flux on the gondola structural material. Once these discrete lines have been identified, they can be subtracted from the total photon spectrum to obtain the pure continuous photon spectrum.

Thus we believe that we have now developed a technique which does allow us to analyze the pulse height spectrum and obtain information which is independent of the detector system that is used, so that one can more precisely compare theory with experiment.

MEASURED SPECTRUM AS A FUNCTION OF PULSE HEIGHT V

INCIDENT PHOTON SPECTRUM AS A FUNCTION OF ENERGY E

SMEARING FUNCTION INTERACTION OF RADIATION WITH THE DETECTOR SYSTEM

$$Y(V) = \int_0^{E_{MAX}} T(E) \cdot S(E,V) \cdot dE \qquad (1)$$

FROM INFORMATION THEORY

$$Y_i \approx \sum_j T_j S_{ij} \qquad (2)$$

FROM ANALYSIS OF VARIANCE, SOLUTION IN MATRIX FORM

$$T = (\tilde{S}\omega S)^{-1} \tilde{S}\omega Y \qquad (3)$$

WHERE ω IS A STATISTICAL WEIGHTING MATRIX

Figure 1

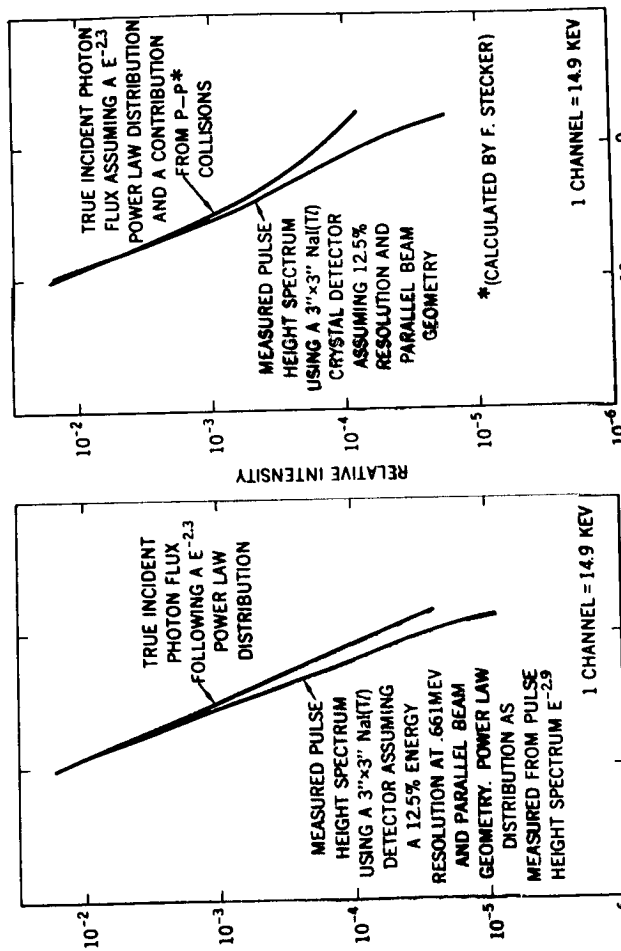
EFFECT OF DETECTOR INTERACTION WITH INCIDENT PHOTON FLUX IN THE MEASUREMENT OF GAMMA RAYS
RELATIVE INTENSITY
CHANNEL
TRUE INCIDENT PHOTON FLUX FOLLOWING A E^-2.3 POWER LAW DISTRIBUTION
MEASURED PULSE HEIGHT SPECTRUM USING A 3"×3" NaI(Tl) DETECTOR ASSUMING A 12.5% ENERGY RESOLUTION AT .661MEV AND PARALLEL BEAM GEOMETRY. POWER LAW DISTRIBUTION AS MEASURED FROM PULSE HEIGHT SPECTRUM E^-2.9
1 CHANNEL = 14.9 KEV
TRUE INCIDENT PHOTON FLUX ASSUMING A E^-2.3 POWER LAW DISTRIBUTION AND A CONTRIBUTION FROM P–P* COLLISIONS
MEASURED PULSE HEIGHT SPECTRUM USING A 3"×3" NaI(Tl) CRYSTAL DETECTOR ASSUMING 12.5% RESOLUTION AND PARALLEL BEAM GEOMETRY
*(CALCULATED BY F. STECKER)
1 CHANNEL = 14.9 KEV

Figure 2

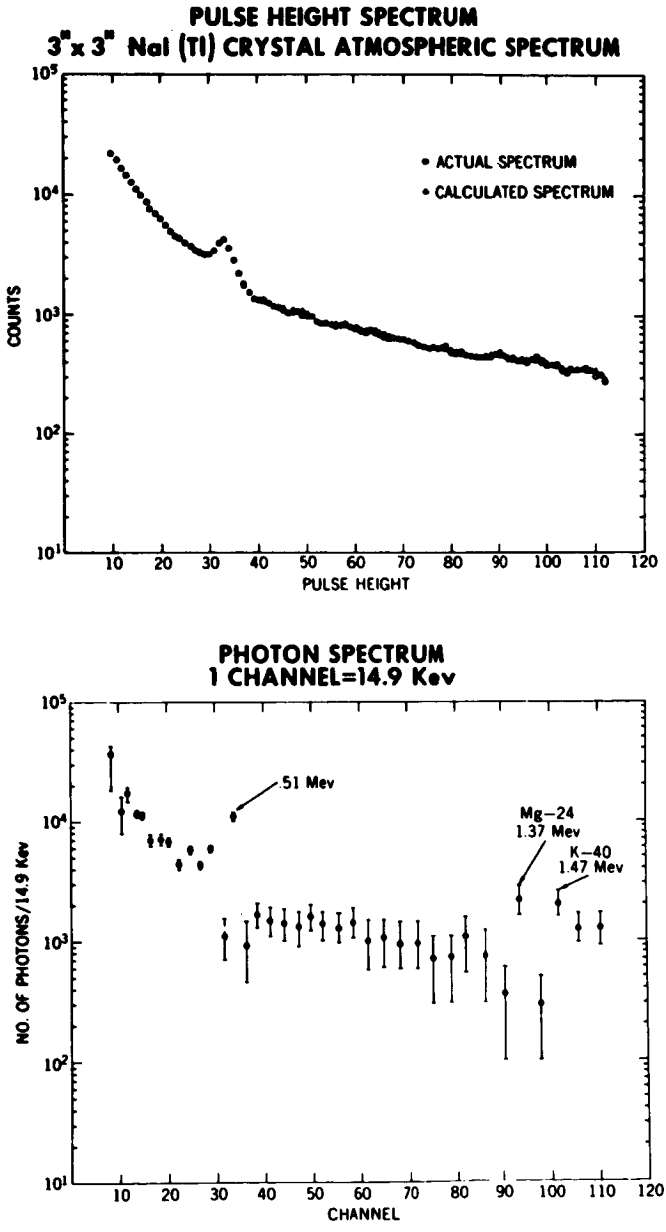
PULSE HEIGHT SPECTRUM
3" x 3" NaI (Tl) CRYSTAL ATMOSPHERIC SPECTRUM
• ACTUAL SPECTRUM
• CALCULATED SPECTRUM
COUNTS
PULSE HEIGHT
PHOTON SPECTRUM
1 CHANNEL=14.9 Kev
.51 Mev
Mg–24
1.37 Mev
K–40
1.47 Mev
NO. OF PHOTONS/14.9 Kev
CHANNEL

Figure 3

GAMMA RAY ASTRONOMY

Carl E. Fichtel

CHAIRMAN:

Our final speaker this afternoon has as his topic gamma ray astronomy. This is Dr. Carl Fichtel.

DR. FICHTEL:

The importance of gamma ray astronomy in the energy region above about 30 Mev has been recognized for over a decade. Gamma rays in this high-energy region are directly related to all the truly high-energy processes and energy transfers in the universe.

These high-energy gamma rays, however, are extremely elusive because they are not very intense as observed near the earth, and they have to be observed in the background of other forms of radiation and cosmic-ray charged particles. Therefore, it became apparent several years ago that a very carefully designed detector system with a large area must be built in order to observe these gamma rays in detail.

With this in mind, we began development of a digitized spark chamber for this and other experiments several years ago. We have been flying the original digitized spark chamber gamma ray telescope on high-altitude balloons for the last two years and have obtained some data related to gamma ray astronomy.

This original detector system is shown in Figure 1. The basic concept is the following. A conventional spark chamber has two plates to which high voltage is applied. We have replaced these two plates by wire grids. The wires in one wire grid plane are othogonal to those in the other so that, when the spark occurs after a charged particle has passed through the chamber, the current flows in one wire and out the other, setting a core on the end of each wire. The data, then, is contained in these cores and can be read out electronically and telemetered. By stacking a large number of these digitized spark chambers, in this case 32, we can obtain a three-dimensional picture of the event we are interested in and telemeter the data to the ground without having to take pictures of the events and recover the film.

A gamma ray in the high-energy region is detected by the formation of a negatron-positron pair in a pair production plate. The electrons are detected by two other detectors which trigger the spark chamber, if no charged particle has entered the system.

With this detector system we have set upper limits on a large number of sources, which are shown in Figure 2. The detection limit is set for the most part by the area and collecting time. We shall go over in the next few months to a larger system which will be limited only by the atmospheric background.

These upper limits are already significant, though, because they show that the X-ray sources do not extend, with the same nature, into the gamma ray region.

Turning next to another feature of the gamma ray region, I feel that the ultimate first-generation experiment, which does not include picture-type devices, is the experiment flown by Kraushaar, Clark, and Garmire on OSO 3. They have seen gamma rays in the high-energy—in their case, greater than about 50 Mev—region. Their results show a sharp peaking in the galactic plane and in particular in the galactic center, indicating that at least the predominant gamma rays are coming from the galactic plane and the galactic center.

The surprising feature of their work is that their flux is about 20 times higher than predicted by any source mechanism that one has been able to think of so far, including the one which was expected to be most intense, namely, the gamma resulting from decays of π^0 mesons formed in the interactions of cosmic rays with interstellar matter.

One suggestion by Clark et al. was that the radiation might be a sum of point sources, and they suggested that perhaps the X-ray point sources might be the ones which were contributing. We can tell from the upper limits shown in Figure 2 that this is not the case. We could have clearly seen the stronger X-ray point sources if the general gamma ray distribution were due to these point sources. The gamma radiation observed by the OSO 3 experiment could be a broad distribution which could not be seen with the limited size of this detector system.

Another cause of concern was the calibration of the OSO 3 gamma ray experiment. The calibration of these first-generation experiments is always difficult. Kraushaar and Clark talked to us and asked us if there was any way we could cross-correlate. There is indeed a method of

cross-correlating between experiments in flight by flying our detector system upside down, looking at the atmospheric background coming from the earth, and then comparing this with their OSO observation. The results are shown in Figure 3. This figure shows the gamma radiation coming down at balloon altitudes, horizontally, and directly upward. The upward flux is compared with the Explorer XI result, where the agreement is reasonably good, and with the OSO 3 result, where there is a factor of about 2-1/2 difference. Even after Clark and co-workers use the angular distribution and energy spectrum measured here, the differences is a bit larger than expected, but still confirms that the gamma ray flux measured by OSO 3 is at least an order of magnitude greater than expected.

Future experiments of the second-generation type should be able to determine the nature of this radiation by obtaining more accurate position information and energy measurements, and by having better sensitivity.

CHAIRMAN:

Are there any questions? Yes?

DR. ALOIS SCHARDT:

You showed an upper limit for the galactic center. Could you comment?

DR. FICHTEL:

That was for the galactic center as a point source. It is not inconsistent with the line source intensity measured by the OSO 3 experiment. We have now interpreted our data in terms of a line source. We do see something which is about two standard deviations above background. It is not inconsistent with the line source intensity measured by the OSO 3 experiment. However, you can't on the basis of two standard deviations say that we really see a positive flux. We can see this level of intensity easily with the bigger (half-meter-by-half-meter) spark chamber which we now have.

CHAIRMAN:

Are there other questions? Yes? Dr. Shapiro.

DR. MAURICE SHAPIRO:

If we defined the energy threshold of the detector at, say, 10 percent of your peak efficiency, about what is that figure?

DR. FICHTEL:

At about 20 Mev it is 20 percent, and it falls off very dramatically below that. We speak in terms of a cut-off at 30 Mev, in part because calibration below that energy is very difficult.

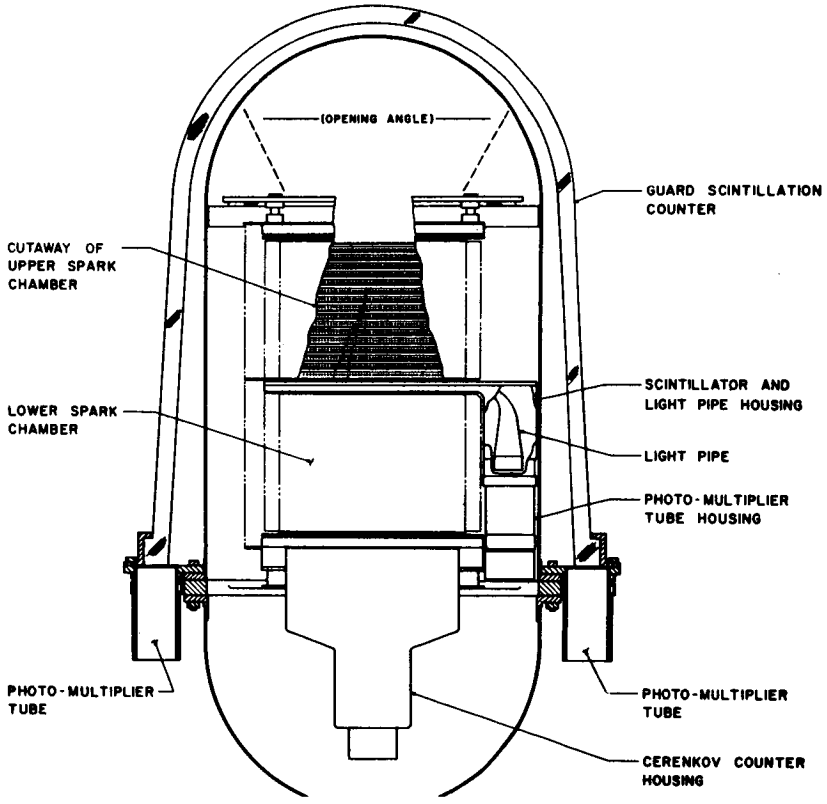

Figure 1

GAMMA RAY POINT SOURCE UPPER LIMITS (95% CONFIDENCE)	
SOURCE	LIMIT ($CM^{-2}SEC^{-1}$)
CRAB NEBULA	1.9×10^{-4}
CENTAURUS A	9.5×10^{-5}
QUIET SUN	2.4×10^{-5}
Sco X-1	2.4×10^{-5}
Sco XR-1	2.4×10^{-5}
GALACTIC CENTER	3.9×10^{-5}
KEPLER SUPERNOVA (Oph XR-1)	3.9×10^{-5}
Sgr XR-1	3.9×10^{-5}
Sgr XR-2	5.4×10^{-5}
VIRGO	9.0×10^{-5}

Figure 2

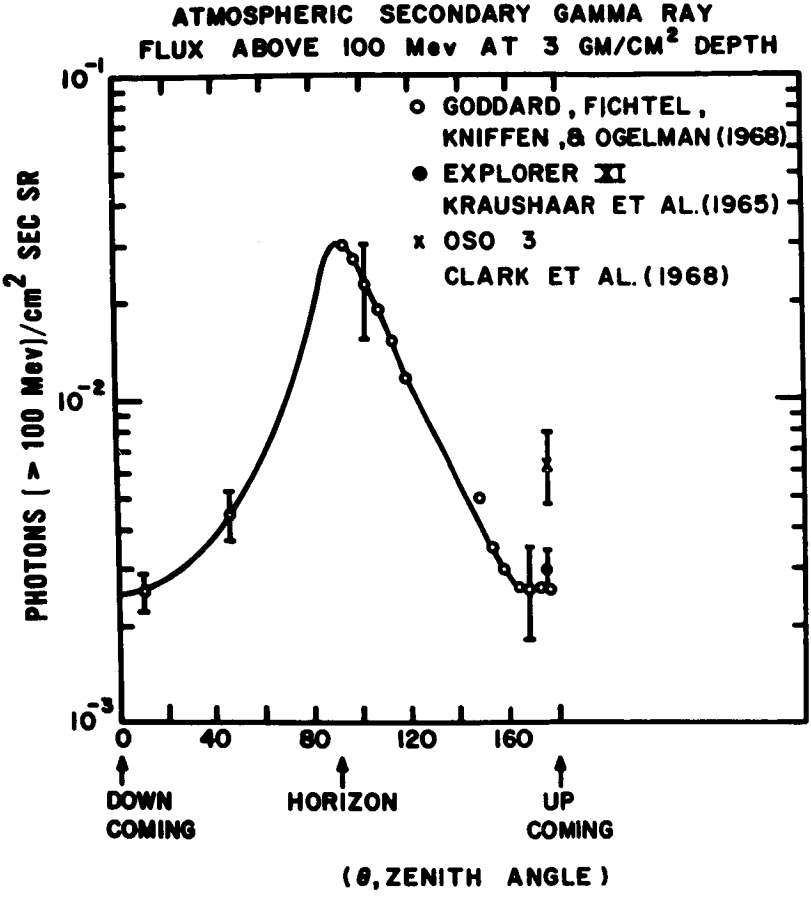
ATMOSPHERIC SECONDARY GAMMA RAY
FLUX ABOVE 100 Mev AT 3 GM/CM² DEPTH
o GODDARD, FICHTEL, KNIFFEN, & OGELMAN (1968)
● EXPLORER XI KRAUSHAAR ET AL. (1965)
x OSO 3 CLARK ET AL. (1968)
PHOTONS (> 100 Mev)/cm² SEC SR
10⁻¹
10⁻²
10⁻³
0
40
80
120
160
DOWN COMING
HORIZON
UP COMING
(θ, ZENITH ANGLE)

Figure 3

CONCLUDING REMARKS BY DR. PIEPER

I would like in conclusion to thank our more than forty speakers. I would like to thank my colleagues, Mr. Spencer, Dr. Northrop, Dr. Jastrow; and especially Dr. Meredith, who worked with me in preparing the program.

I would like to thank the audience. To those of you from NASA Headquarters, this was a report not just on our work, but on your work, because without your enthusiastic support for it we would not be able to carry it on. I hope that you have all gotten some semblance of the quality and the quantity of the work that we do here.

To those of you who could otherwise have been on "use or lose" annual leave, I am particularly grateful for your having come.

NASA-Langley, 1969 —— 34

NATIONAL AERONAUTICS AND SPACE ADMINISTRATION
WASHINGTON, D. C. 20546

OFFICIAL BUSINESS

FIRST CLASS MAIL

POSTAGE AND FEES PAID
NATIONAL AERONAUTICS AND
SPACE ADMINISTRATION

POSTMASTER: If Undeliverable (Section 158 Postal Manual) Do Not Return

"The aeronautical and space activities of the United States shall be conducted so as to contribute . . . to the expansion of human knowledge of phenomena in the atmosphere and space. The Administration shall provide for the widest practicable and appropriate dissemination of information concerning its activities and the results thereof."

— NATIONAL AERONAUTICS AND SPACE ACT OF 1958

NASA SCIENTIFIC AND TECHNICAL PUBLICATIONS

TECHNICAL REPORTS: Scientific and technical information considered important, complete, and a lasting contribution to existing knowledge.

TECHNICAL NOTES: Information less broad in scope but nevertheless of importance as a contribution to existing knowledge.

TECHNICAL MEMORANDUMS: Information receiving limited distribution because of preliminary data, security classification, or other reasons.

CONTRACTOR REPORTS: Scientific and technical information generated under a NASA contract or grant and considered an important contribution to existing knowledge.

TECHNICAL TRANSLATIONS: Information published in a foreign language considered to merit NASA distribution in English.

SPECIAL PUBLICATIONS: Information derived from or of value to NASA activities. Publications include conference proceedings, monographs, data compilations, handbooks, sourcebooks, and special bibliographies.

TECHNOLOGY UTILIZATION PUBLICATIONS: Information on technology used by NASA that may be of particular interest in commercial and other non-aerospace applications. Publications include Tech Briefs, Technology Utilization Reports and Notes, and Technology Surveys.

Details on the availability of these publications may be obtained from:

SCIENTIFIC AND TECHNICAL INFORMATION DIVISION

NATIONAL AERONAUTICS AND SPACE ADMINISTRATION

Washington, D.C. 20546